1991

Elevated temperature erosion studies on some materials for high temperature applications

Jianren Zhou
Iowa State University

INFORMATION TO USERS

This manuscript has been reproduced from the microfilm master. UMI films the text directly from the original or copy submitted. Thus, some thesis and dissertation copies are in typewriter face, while others may be from any type of computer printer.

The quality of this reproduction is dependent upon the quality of the copy submitted. Broken or indistinct print, colored or poor quality illustrations and photographs, print bleedthrough, substandard margins, and improper alignment can adversely affect reproduction.

In the unlikely event that the author did not send UMI a complete manuscript and there are missing pages, these will be noted. Also, if unauthorized copyright material had to be removed, a note will indicate the deletion.

Oversize materials (e.g., maps, drawings, charts) are reproduced by sectioning the original, beginning at the upper left-hand corner and continuing from left to right in equal sections with small overlaps. Each original is also photographed in one exposure and is included in reduced form at the back of the book.

Photographs included in the original manuscript have been reproduced xerographically in this copy. Higher quality 6" x 9" black and white photographic prints are available for any photographs or illustrations appearing in this copy for an additional charge. Contact UMI directly to order.

U·M·I

University Microfilms International
A Bell & Howell Information Company
300 North Zeeb Road, Ann Arbor, MI 48106-1346 USA
313/761-4700 800/521-0600

Order Number 9207259

Elevated temperature erosion studies on some materials for high temperature applications

Zhou, Jianren, Ph.D.

Iowa State University, 1991

U·M·I
300 N. Zeeb Rd.
Ann Arbor, MI 48106

Elevated temperature erosion studies on some materials for high temperature applications

by

Jianren Zhou

A Dissertation Submitted to the
Graduate Faculty in Partial Fulfillment of the
Requirements for the Degree of
DOCTOR OF PHILOSOPHY

Major: Mechanical Engineering

Approved:

Signature was redacted for privacy.
In Charge of Major Work

Signature was redacted for privacy.
For the Major Department

Signature was redacted for privacy.
For the Graduate College

Iowa State University
Ames, Iowa
1991

TABLE OF CONTENTS

INTRODUCTION

Erosion is a serious problem in many industries which puts a serious constraint on engineering design. The damage suffered from erosive attack has been observed in many devices used in energy production and utilization systems, transportation of airbone solids through pipes, boiler tubes exposed to fly ash, fluid cat crackers, helicopters operating in sandy terrains, high-performance marine vehicles, and space vehicles undergoing meteorite bombardment in upper atmospheres or landing on some planets.

If along with erosion high temperature corrosion is involved, it is a problem of combined erosion-corrosion where materials degradation occurs simultaneously by both the mechanical and chemical means. Examples of the components subjected to erosion-corrosion environment are aircraft gas turbine and compressor blading and other jet engine parts, steam turbine blades, pulverized coal-fired boilers tubes, fluidized bed combustion chamber and tubing, and rocket nozzles.

Recently, the erosion-corrosion problem has drawn particular attention. The Gulf War has brought home the recognition of the dependence of this country on oil imports, and the risks associated with it. The solution involves the utilization of coal as the major energy resource because coal supplies are abundant in this country. One of the main barriers in the utilization of coal is the high rate of material damage that

it causes in erosive-corrosive environment. The understanding of erosion-corrosion is thus very important for proper design and operation of the components in turbomachinery used in coal conversion and utilization. It is believed that along with other factors erosion-corrosion will also serve as a design parameter.

The material loss caused by erosion at room temperature has been studied extensively in the last fifteen years but the understanding of the mechanisms involved is still very limited. The high temperature erosion-corrosion studies were just initiated in the last decade. The understanding of this phenomenon is thus still in its infancy because of the complex interaction between the factors involved.

Explanation of Dissertation Format

This dissertation consists of five parts. Each of them contains sections on the introduction, experimental procedures, results, discussion, conclusions, and references. The figures are placed within the text. PART I was presented in a symposium, sponsored by the TMS-ASM Joint Corrosion and Environmental Effects Committee, which was held at the 118th Annual Meeting of The Minerals, Metals & Materials Society in Las Vegas, Nevada, February 27-March 3, 1989. It was published in the refereed conference proceedings entitled "Corrosion & Particle Erosion at High Temperatures." PART II was presented in the Fourth Berkeley Conference on the Corrosion-Erosion-Wear at Elevated Temperatures, held at Berkeley, California, January 31-February 2, 1990. It is also published in the refereed conference proceedings. The rest of the parts will be submitted as individual papers for publication in the professional journals. There are two published papers with the joint authorship of J. R. Zhou and S. Bahadur which are closely related to the present work but are

not included in this dissertation. These papers are: "Effect of Blending of Silicon Carbide Particles in Varying Sizes on the Erosion of Ti-6Al-4V," Wear, 132 (1989) 235-246; and "The Effect of Material Composition and Operational Variables on the Erosion of Alumina Ceramics," Wear, to appear shortly.

PART I.

HIGH-TEMPERATURE EROSION-CORROSION BEHAVIOR OF STAINLESS STEELS

ABSTRACT

The erosion-corrosion behavior of 304, 416, 430 and 17-4 PH stainless steels with 120 grit SiC particles accelerated by high pressure air was studied. The temperature range covered was from ambient to 800°C. The impact velocity was changed from 55 to 110 m/s and the impingement angle from 10° to 90° to study the effects of impingement velocity and angle on erosion rate. It was observed that erosion rate virtually remained unchanged up to about 200°C. After this erosion rate increased rapidly up to about 650°C and was followed by a moderate increase in erosion up to 800°C. The mechanical properties of the oxides produced and their bonding to substrate were studied. It is concluded that high temperature erosion is governed by interaction among features such as the rate of oxidation, mechanical erosion characteristics, temperature-dependent properties of the material, and the mechanical properties of oxides. Erosion mechanisms have also been investigated by SEM.

INTRODUCTION

The erosion behavior of metallic materials at room temperature has been extensively investigated and currently the emphasis is on the high temperature erosion-corrosion studies. Stainless steels are probably the most common alloys used for high temperature applications. For instance, they are used for automotive exhaust systems, combustion chambers, mufflers, nozzles, steam and gas turbine blades, coal gasification systems, and aircraft exhaust manifolds, a great deal of which involve an erosion-corrosion environment. A few workers have studied the high-temperature corrosion behavior of stainless steels [1-3]. For example, Fujikawa et al. [1] found that 347 stainless steel showed better resistance to high temperature corrosion due to the Cr-rich spinel oxide formed in the vicinity of metal/scale interface than other austenitic stainless steels in which this oxide layer was not formed. Ishiguro et al. [2] observed that the short term oxidation of Fe-18% Cr alloy proceeded in two stages –an initial rapid rate followed by a substantial slowing of the oxidation rate. The oxidation kinetics depended upon the temperature and oxygen pressure. Natesan [3] reported that for Fe-Cr-Ni alloys with high chromium content the alloy chemistry had only a minor influence on the type and morphology of the scales developed.

As for erosion, working under ambient condition with 304 SS, Morrison and Scattergood [4] found that the dependence of steady state erosion rate on erodent velocity and particle size was the same over the entire impact angle range. SEM observations of the surface eroded under steady state condition disclosed similar morphologies for the low and high angles of impact. It led these workers to conclude that a single mechanism controlled the erosion behavior of the stainless steel at room temperature.

Working under high temperature conditions in nitrogen environment, Levy et al. [5] reported that the erosion rate of stainless steels either remained constant or decreased as the test temperature was increased until a temperature was reached where a marked increase in erosion rate occurred with increasing temperature. These workers attributed this increase in erosion rate to the changes in the downward slope of the short-time tensile strength vs temperature plot. It was also observed that the velocity exponent in the erosion rate-velocity relationship for 310 SS eroded in non-oxidizing environment at 800°C was only half of its room temperature value.

Gat and Tabakoff [6-7] studied the erosion of 410 SS in air environment up to 204 °C and concluded that erosion was too complex to be analyzed by a single mechanism, as it was rather a combination of several mechanisms. These workers also found that the erosion rate of 410 SS depended upon the impingement angle. Shida et al. [8] studied the influence of erodent particle properties on the erosion behavior of some austenitic steels. They indicated that erodent particle hardness could be the most important factor in increasing erosion rate, particularly so at high temperatures. Levy et al. [9] studied the effects of erodent particle size and elevated temperature on the combined erosion-corrosion behavior of a series of Cr-containing steels. They found that the morphology of surface oxide was dependent upon the erodent particle size and test temperature.

Levy and Man [10] tested 9Cr-1Mo steel in air atmosphere and 310 stainless steel in nitrogen atmosphere. They found that for an impingement angle of 30° and velocity of 30 m/s, the continuous scale formed in air at high temperature on the surface of 9Cr-1Mo steel appeared to provide better protection to the metal surface in erosion than the discontinuous scale formed in nitrogen atmosphere on the 310

stainless steel surface.

The mechanisms of high temperature erosion and the interaction between erosion and corrosion are still not well understood. This realization together with the potential use of stainless steels in high temperature erosive environments and the lack of systematic erosion-corrosion studies on all representative kinds of steels led to the present work. We studied here the erosion of one of each of the austenitic, ferritic, martensitic and precipitation hardening types of stainless steels with emphasis on the interaction between erosion and corrosion along with other aspects.

EXPERIMENTAL DETAILS

A vertical sand-blast type of high temperature test rig, as shown in Figure 1, was designed and fabricated for erosion-corrosion experiments. It consists of a heating cylinder A, particle chamber B, mixing block C and specimen holding arrangement D. The gas-particle mixing block C, specimen holder D and acceleration tube E are located inside a furnace. The particle chamber B has a cylindrical heater wrapped around it so as to heat erodent particles before entering the mixing block. The main cylinder A is made of stainless steel and is stuffed with stainless steel mesh to provide a very large surface area for heating of the gas passing through it. The cylinder A as well as the mesh inside it are heated with cylindrical heaters F. The temperatures of all the units are monitored and automatically adjusted by independent temperature controllers to ensure that the desired temperatures were reached. The tubes connecting the teated cylinder, particle chamber and mixing valve are heavily insulated. The acceleration tube is of 3 mm inside diameter and the gap between the tube-end and the specimen surface is 7 mm. The carrier gas which is used for accelerating erodent particles is supplied from a high pressure gas cylinder. Its entry to the system is controlled by a solenoid valve G. During its passage across the large heated surface in the heating cylinder, it gets heated to the desired temperature. The heated gas makes its way to the mixing block as well as the upper end of the particle chamber. The valve H regulates the pressure of gas entering the chamber B and thereby regulates particle flow. The particles carried by gas enter the mixing block C and are accelerated by high pressure heated gas in the acceleration tube E. For the particular system, the impingement velocity of particles on specimen surface is governed by the pressure of gas entering the system.

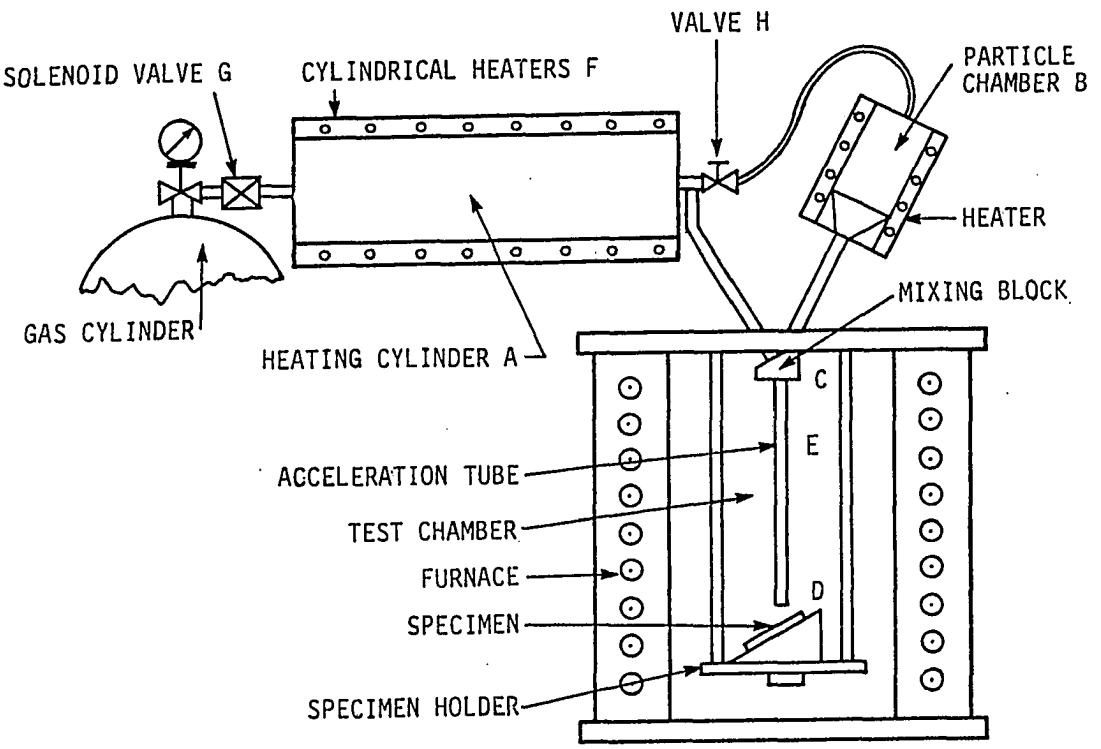

Figure 1: Schematic diagram of high temperature erosion-corrosion test rig

The possibility of the drop in specimen surface temperature due to the impingement of heated air was checked by placing the a thermocouple directly in the impingement location on the specimen surface. It was perceived that the air might not get heated sufficiently during its passage through the heated cylinder. A number of heater settings for the heating cylinder and particle chamber were tried to obtain an acceptable temperature drop. The temperature settings that were used finally indicated a drop in the specimen surface temperature on the impingement of air of 15, 12 and 8°C for the test temperatures of 800, 650 and 500°C respectively. There was no temperature drop observed in case of 400 and 200°C test temperatures.

The materials selected for the investigation were 430, 304, 416 and 17-4 PH stainless steels which represented the four main groups of stainless steels, namely the ferritic, austenitic, martensitic and precipitation hardening, in the same order. Specimens were prepared from commercial flat bar or rod stock. The ferritic 430 SS and austenitic 304 SS were used in the annealed condition, 17-4 PH steel was double aged, and the martensitic 416 SS was austenitized at 980°C and tempered at 205°C. After heat treatment the specimens were ground and polished by abrasion against emery paper in running water sequentially down to 600 grade finish.

Commercial silicon carbide particles in 120 grit size, supplied by the Buehler Corporation, were used as erodents. The erodent mass flow rate was 20 g/min. Air, which is the most common oxidant in industrial practice was used for accelerating these particles. Most of the erosion experiments were done with an impingement angle of 30° but in some experiments the impingement angles were varied from 10° to 90°. The particle impingement velocities at different temperatures and gas pressures were measured by a double-disk arrangement. They ranged from 55 m/s to 110 m/s. The

Erosion test on any specimen lasted for about 110 minutes. The specimens were impacted with a total of 100 g erodent particles in ten steps of 10 g each with an interval of 10 minutes between each step. Erosion rate was calculated by dividing the total mass loss by the total mass of erodent impacted.

High temperature corrosion-only experiments were also carried out in the same test rig by using the same air flow rate as used in erosion experiments but the impact of particles was avoided.

The surfaces of corroded and eroded-corroded specimens were studied by scanning electron microscopy.

RESULTS AND DISCUSSION

Variation of Erosion with Operating Parameters

The operating parameters considered in this study were the temperature, impingement angle and erodent particle velocity. As for the temperature, erosion was measured at six different temperatures: room temperature, 200°C, 400°C, 500°C, 650°C and 800°C. Figure 2 shows the variation of erosion rate with temperature in the presence of corrosion for stainless steels at an impingement angle (α) of 30° and velocity (v) of 65 m/s. At the end of high temperature erosion-corrosion tests, oxide film with discoloration was observed on the surface of specimens exposed to 400°C and above outside of the particle impact area. The data obtained from corrosion (only) tests indicated no weight gain from high temperature corrosion in the case of specimens exposed to as high a temperature as 650°C for 110 minutes and only negligible weight gain (about 0.2 mg weight gain compared to about 20 mg material loss by erosion) for those exposed to 800°C for the same period of time. Figure 2 shows that as the temperature increases above ambient, erosion rate remains unchanged up to 200°C, then it increases rapidly and shows very little change after 650°C. The variation of erosion rate with temperature will be explained later.

The variation in the erosion rate of 304 SS with impingement angle both for the room temperature and 500°C conditions is given in Figure 3. It is noted that erosion rate peaks around 30° at room temperature and around 20° at 500°C. The maximum in erosion rate within 20° to 30° is typical of ductile materials and so does not need explanation.

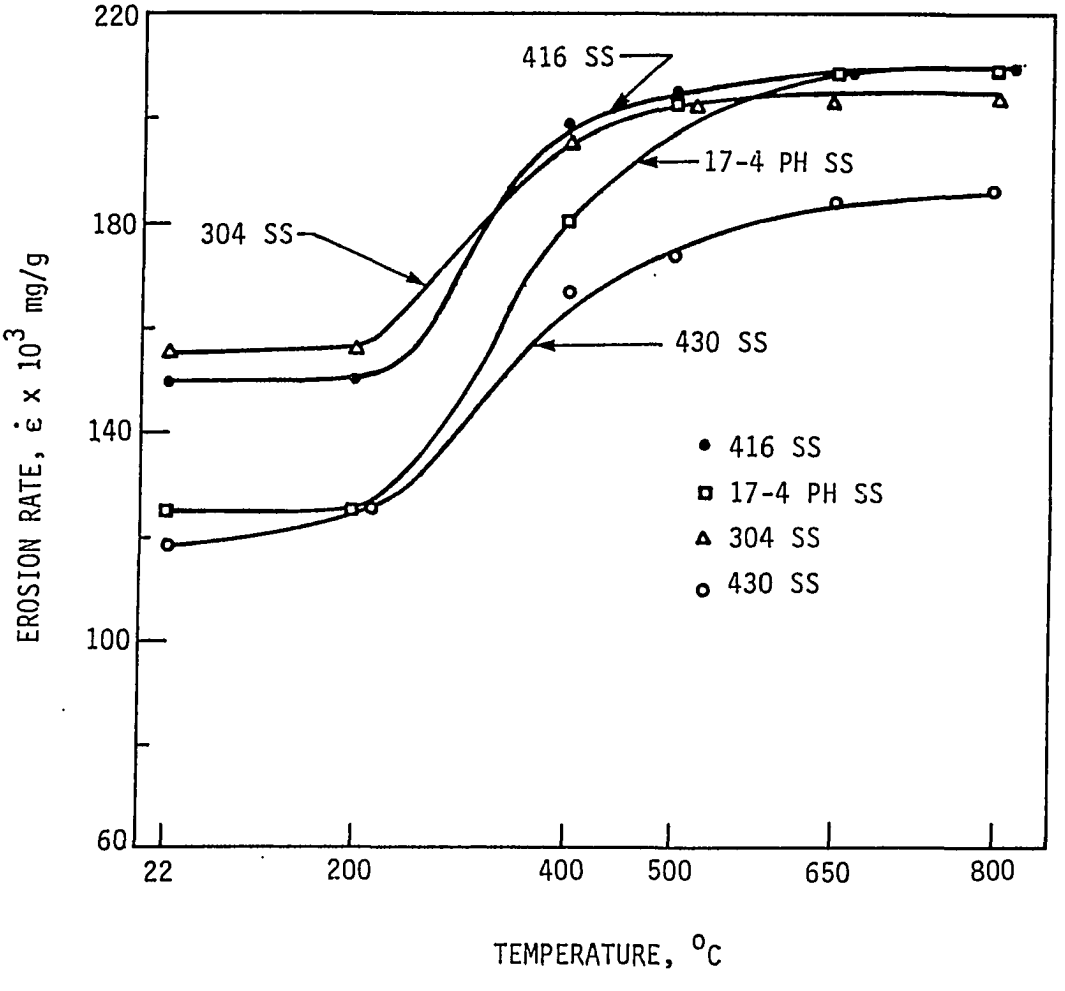

Figure 2: Temperature dependence of erosion rate for various kinds of stainless steels (v = 65 m/s, $\alpha = 30^{\circ}$, 120 grit size SiC particles, accelerating gas is air)

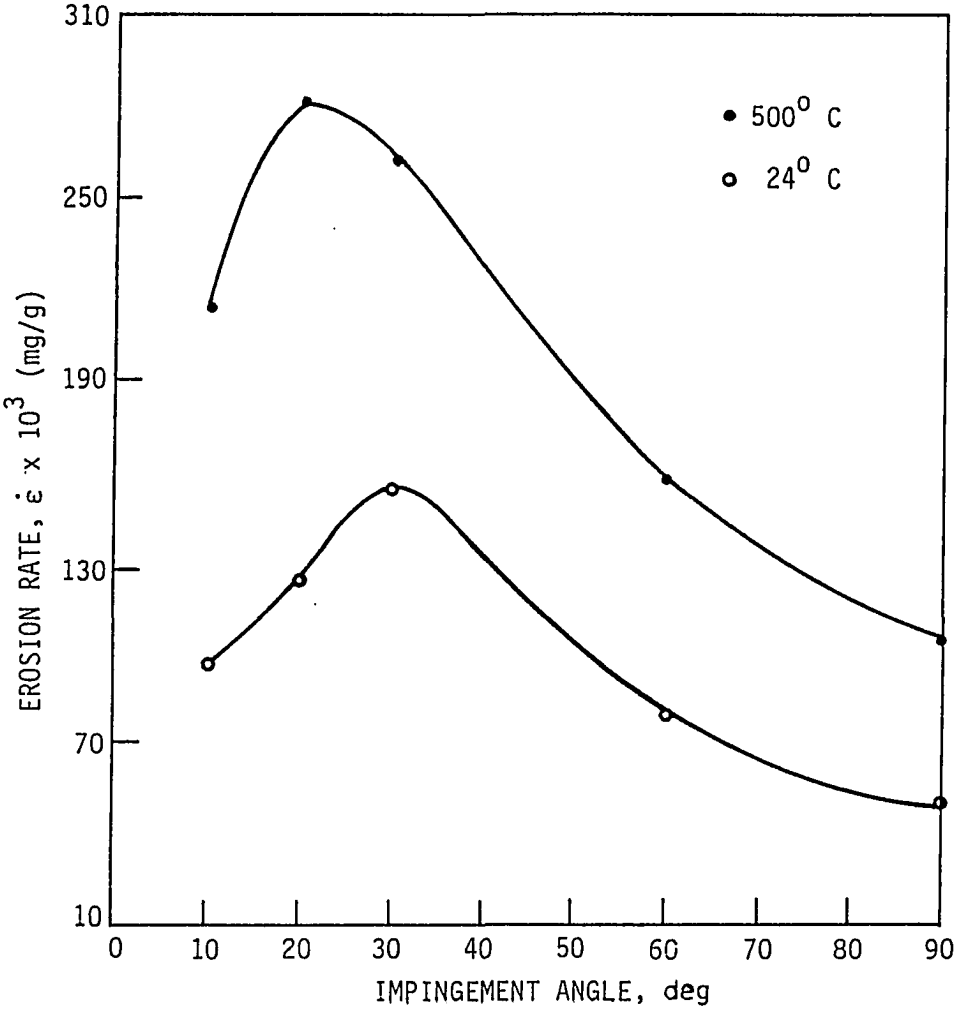

Figure 3: Impingement angle dependence of erosion rate of 304 SS at 24°C and 500°C (velocity 70 m/s)

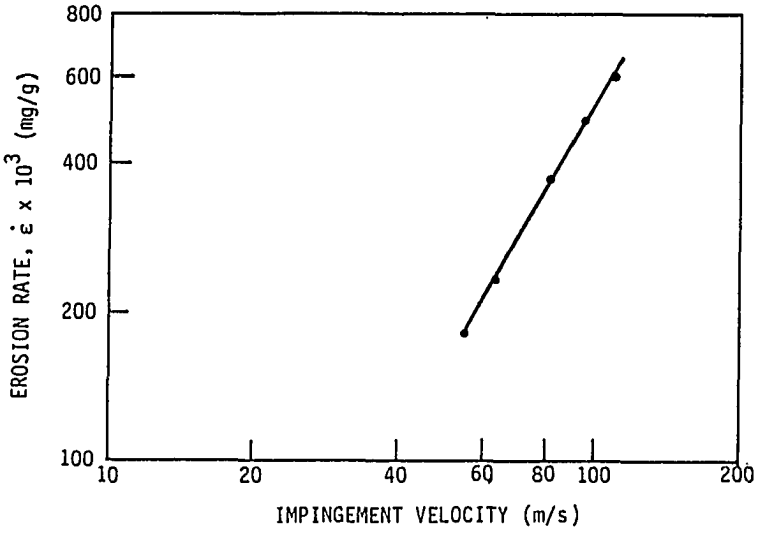

Figure 4: Variation of erosion rate with impingement velocity for 304 SS at 500°C (impingement angle 30°)

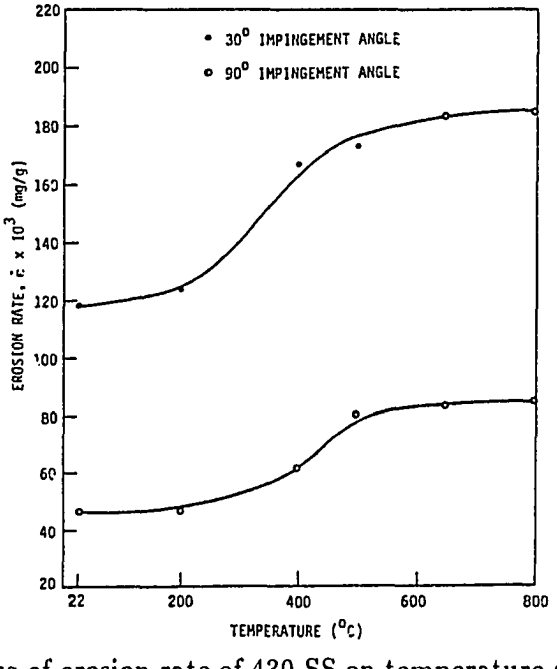

Figure 5: Dependence of erosion rate of 430 SS on temperature at the impingement angles of 30° and 90° (velocity 65 m/s)

The effect of impingement velocity on the erosion rate of 304 SS at 500°C is shown in Figure 4. According to this data, erosion rate is directly proportional to $(velocity)^{1.8}$. Since the velocity exponent under ambient conditions is 2 or above [11], it implies that the erosion rate at high temperature is less sensitive to impingement velocity.

Figure 5 shows the variation in the erosion rate of 430 SS with temperature at the impingement angles of 30° and 90°. It reveals that the shape of both curves is identical although the erosion rates in normal impact are less than half of those at 30° impact for the corresponding temperatures. The latter is also typical of the erosion behavior of ductile materials.

Morphological Features of Eroded-Corroded Surfaces

Figures 6 to 9 show the surface features on the specimen surfaces produced by combined erosion and corrosion on 430, 17-4 PH, 304 and 416 stainless steels, respectively. Each figure includes scanning electron micrographs for both the room temperature and high temperature conditions. Careful examination of details revealed that there are some fine differences in microfeatures which reflect the effect of temperature and corrosion on erosion features. It is noted that in the case of all the stainless steels the domains produced by impacting particles on the surfaces of high temperature specimens are larger than those on the surfaces of room temperature specimens. The "rub" bands which were produced due to erodent particle sliding are wider at higher temperatures too. The crater surfaces of all high temperature specimens appear to be more jagged with relative "ductile" characteristics while the features on room temperature specimens are finer with relatively less ductile char-

acteristics. The grooves in the case of high temperature specimens are deeper and wider.

The high magnification micrograph in Figure 6(d) exhibits features representing the interaction between erosion and corrosion when tested at 800°C. It may be seen that the material has undergone severe plastic deformation in erosion. There are some oxide crystallites and scales present on the surface while some scale fragments are embedded in discrete locations. The diagram shows an erosion pit and the material overhanging above it.

The features in the halo zone (Figures 6(e) and (f)) are similar to those in the center of crater (Figures 6(b), (c) and (d)) with the only difference that ploughing in the halo zone is virtually absent and the compaction of material is evident. This is because of the lower particle concentration and lower energy associated with scattered particles which are responsible for producing halo zone. The high magnification photograph (Figure 6 (f)) shows severe deformation of material, microcracking in oxide scale and the protection provided by it to the material underneath.

Figure 10 provides the cross-sectional views of the craters of 430 stainless steel formed by erosion at the temperature of 200, 500 and 800°C. The surface topography resulting from erosion at 200°C is wavy, as is typically observed in the erosion under ambient condition. It resulted from the impingement of eroded particles at 30° to the surface as well as the particles being reflected back also at about the same angle. The deformation in the substrate (particularly seen in Figure 10(c)) exhibits microcracking which contributed to the loss of material in the erosion process. There is also some evidence of flake formation on the surface. The depth of the crater formed by erosion at 500°C is much larger than that at 200°C, which would account for the

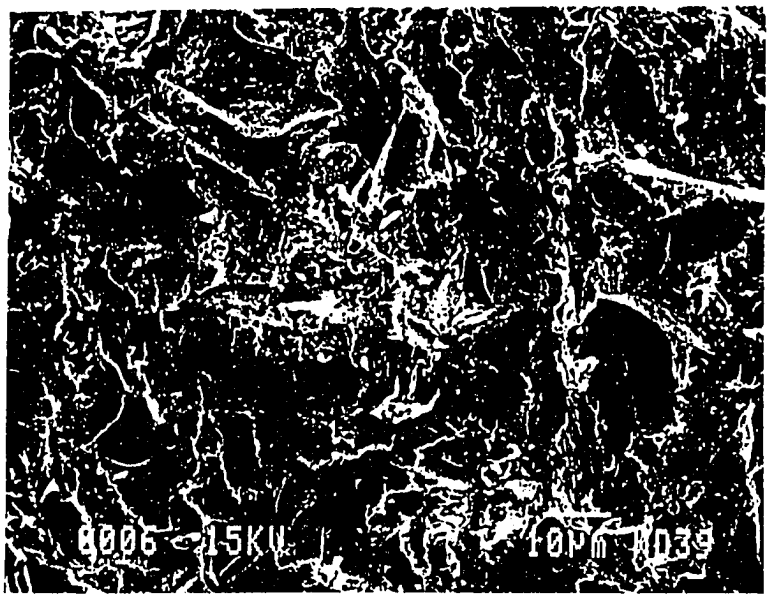

a

b

Figure 6: Electron micrographs of the craters of 430 SS for the erosion test temperature and crater locations indicated below: (a) 24°C , center of crater; (b) 650°C, center of crater; (c) and (d) 800°C, halo zone (v = 65 m/s, α = 30°)

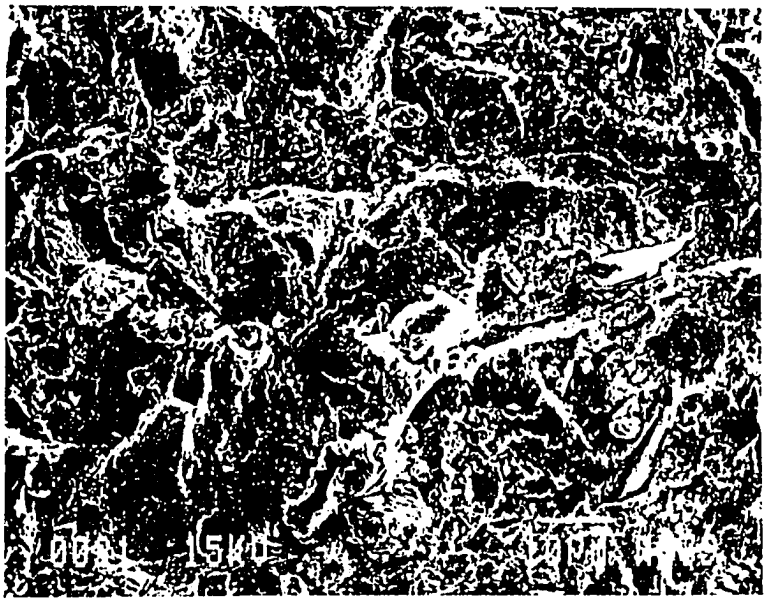

c

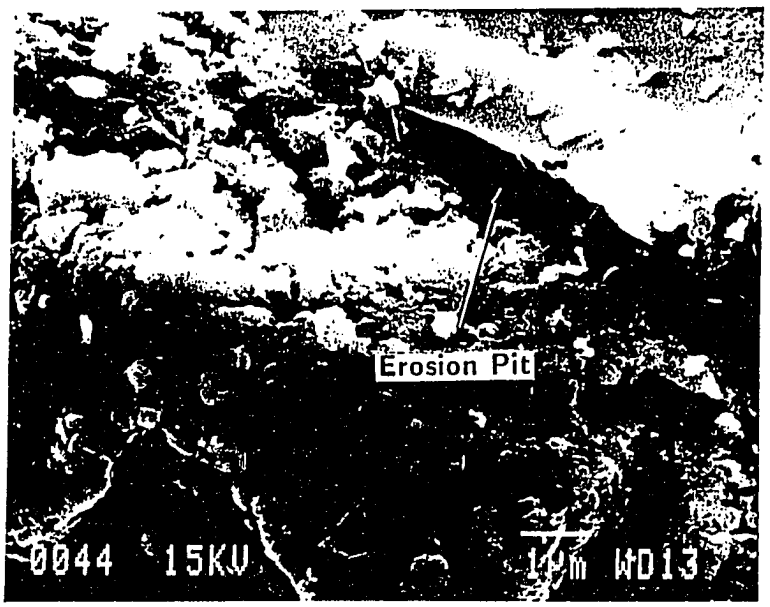

d

Figure 6 (Continued)

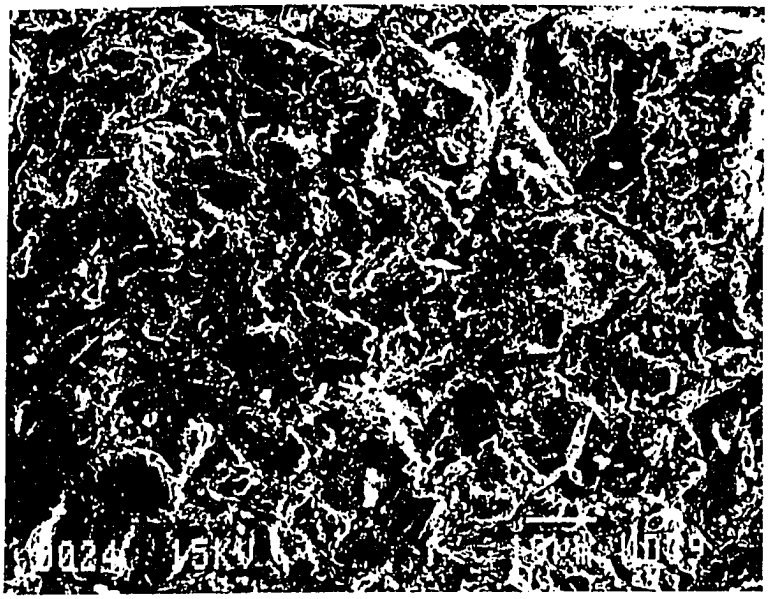

e

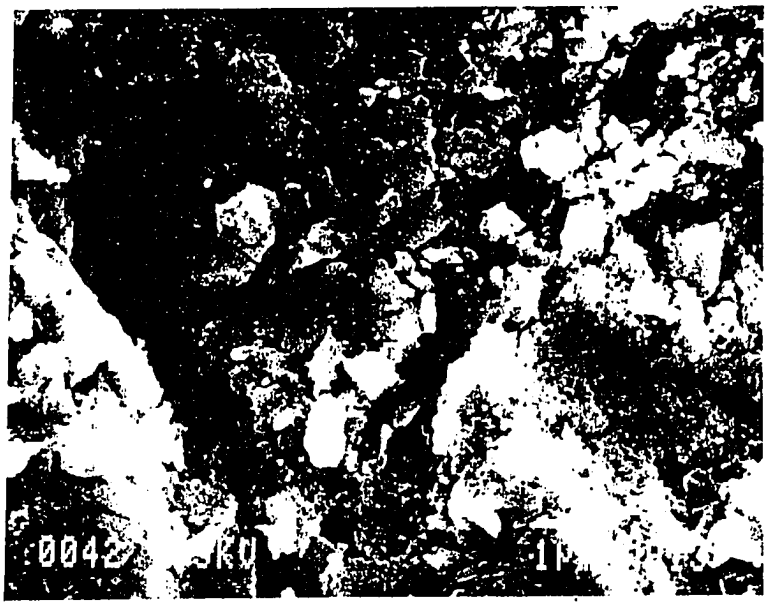

f

Figure 6 (Continued)

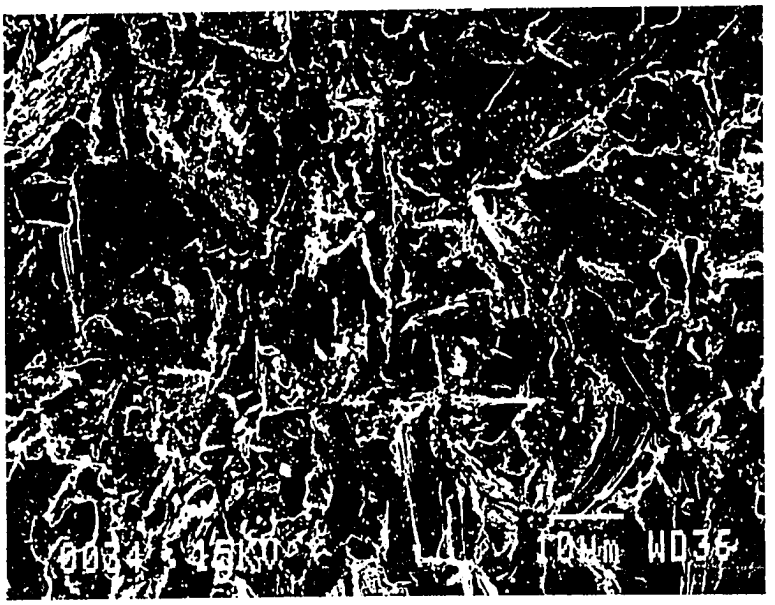

a

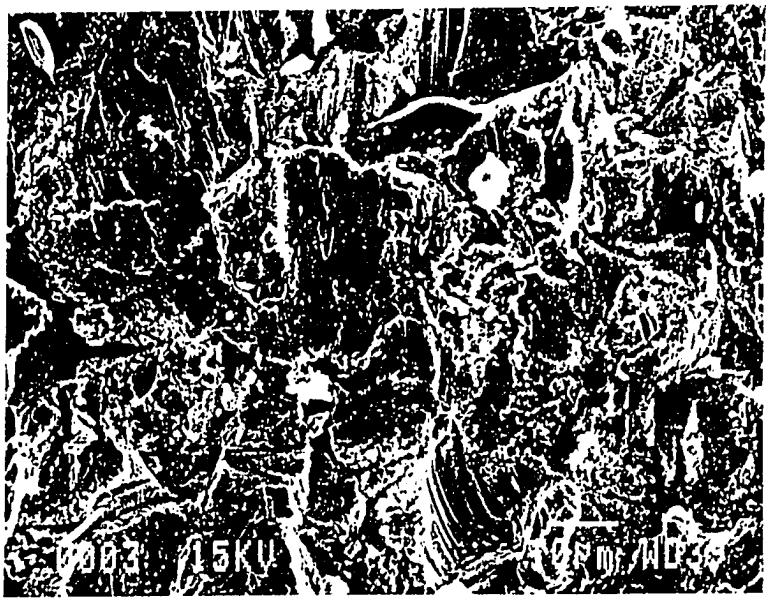

b

Figure 7: Electron micrographs of the crater centers of 17-4 PH SS: (a) for erosion at 24°C; (b) for erosion at 800°C

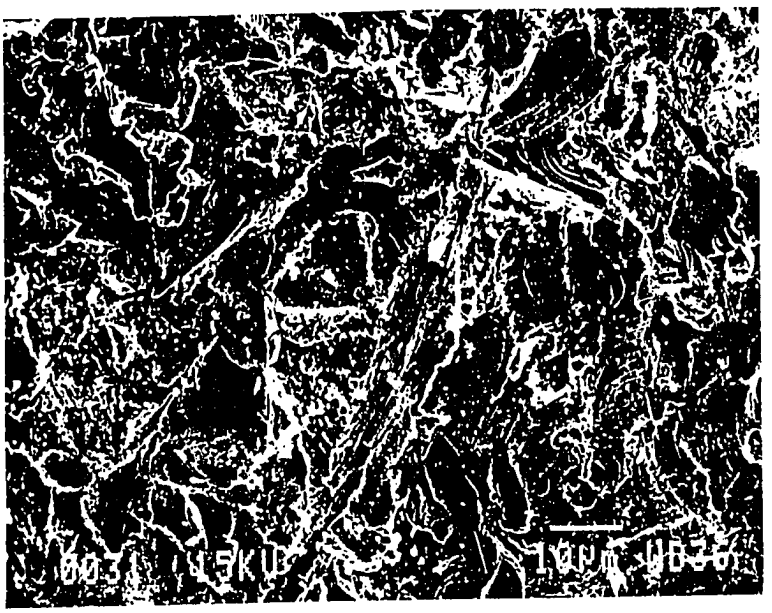

a

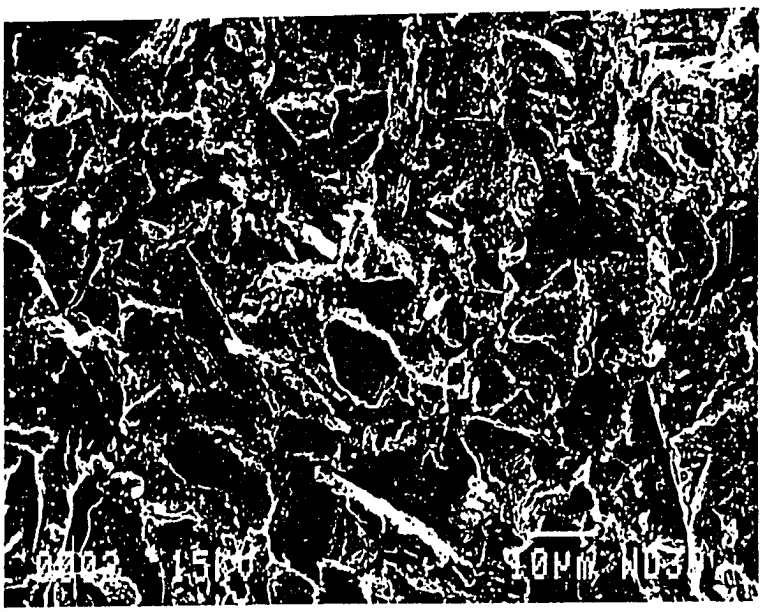

b

Figure 8: Electron micrographs of the crater centers of 304 SS: (a) for erosion at 24°C; (b) for erosion at 800°C

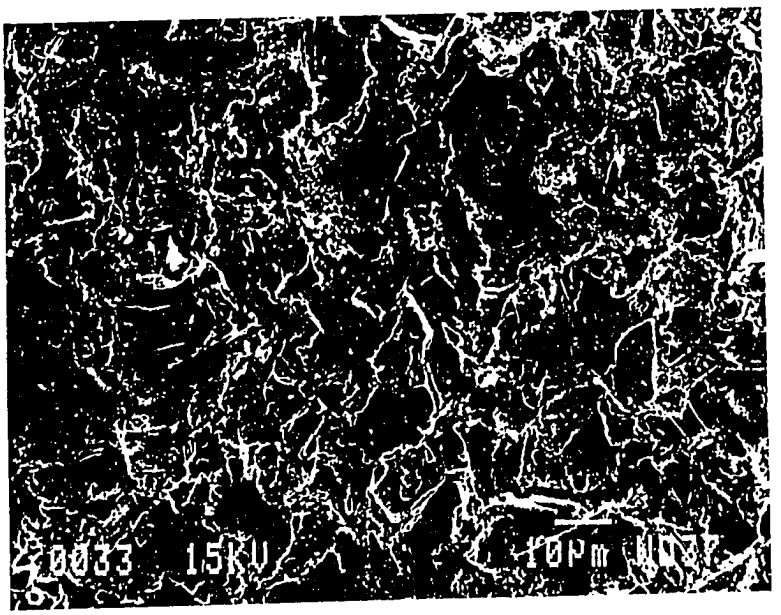

a

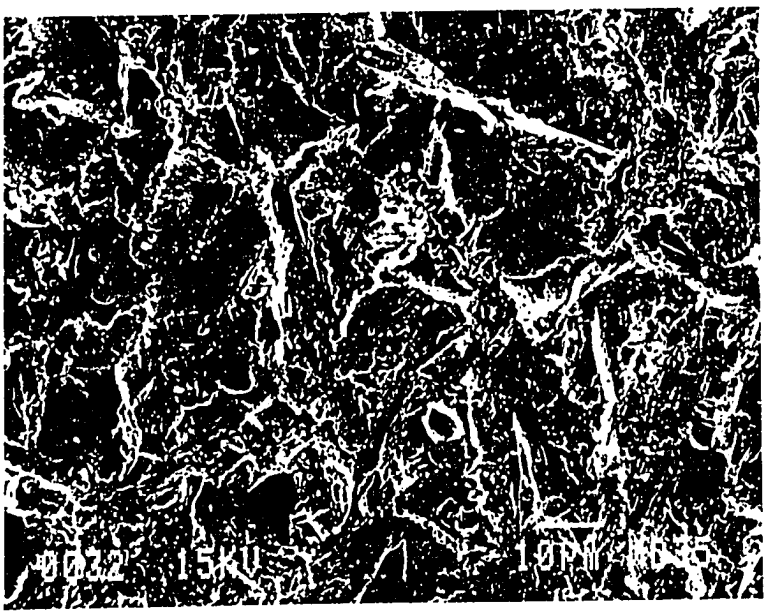

b

Figure 9: Electron micrographs of 416 SS: (a) for erosion at 24°C; (b) for erosion at 800°C

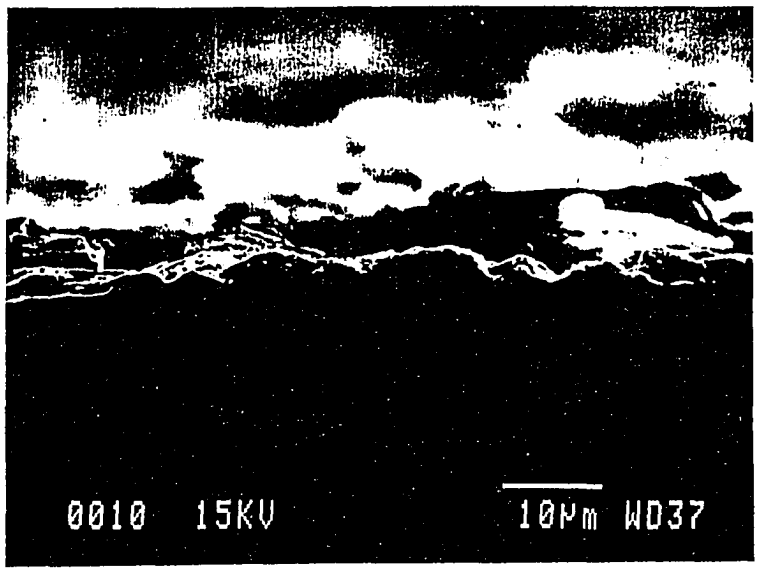

a

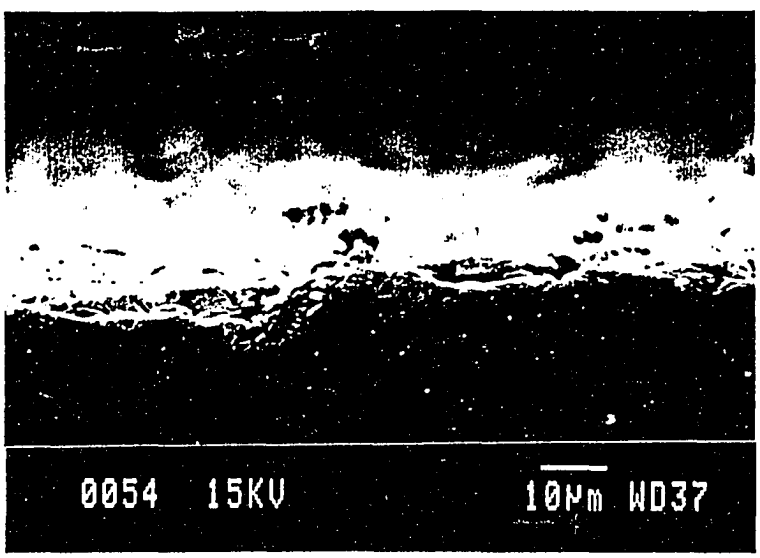

b

Figure 10: Cross-sectional views through the middle of crater of 430 SS eroded at (a) 200°C; (b) and (c) 500°C; (d) 800°C

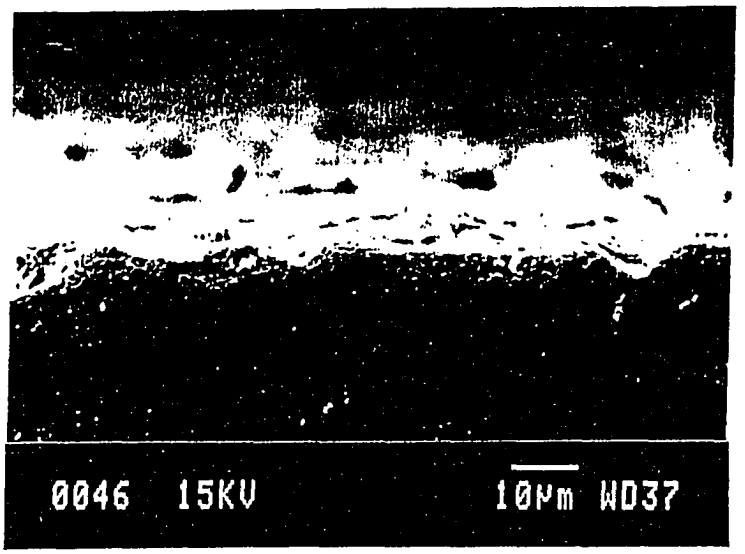

c

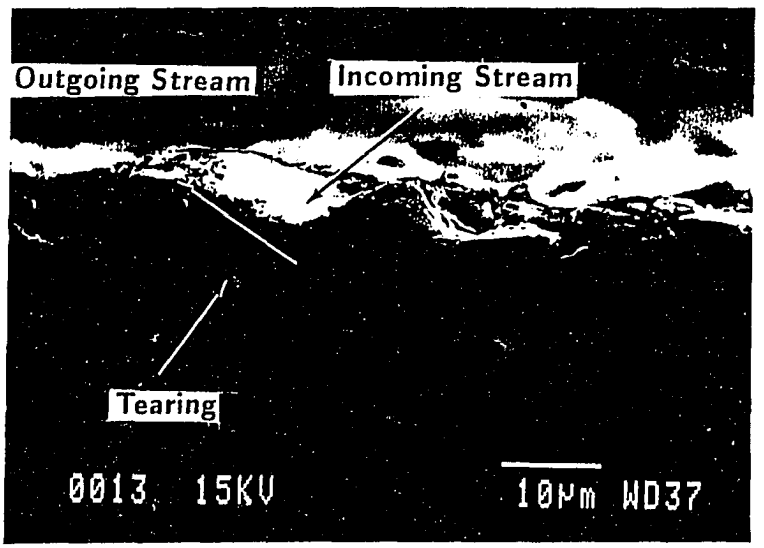

d

Figure 10 (Continued)

erosion being much greater at the higher temperature as seen in Figure 2. That is also the case at 800° C. The sectional views corresponding to the temperatures of 500 and 800°C show that the high-velocity stream of erodent particles cuts through the base material separating the fragments of material on its way. The lower the strength of the material, the deeper will be the penetration of the particle stream. As the particles are reflected back, they tend to tear the overhead material as shown in Figure 10(d) which could finally result in the detachment of a fairly large fragment of material.

Corrosion Aspects in the Erosion-Corrosion Process

Stainless steels react to form surface oxide scales when exposed to air (or oxygen) at high temperatures. The oxidation rate is a function of temperature and the resistance-to-attack is a function of the protection afforded by the scale formed. Figure 11 shows the oxidation behavior of stainless steel in 0.1 atm oxygen as a function of time and temperature [12]. It may be seen that the oxidation rate up to 650°C is low and it becomes significant at 700°C. The weight increase obtained from corrosion tests on different kinds of stainless steels exposed to flowing air at 800°C for 110 minutes was $0.1 \sim 0.4$ mg on a specimen of the size $25.4mm \times 19.0mm \times 3.2mm$ which amounted to $(0.8 \sim 3.2) \times 10^{-4}$ mg per mm^2 surface area. This weight gain is negligible compared to the material loss of about 20.0 mg in erosion when impacted by 100 g erodent.

The oxidation features on the surface of 430 SS exposed to still air at 650°C for 10 minutes are shown in Figure 12(a). It may be seen that during this short time oxide crystallites initiated and grew to about 0.05 μm size. They seem to have

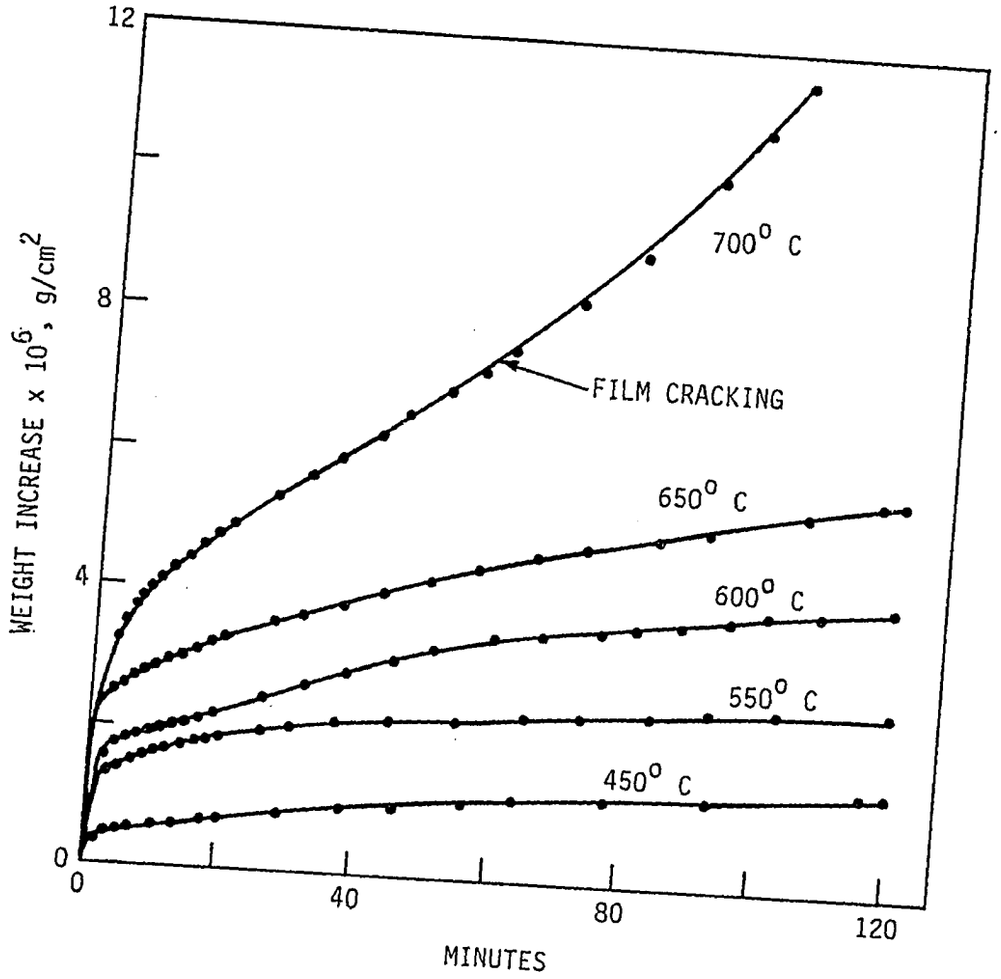

Figure 11: Oxidation of stainless steel at various temperature in 0.1 atm oxygen [12]

initiated preferentially in defect locations such as scratch marks. The oxide scale formed is neither uniform nor continuous. Due to its sparse nature, this oxide scale would not be expected to play a significant role in the high temperature combined erosion-corrosion process. Therefore, the erosion rate variation with temperature below 650°C is basically due to changes in the temperature-dependent properties of stainless steels.

Oxidation becomes fairly profound when the stainless steel is exposed to air at 800°C even for a short duration of 10 minutes as shown in Figure 12(b). In this case, oxide crystallites have covered the entire surface providing the appearance of a monolayer of oxide scale with some overlap only in discrete locations, possibly of defects. The bulk of the crystallites are 0.15 μm in size while some, which probably resulted from the growth of preexisting oxide crystallites, are more than double in size. The crystallites are in the shape of multi-faceted polyhedra. After a prolonged exposure of 110 minutes, there is a multiple-layer deposition of crystallites, as shown in Figure 12(c), resulting in a thicker oxide scale. It is noted that the contribution to the thickening of oxide scale comes from three processes: the growth of preexisting crystallites, the initiation of new crystallites, and the agglomeration of crystallites. The figure also shows that these crystallites which are initially multi-faceted become round with longer exposure times.

Oxide Scale Characteristics

Although there were no significant weight gains from oxidation in the case of specimens exposed to air at 800°C, a uniform and continuous thin oxide scale did form on the surface even after 10 minutes exposure, as seen above. Whether erosion

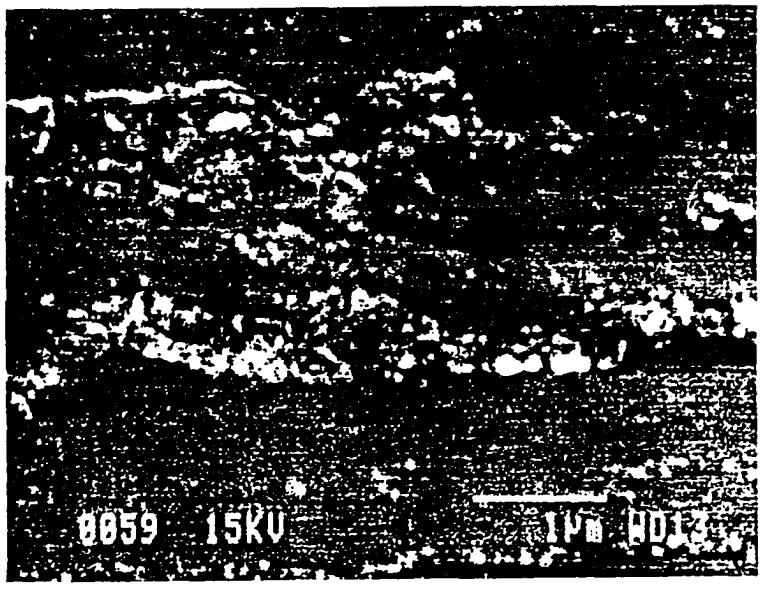

a

b

Figure 12: Morphology of high temperature corroded surface of 430 SS exposed to air at the temperatures and times given: (a) 650°C, 10 min; (b) 800°C, 10 min; (c) 800°C, 110 min

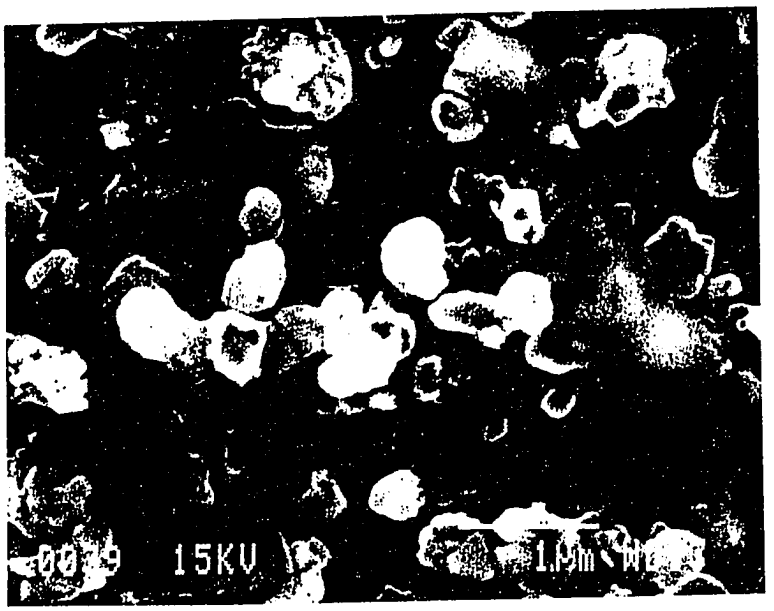

c

Figure 12 (Continued)

is accelerated or retarded by corrosion depends upon the degree of oxidation and the properties of the oxide scale formed. The extent of oxidation as a function of time and temperature has already been discussed. We would now study the properties of oxide at room temperature. Admittedly, the properties at room temperature may be different from those at high temperatures, but they should still provide some insight into the relevant aspects.

In order to analyze the adhesion of oxide film to the base material under plastic deformation conditions, an indentation was made on the oxidized surface (exposed to air at 850°C for 4 hours) of 430 SS with a square-base pyramid diamond indentor and 100 g load. This is shown in Figure 13 both at low and high magnifications. The crystallites of oxide are seen to undergo plastic deformation along with the base material because the oxide film stays mostly unbroken. There are some locations within the bounds of the indentation where oxide scale appears to be thin. There is no evidence showing that the scale was separated from the substrate. The microhardness measurements with 100 g load on the surface oxidized at 800°C and the substrate beneath it gave DPH values of 178 and 163, respectively. The higher value of hardness in the former case indicates that the stainless steel surface with oxide on it is stronger than in the latter case. We could thus conclude that the the oxide scale formed on the stainless steel surface is hard, pliable and adherent to the base metal. In a situation like this where oxide acts as a barrier between the base metal and outside effect, which may be a high temperature environment or a stream of impacting erodent particles, oxide would be expected to play a significant role in the erosion-corrosion process.

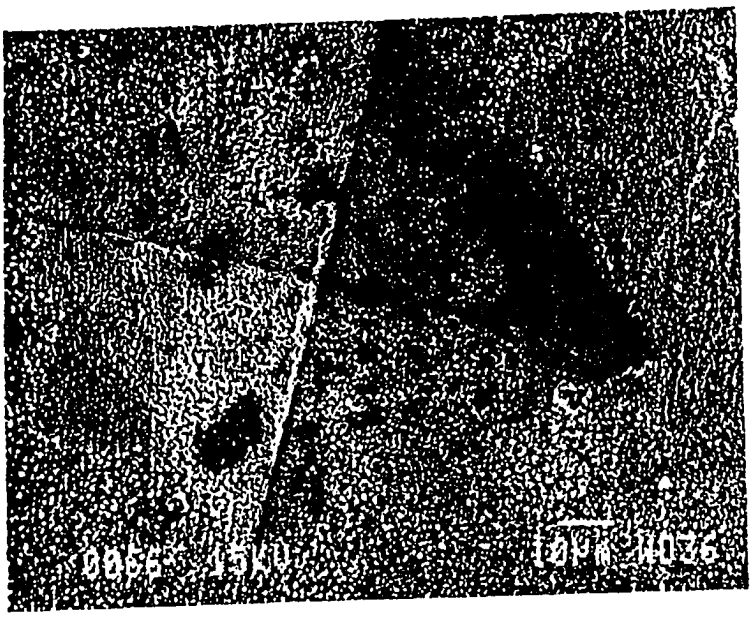

a

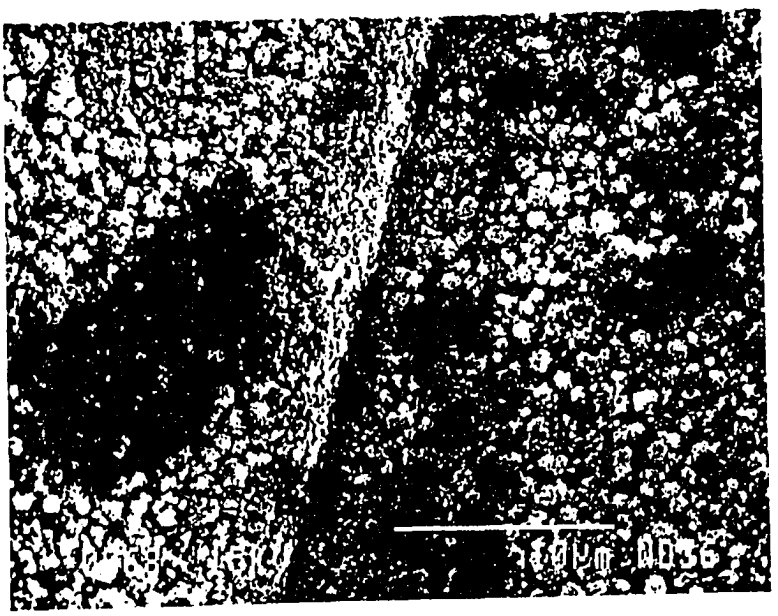

b

Figure 13: Microindentation on the surface of 430 SS oxidized at 850°C showing details at two magnifications

DISCUSSION

It is the protective nature of oxide scale that accounts for the heat-resistance of stainless steels. Once a thin chromium oxide layer is formed, it serves as a barrier between the base metal and corrosive environment and thereby protects the metal from further corrosion. As for erosion, the oxide scale could be resistant to erosion depending upon its thickness, strength, and its ability to deform and to keep adhering to the base material. In high temperature erosion-corrosion, it is thus possible for the oxide scale to retard both corrosion and erosion. At relatively modest temperatures, say up to 200°C, the oxidation rate is negligibly low so that it has virtually no effect on erosion. The oxide scale formed from 650°C to 800°C has erosion resistant properties: strong, pliable, continuous and good adherence to the substrate. As such, it would be expected to slow down the increase in erosion rate in this temperature range, which is the case as observed in Figure 2. In order to verify that the moderation in erosion rate was due to oxide scale, 430 SS was eroded at 800°C with nitrogen as the carrier gas and the test chamber was maintained under positive nitrogen pressure at all times. The erosion rate in this non-oxidizing atmosphere was found to be close to 0.2 mg/g compared to 0.185 mg/g in air atmosphere. This confirms the role of oxide as a retarder of erosion. The retardation of erosion by corrosion has been observed by others as well [8, 10]. A rapid increase in erosion rate occurs in the temperature range of 200 to 650°C. In this temperature range, the role of oxide scale on erosion is fairly small and the rapid increase in erosion rate is believed to be because of the changes in target material properties and microstructure.

Erosion studies under ambient conditions have shown that erosion increases with the increase in strength or the accompanying decrease in ductility. This is basically

due to localized extrusion and ploughing which produce work-hardening so that subsequent repeated impacts on the piled-up material give rise to flake formation and finally the detachment of material. As discussed earlier, the micromechanisms of erosion at high temperature are somewhat different from those at room temperature. The examination of cross-sectional views of the eroded craters in Figure 10 revealed that much higher erosion at 500°C and 800°C was being produced due to the cutting action of the stream of particles into the substrate and tearing by the reflected stream. With erosion being controlled mostly by these two mechanisms, erosion would be expected to increase with decreasing strength. The morphological features in Figures 6 to 9 also support this because the sizes of domains, rub-bands and grooves were all bigger at higher temperatures. Figure 14 shows the variation of tensile strength and ductility with temperature for 430, 304 and 17-4 PH stainless steels. The variation in properties for 416 stainless steel is similar to that of 17-4 PH steel. Since the strength of all stainless steels is decreasing with increasing temperature, their erosion rate is increasing. Ductility is not playing the role in influencing erosion process because all steels have reasonable percent elongation at all temperatures and the role of work-hardening and flake formation leading to the removal of material is greatly diminished due to the considerably greater recovery rate at higher temperatures.

Another factor which may be influencing the erosion of stainless steels is the intergranular precipitation which occurs at high temperatures [13]. It probably contributes to the rapid increase in erosion rate in the temperature range 400 to 650°C. For ferritic stainless steels, a Cr-rich α' phase is precipitated on dislocations and σ phase along grain boundaries when heated in the 400 to 540°C and 500 to 800°C ranges. In martensitic stainless steels heated above 260°C, carbide (or nitride) pre-

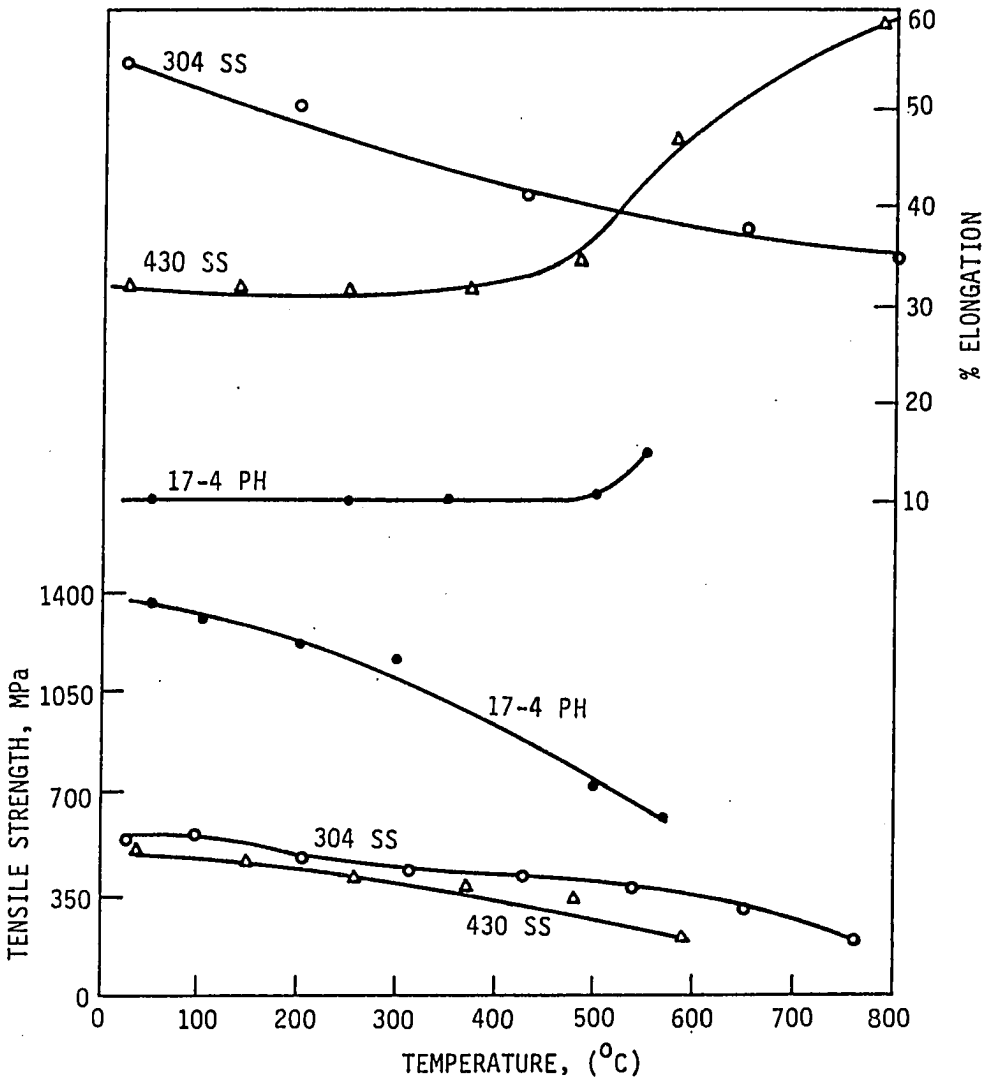

Figure 14: Variation of tensile strength and ductility of stainless steels with temperature [14-15]

cipitation occurs at grain boundaries, especially between 450 to 550°C. In austenitic stainless steels Cr-carbide precipitation also occurs in the grain boundary region. The hard precipitation products along grain boundaries or crystal defects, from a brittle network within the matrix material. Thus, whereas the bulk material has ductile matrix and exhibits ductile properties as in Figure 14, it is brittle in the localized level due to the brittle network at elevated temperatures where such precipitation occurs. Such a material would be very susceptible to external impacts. The evidence of this is seen in Figure 10 which shows microcracking, shatter and detachment of material in erosion pits at 500 and 800°C. Thus the increase in erosion above 200°C is occurring both due to localized precipitation and the decrease in strength.

At temperatures higher than 800°C, the oxide scale thickness increases and the scale manifests spalling tendency [12]. This occurs so because thick scales tend to be brittle and they have internal stresses which promote the rupture of oxide scale and spalling from the surface under external impacts. Such oxide scales would neither be expected to provide resistance to corrosion nor erosion. Consequently, erosion at such high temperatures would be expected to increase considerably and the erosion process would be dominated by rupture and spalling of the oxide scale.

CONCLUSIONS

1. The variation of erosion rate with temperature is similar for all types of stainless steels: ferritic, martensitic, precipitation-hardening and austenitic. Erosion rate virtually remains unchanged up to about 200°C, then it increases rapidly to about 650°C and is followed by a moderate increase up to 800°C.

2. The role of corrosion in erosion from ambient temperature to 650°C is insignificant. The variation of erosion with temperature in this temperature range may be explained in terms of the changes in tensile strength with temperature and the precipitation of chromium carbide in dislocations or grain boundary regions.

3. The exposure of 430 SS to air at about 800°C results in the formation of a strong and pliable oxide film with good adherence to the substrate. This oxide film is resistant to both corrosion and erosion.

4. The exponent of velocity in the erosion-velocity relationship for 304 SS has a value of 1.8 at 500°C compared to 2.0 or above normally obtained for room temperature conditions.

5. The maximum in erosion rate for 304 SS occurs in the impingement angle range of 20° to 30° irrespective of temperature.

6. The shape of curves representing the variation of erosion with temperature for 430 SS is similar for both 30° and 90° impingement angles.

7. Erosion morphology changes with erosion test temperature. The sizes of domains, rub-bands and grooves formed due to the impingement of particles in erosion on the surfaces of high temperature specimens are larger than those at room temperature.

8. It is seen that corrosion influences erosion and whether erosion is less, unaffected or more in the presence of corrosion depends upon the characteristics of the corrosion scales formed.

REFERENCES

[1] Fujikawa, H., H. Makiura, N. Fujino, J. Murayama, M. Yagi, and H. Yuzawa. "High Temperature Corrosion Behavior of Austenitic Stainless Steels for Utility Boilers." In High Temperature Corrosion, ed. Robert A. Rapp, 469-75. Houston: NACE, 1981.

[2] Ishiguro, K., and T. Homma. "Thin Oxide Films on a Ferritic and an Austenitic Alloy." In High Temperature Corrosion, ed. Robert A. Rapp, 28-34. Houston: NACE, 1981.

[3] Natesan, K. "High Temperature Alloy Corrosion in Coal Conversion Environments." In High Temperature Corrosion, ed. Robert A. Rapp, 336-44. Houston: NACE, 1981.

[4] Morrison, C. T., R. O. Scattergood, and J. L. Routbout. "Erosion of 304 Stainless Steel." Wear 111 (1986): 1-13.

[5] Levy, A., J. Yan, and J. Patterson. "Elevated Temperature Erosion of Steels." Wear 108 (1986): 43-60.

[6] Gat, N. and W. Tabakoff. "Some Effects of Temperature on the Erosion of Metals." Wear 50 (1978): 85-94.

[7] Gat, N. and W. Tabakoff. "Effects of Temperature on the Behavior of Metals under Erosion By Particulate Matter." Journal of Testing and Evaluation 8(4) (July 1980): 177-86.

[8] Shida, Y., N. Ohtsuka, and H. Fujikawa. "Influence of Particle Properties on the Solid Particle Erosion Behavior at High Temperature." In High Temperature Corrosion in Energy Systems ed. Michael F. Rothman, 769-80. New York: Metallurgical Society of AIME, 1985.

[9] Levy, A., E. Slamovich, and N. Jee. "Elevated Temperature Combined Erosion-Corrosion of Steels." Wear 110 (1986): 117-49.

[10] Levy, A. and Y-F Man. "Surface Degradation of Ductile Metals in Elevated Temperature Gas-Particle Streams." Wear 111 (1986): 173-86.

[11] Scott, D., ed. Treatise on Materials Science and Technology. Vol. 13, 287-319. Erosion Caused by Impact of Solild Particles, by G. P. Tilly. New York: Academic Press, 1979.

[12] Brasunas, A. des. Corrosion Basics. Houston: National Association of Corrosion Engineers, 1984.

[13] Smith, W. F. Structure and Properties of Engineering Alloys. New York: McGraw-Hill Book Company, 1981.

[14] Metals Handbook, Vol. 1, 8th Edition. Metals Park: American Society for Metals, 1961.

[15] Mechanical and Physical Properties of the Austenitic Chromium-Nickel Stainless Steels at Elevated Temperatures. New York: International Nickel Company, Inc., 1963.

[16] Metals Handbook, Vol. 3, 9th Edition. Metals Park: American Society for Metals, 1980.

PART II.

FURTHER INVESTIGATIONS ON THE ELEVATED TEMPERATURE EROSION-CORROSION OF STAINLESS STEELS

ABSTRACT

The erosion-corrosion behavior of four representative types of stainless steels is reported and compared to the work of others. The characteristics of oxidation and the properties of oxide scale are examined by scanning electron microscopy, dynamic ball impact, and scratch tests. The effect of operating parameters on erosion-corrosion is studied by varying the temperature, impingement angle and velocity, particle size, and erodent concentration. The features of eroded-corroded zones and substrate deformation are examined. It is found that below 650°C elevated temperature erosion is dominant and above it the interactions between erosion and corrosion play an important role. Above 200°C the erosive mass loss rate increases with increasing temperature, but the rate of increase is found to be heavily dependent upon particle concentration. The latter is found to have a great influence on erosion-corrosion and so is considered to be a major operating parameter at elevated temperatures. The mechanisms of erosion-corrosion with particular emphasis to the interaction between erosion and corrosion are discussed. Four possibilities for the damage or loss of material by impacting particles in elevated temperature erosion-corrosion situation are suggested and related to the actual features observed on the eroded-corroded surfaces.

INTRODUCTION

The study of the combined erosion-corrosion behavior of metallic materials at elevated temperatures has lately been drawing considerable attention because of its economic significance. The damage resulting from erosion-corrosion is a serious problem in many industrial applications. Since it affects the operational life and the efficiency of a component or system, it has become an important design consideration in many situations.

Stainless steels are extensively used for exposure to elevated temperatures in exhaust systems, combustion chambers, turbine blades, coal gasification systems, etc., which involve an erosion-corrosion environment. As such the elevated temperature combined erosion-corrosion behavior of these materials deserves to be studied. As for the elevated temperature corrosion of stainless steels, it has been studied most extensively and reported in the literature [1-3]. Some investigators have studied the erosion of stainless steels under ambient conditions [4]. As for elevated temperature erosion, some test results on the erosion of stainless steels at about 205°C were reported [5] in 1977, and Tabakoff and coworkers [6, 7] later reported the erosion behavior at a higher temperature of 649°C. A study on the elevated temperature erosion of steels, including some stainless steels, was conducted in undried nitrogen atmosphere to avoid the analysis of the erosion mechanisms as complicated by simultaneous corrosion [8]. Gradually the emphasis on investigations has shifted to combined elevated temperature erosion-corrosion [9-13]. An extensive review of the elevated temperature erosion-corrosion work on stainless steels was provided in our earlier work [9].

The realization that the mechanisms of elevated temperature erosion-corrosion were not well-understood together with the potential for the use of stainless steels in elevated temperature erosive environments led to our earlier work [9] on the various kinds of stainless steels: austenitic, ferritic, martensitic and precipitation hardening types. The present work is a continuation of that work. It supplements our earlier work with the additional data and aspects not studied earlier, and complements it with the recent work of others on stainless steels and also some other chromium-containing steels. Its purpose is to present a coherent understanding of the mechanisms of combined erosion-corrosion, with emphasis on the interactions between erosion and corrosion, and of other aspects.

EXPERIMENTAL

Erosion-corrosion experiments were performed using a vertical sand-blast type of elevated temperature test rig described in detail in PART I. The carrier gas used for accelerating erodent particles was air. It is the most common oxidizing environment encountered in industrial practice. The temperature range of the investigation was from ambient to 800°C.

The materials selected for the investigation were 430, 304, 416 and 17-4 PH stainless steels. These represent the four main groups of stainless steels, namely the ferritic, austenitic, martensitic and precipitation hardening, in the same order. Their chromium contents range from 12 to 20%. The same heat treatment conditions as reported in PART I were used, that is, the ferritic 430 SS and the austenitic 304 SS were used in the annealed condition, 17-4 PH steel was double aged, and the martensitic 416 SS was austenitized at 980°C and tempered for 1 hour at 205°C. After heat treatment the specimens were ground and polished by abrasion against emery paper in running water sequentially down to 600 grade finish.

The commercial silicon carbide particles in 120, 240, 320, 400 and 600 grit sizes, supplied by the Buehler Corporation, were used as erodents. Two different erodent mass flow rates, 0.0421 g/mm^{2}s and 0.0026 g/mm^{2}s, were used for investigating the influence of erodent concentration on elevated temperature erosion-corrosion. Most of the erosion-corrosion experiments were done with an impingement angle of 30°, but in some experiments the impingement angle was varied from 10° to 90°. The particle impingement velocities at different test temperatures were measured by the double-disk arrangement. The velocity range used in some experiments was from 55 m/s to 128 m/s, but most experiments were done with an impingement velocity

of 65 m/s. Whereas some of the test conditions may be somewhat severe in terms of practical erosion, the results obtained reveal fairly well the features of elevated temperature erosion and thus help to understand the underlying mechanisms.

The erosion experiment on any specimen lasted for 110 minutes. In the case of erodent mass flow rate of 0.0026 g/mm^2s, the specimen was continuously impacted with a total of 100 g erodent particles. In the case of higher mass flow rate of 0.0421 g/mm^2s, the 100 g erodent particles were impacted in ten steps of 10 g each, every 10 minutes between each step, and during a fraction of 10 minutes the specimen was not impacted by the particles. Erosive mass loss rate was calculated by dividing the specimen mass loss by the total mass of erodent particles impacted. The elevated temperature corrosion-only experiments were performed in two ways: static where the specimen was heated in furnace and no air was impinging, and dynamic where the specimen was heated in the same test rig and subjected to the same air flow rate as used in the erosion-corrosion experiments (but the air stream was devoid of particles). The surfaces of the corroded and eroded-corroded specimens were studied by scanning electron microscopy. Some of the eroded specimens were sectioned to reveal the cross-sectional features.

RESULTS AND DISCUSSION

Oxidation Characteristics

When the clean surface of an alloy with the ability to form protective oxide scale is exposed to elevated temperature in an oxidizing environment, three stages of oxidation are typically exhibited, as shown in Figure 1 [14]. The duration of the first stage which is transient in nature is fairly short, and the oxidation rate is high. During this stage, oxides of all the reactive elements on the alloy surface form and the amount of each is roughly proportional to the concentration of the element in the alloy. The extent of oxidation depends on the relative amounts and the growth rates of the oxides formed. In steady-state oxidation the rate of oxidation is controlled by the growth of a protective oxide scale, which is a solid-state diffusion-controlled process. As oxide scales thicken, stresses develop and cause failure of the scales and the onset of breakaway oxidation by the stress relief mechanisms such as blistering, tensile or shear scale-cracking, etc. The onset of breakaway behavior is also related to the penetration of protective oxide scales by cations from the base metal or anions from the environment.

Stainless steels are typical of the alloys which form protective film during oxidation. In elevated temperature erosion-corrosion the oxidation behavior during the first and second (particularly, the early part of it) stages is of interest. As such the extent of oxidation and the nature of the transient oxidation products are of concern. When the test conditions lead to high erosivity, the erosion-corrosion process becomes erosion-dominant, and the corrosion process in this case will relate to transient oxidation. If the process is corrosion-dominant, steady-state oxidation will

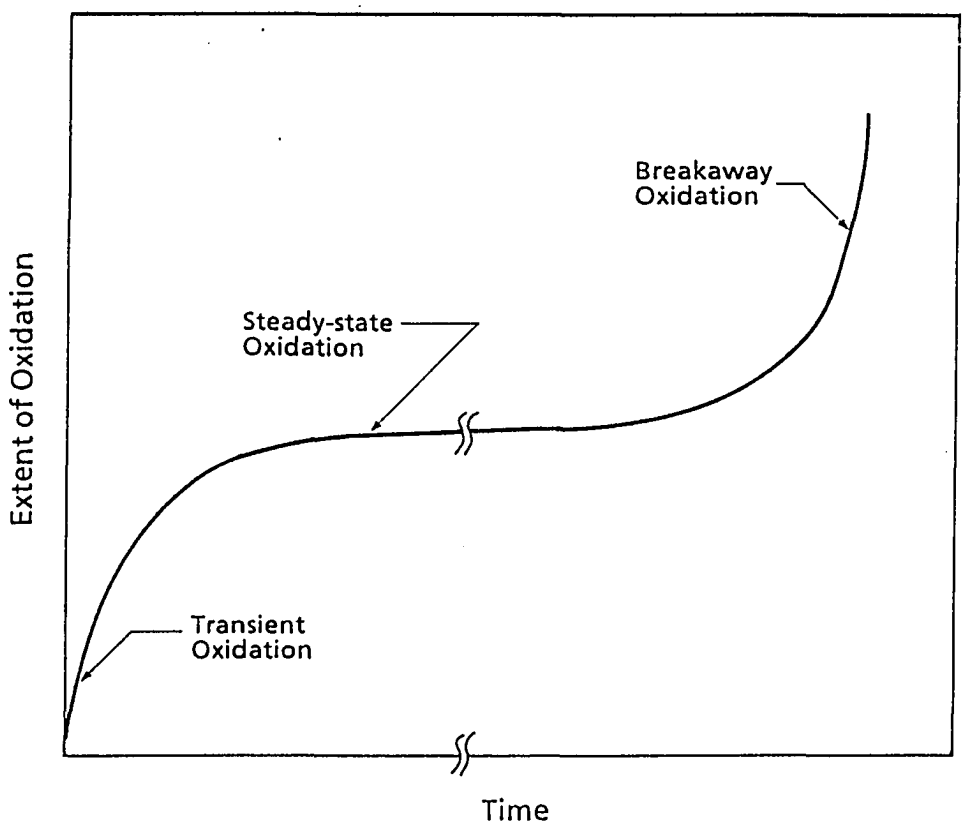

Figure 1: Schematic representation of the extent of oxidation (i.e. weight change per unit area or scale thickness plus depth of internal oxidation) as a function of time [14]

be the relevant mechanism. In other cases, erosion-corrosion will involve both the transient and steady-state oxidation processes.

For stainless steels the oxidation rate up to 550°C is extremely low while it becomes significant above 700 °C [9]. The mass gain obtained by exposing to air all the four kinds of stainless steels tested in this work at 800°C for 110 minutes was 0.1-0.4 mg on a specimen of the size $25.4mm \times 19.0mm \times 3.2mm$. It amounted to $(0.8-3.2)\times 10^{-4} mg/mm^2$ surface area. These corrosion tests were carried out under both the static and dynamic conditions, and there was no significant difference in the mass gain values found. Levy et al. [10, 13] reported from their observations on a series of other chromium-containing steels that there were essentially no differences in the oxide scale thickness, morphology and composition between the short-time static and dynamic corrosion exposures.

The oxidation features on the surface of 430 SS exposed to air at 650°C for 10 minutes are shown in Figure 2 (a). It may be seen that during this short time oxide crystallites initiated and grew to about 0.05 μm size. They seem to have initiated preferentially in the defect locations such as scratch marks. The oxide scale formed is neither uniform nor continuous due to the slow oxidation rate at this temperature. Due to its sparse nature, this oxide scale would not be expected to play any significant role in the elevated temperature combined erosion-corrosion process. Therefore, it is believed that at the temperatures 650°C and below the erosion-corrosion of stainless steels is basically an erosion-dominant process, and the variation in erosion rate with temperature within this range is basically due to the changes in the temperature-dependent properties of the materials.

Oxidation becomes fairly profound when stainless steel is exposed to air at 800°C

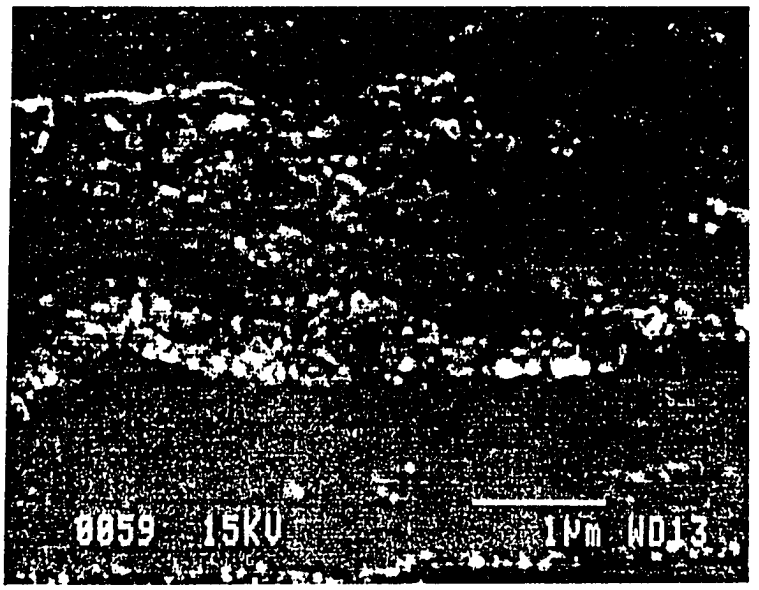

a

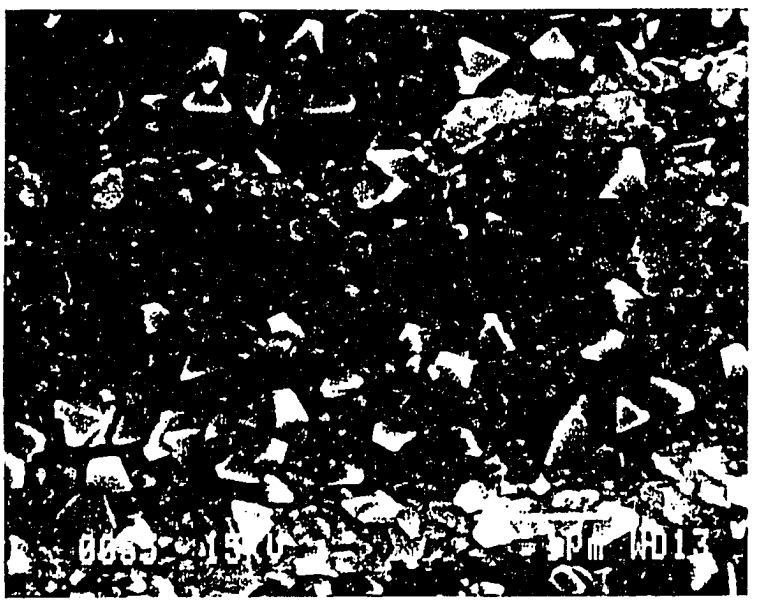

b

Figure 2: Morphology of high-temperature corroded surfaces of 430 SS exposed to air at the temperatures and times given: (a) 650°C, 10 min; (b) 800°C, 10 min; (c) 800°C, 110 min; (d) same as (c) but at a higher magnification

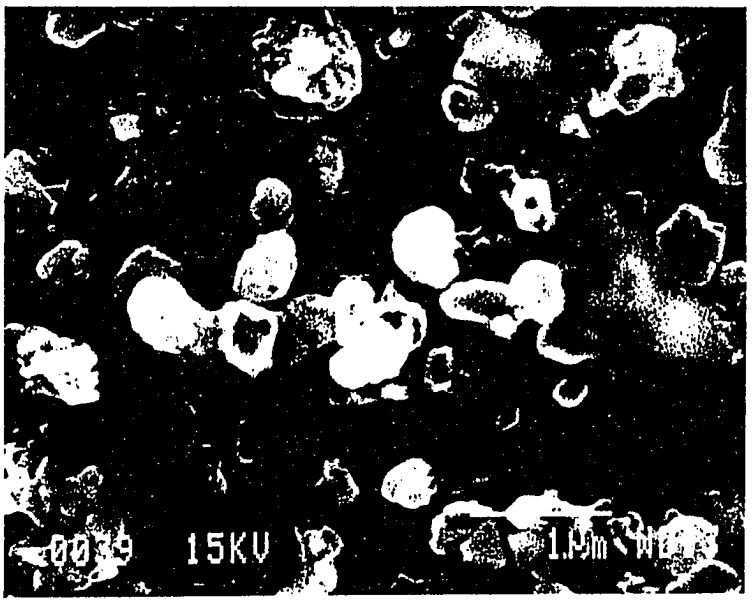

c

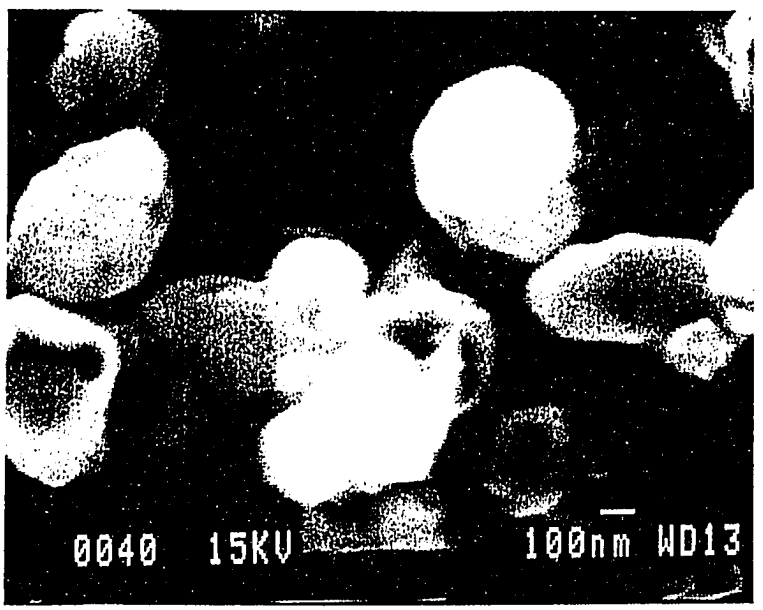

d

Figure 2 (Continued)

Table 1: Oxides determined by x-ray diffraction analysis of the eroded-corroded surfaces of Cr-steels [13]

Alloy	Oxides
2.25Cr1Mo	γ-Fe_2O_3
5Cr0.5Mo	γ-Fe_2O_3, $FeCr_2O_4$
9Cr1Mo	γ-Fe_2O_3, $FeCr_2O_4$
410SS (12Cr)	γ-Fe_2O_3, $FeCr_2O_4$, Cr_2O_3
304SS (19Cr9Ni)	γ-Fe_2O_3, $FeCr_2O_4$,Cr_2O_3
310SS (25Cr20Ni)	NiO, $FeCr_2O_4$, Cr_2O_3

even for a short duration of 10 minutes. In this case, the oxide nuclei formed grow laterally to yield a continuous film on the surface. This can be seen in Figure 2 (b) where the oxide crystallites have covered the entire surface thereby providing the appearance of a monolayer of oxide scale with some overlap only in discrete locations, possibly of defects. The bulk of the crystallites are 0.15 μm in size while some are more than double this size. These larger crystallites resulted from the growth of pre-existing preferentially-nucleated oxide crystallites. These could be interpreted in terms of the Ostwald ripening, i.e., the nuclei which are formed near a large particle are dissolved away and the larger particles grow at the expense of the smaller ones in an effort to reduce surface energy. All of the crystallites are in the shape of multi-faceted polyhedra. After a prolonged exposure of 110 minutes, the multilayer deposition of crystallites results in a thicker oxide scale, as shown in Figure 2 (c). It is noted that the contribution to the thickening of oxide scale comes from three processes: the growth of pre-existing crystallites, the initiation of new crystallites, and the agglomeration of crystallites. Figure 2 (d) which shows these crystallites at a much higher magnification indicates that the crystallites which were initially multifaceted became round with longer exposure times.

During oxidation several types of oxides are formed. Table 1 gives the kinds of oxides reported by Levy and Man [13], as determined by the x-ray diffraction analysis of the eroded-corroded surfaces of steels containing Cr.

In an erosion-corrosion process, corrosion on a surface is accelerated by the erosion damage. The evidence to this effect was obtained by heating a specimen containing both the undamaged and the erosion-damaged zones and examining the features in these two zones. These features are seen in Figure 3 where one sees the crystallites in two sizes: those nucleated earlier and appearing as widely-spaced fast-growing big particles, and the ones nucleated later appearing as small particles covering the surface uniformly and giving the appearance of a monolayer. Both sizes of crystallites are larger in the erosion-damaged zone than the corresponding crystallites in the undamaged zone. The agglomeration of crystallites, which is an indication of further oxidation, is also seen in the severely damaged location. The oxidation will be much more enhanced under concurrent impacting and heating as involved in a real erosion-corrosion situation. The stimulated scale-growth by impacting particles was quantitatively verified by holding the undamaged and erosion-damaged 304 SS specimens at 950°C for 20 minutes and at 1000°C for 45 minutes. In both the cases, the mass gain of the damaged specimen was about twice that of the undamaged specimen. The difference in mass gains occurs partly from the accelerated oxidation rate and partly from the increased contact surface area because of the eroded surface topography. Levy and coworkers [10, 13, 15] also made similar observations in the case of 310 SS, 410 SS and other materials. By examination of the scale morphology of 9Cr-1Mo steel, they established that the impact of erodent particles on the surface undergoing corrosion at 750°C produced a scale which occurred in a corrosion-only

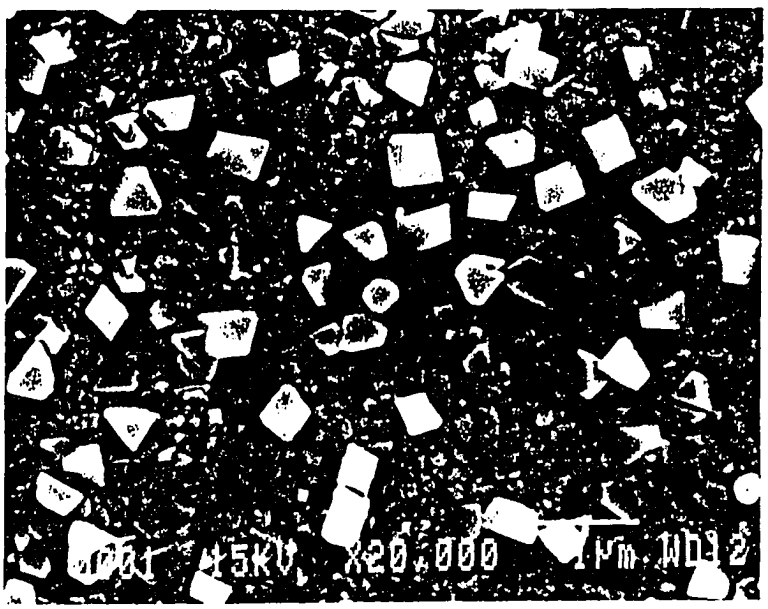

a

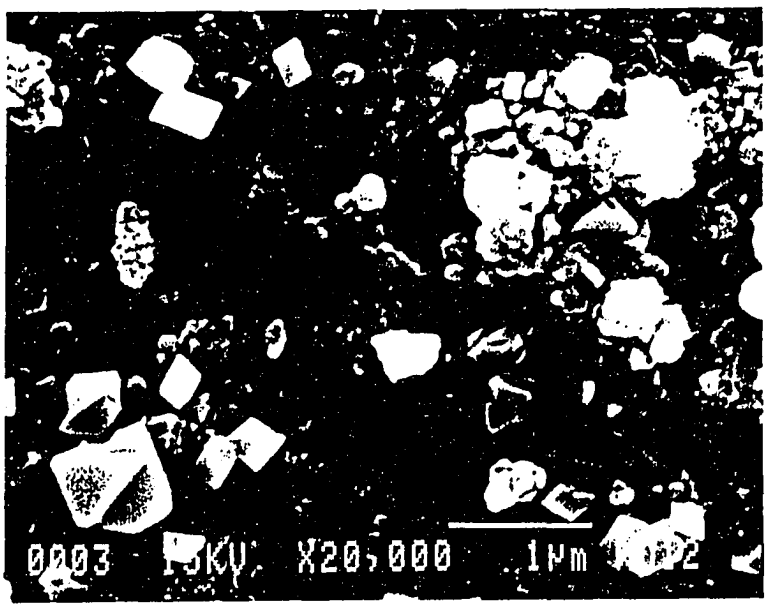

b

Figure 3: Surface morphology of (a) undamaged and (b) erosion-damaged (at room temperature) areas of a 430 SS specimen exposed to 800°C for 40 minutes after erosion

test at a temperature 150°C higher.

The mechanism of the accelerated oxidation discussed above depends upon the fact that oxide nucleation is favored at the sites of higher energy such as the surface defects in the form of dislocations, grain boundaries, impurities, etc. The impacting particles produce localized plastic deformation and thereby induce numerous dislocations in the surface layer. It increases the density of surface defects which serve as locations for the nucleation of oxide. This can be seen in Figure 2 (a) where crystallites nucleated preferentially around scratch marks. Some of these older crystallites later annihilate the newly-formed small crystallites.

The impacting particles change both the composition and the structure of oxide scale. Levy [16] reported that the corroded surface of 410 SS had an upper layer of iron oxide separated by a line of voids from the lower layer of the same thickness of iron oxide. On the other hand, the erosion-corrosion scale had a thinner upper layer of iron oxide and a much thicker lower layer of iron oxide.

Oxide Properties

The oxide scales formed on stainless steel surface are protective because they serve as good solid-state diffusion-barriers between the alloy and the environment which prevents the base metal from being further corroded. The adhesion and hardness are the two properties which could affect the resistance to spalling and mechanical damage from particle impacts. In order to determine the adhesion of oxide film to the base material under impact deformation conditions, a dynamic impact test was carried out by impacting a steel ball of 3.18 mm diameter on a 430 SS specimen surface preoxidized at 800°C for 40 minutes. As seen in Figure 4, the crystallites of

oxide on the impacted surface seem to be consolidated and condensed, and appear to have undergone plastic deformation along with the base material because the oxide film stays mostly unbroken. There is no crack seen either, even around the edge of the impacted indentation, which is typically observed in the case of brittle materials. Whereas, there are some locations within the bounds of indentation where the oxide scale appears to be thin, there is no evidence showing that the scale was separated from the substrate.

The adhesion, deformation and strength of the oxide were further checked by a scratch test. The oxide scale was scratched with a Talysurf diamond stylus under a load of 6.3 g. It produced a scratch of 6 μm width. Figure 5 shows that with the traverse of stylus the oxide scale has been completely condensed and deformed thereby providing a flat and smooth appearance. There are no cracks and there is no indication of spalling in and around the deformed region. These observations lead to the conclusion that the oxide scale formed on the stainless steel surface is pliable, and strongly adherent to the substrate. These observations are consistent with our conclusions drawn from a quasi-static indentation made on a preoxidized 430 SS [9]. Similar characteristics of the oxide scale in the dynamic eroded-corroded zone will be presented later.

The microhardness reading with 100 g load on the surface oxidized at 800°C for 110 minutes was 178 DPH as compared to 163 DPH on the substrate beneath it. The higher value of hardness in the former case indicates that the stainless steel surface with oxide on it is stronger than in the latter case. We could thus conclude that the oxide scale formed on the stainless steel surface is hard, pliable and adherent to the base metal. In a situation like this where oxide acts as a barrier between

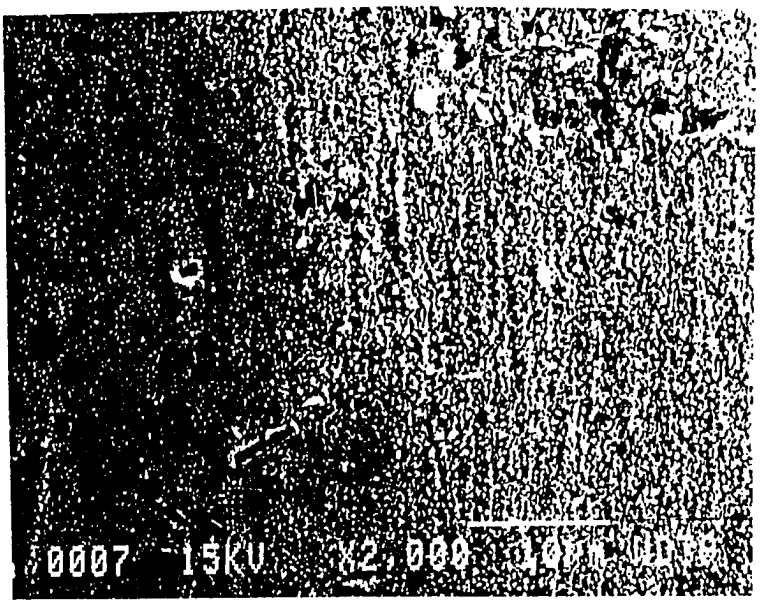

Figure 4: Single ball impact on the surface of 430 SS oxidized at 800°C for 40 minutes

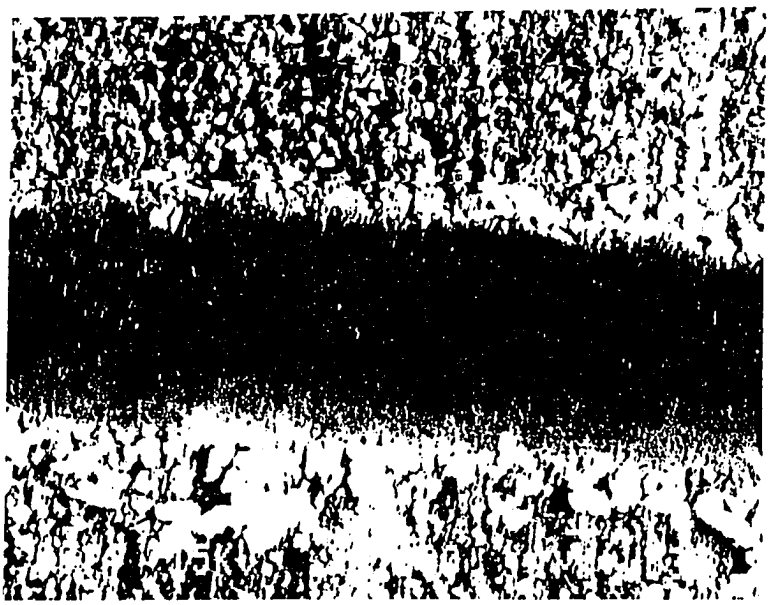

a

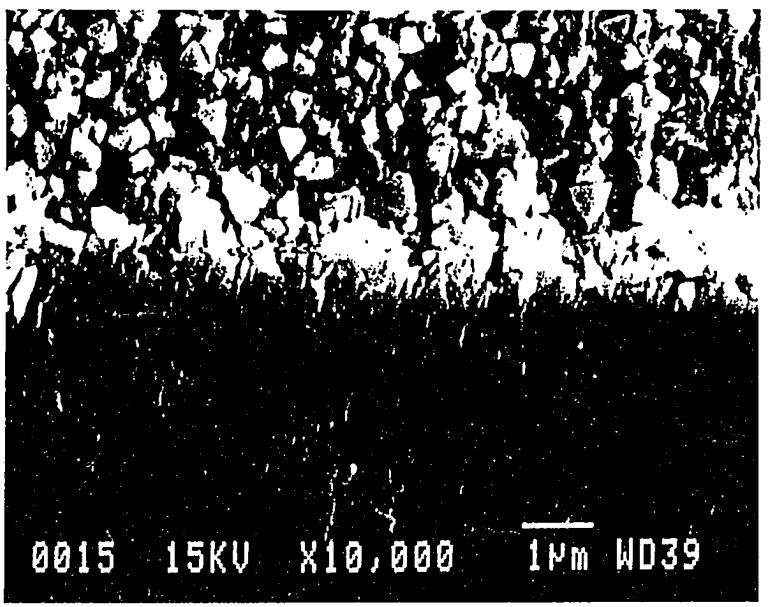

b

Figure 5: Oxide scale deformation from scratching on the surface of 430 SS oxidized at 800°C for 40 minutes

the base metal and its surrounding, which may be either a elevated temperature environment or a stream of impacting erodent particles, oxide would be expected to play a significant role in the erosion-corrosion process.

Effect of Operating Parameters

The operating parameters considered in this study were the temperature, impingement angle, particle velocity, particle size, and erodent concentration.

Temperature The erosive mass loss of material was measured at six different temperatures: room temperature, 200, 400, 500, 650, and 800°C. Figure 6 shows the variation of mass loss rate (which is the mass loss of target divided by the mass of erodent particles impacted) with temperature in the presence of corrosion for stainless steels at an impingement angle of 30°, velocity of 65 m/s, and an erodent concentration of 0.0421 g/mm^{2}s. It would be noted that the trend in the variation of mass loss rate with temperature is basically similar for all the kinds of stainless steels. As the temperature increases above ambient, mass loss rate remains unchanged up to 200°C. It then increases rapidly up to 400°C and there is a moderate increase occurring from 400°C to 800°C. The mass loss rate of the ferritic 430 SS is the lowest of all steels at any temperature.

At the end of elevated temperature erosion-corrosion tests, a thin layer of oxide film with temper color was observed on the surfaces of the specimens exposed to 400°C, and with a color indicative of severe heat-damage at higher temperatures. Since no perceptible mass gain was measured in the case of specimens exposed to as high a temperature as 650°C for 110 minutes and only a small gain for those exposed

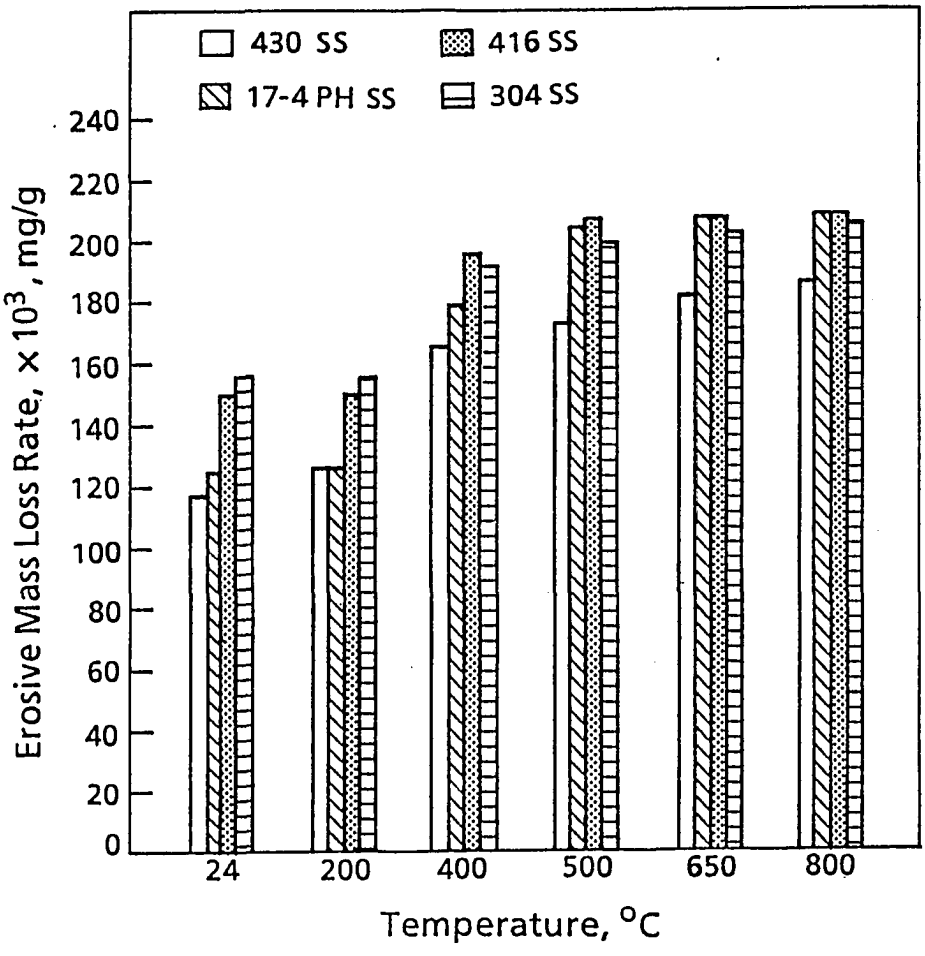

Figure 6: Temperature dependence of erosive mass loss rate for various kinds of stainless steels: $v = 65$ m/s, $\alpha = 30^{\circ}$, 120 grit size SiC particles, erodent concentration 0.0421 g/mm^{2}s, accelerating gas air

to 800°C for the same period of time, it seems reasonable to assume that the oxide film formed was very thin. As the mass loss rate in erosion tests up to 200°C is about the same as at room temperature, it is concluded that oxidation played no role in this temperature range. The erosive mass loss rate increases significantly from 200 to 400°C while there is no significant oxide formed in this temperature range. The erosion variation in this temperature range is thus believed to be because of the changes in material properties and microstructure. This was demonstrated in our earlier work [9]. Since in the temperature range 650 to 800°C, there was significant oxidation but a mere negligible change in mass loss rate from erosion, it is believed that the oxide film played here a significant role in providing protection from erosion. This aspect will be further pursued later.

In our erosion experiments, there was no decrease in erosion rate observed with the increase in temperature up to 800°C (Figure 6). On the other hand, some investigators have reported the decrease in erosion rate occurring beyond a certain temperature. Figure 7 [17-18] shows this kind of behavior particularly for Cr-Mo steels. The leveling in erosive mass loss rate in the temperature range 650-800°C (Figure 6) suggests that we could also observe the decrease in mass loss rate at higher temperatures.

Impingement angle In our earlier work [9], it was reported that the maximum erosive mass loss rate for 304 SS at the impact velocity of 70 m/s occurred at about 30° for room temperature and at 20° for 500°C. Tabakoff et al. [6] reported similar variation of the mass loss rate with impingement angle for this stainless steel at the temperatures of 316, 482, and 649 °C, and at the considerably higher velocities of

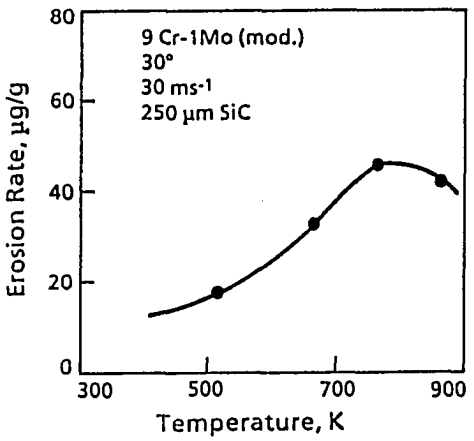

a

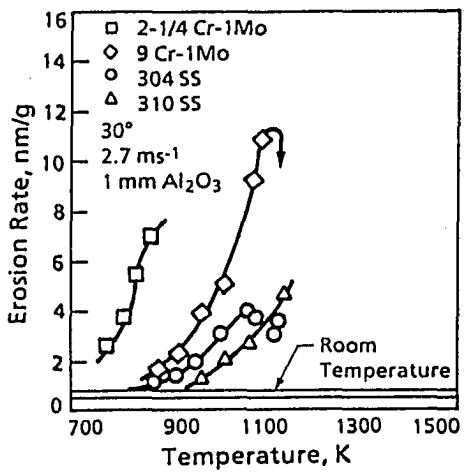

b

Figure 7: Erosion rate vs. temperature for some stainless steels and other Cr-steels: (a) 9Cr-1Mo steel [17]; (b) 304, 310 SS and Cr-Mo steels [18]

183, 244, and 305 m/s. The maximum in mass loss rate within 20° to 30° is typical of ductile materials. This indicates that the mechanism of material removal in erosion does not change with either the increase in temperature or impact velocity. Since in brittle materials the maximum erosion occurs under normal impact conditions, it indicates that the plastic deformation is the dominant mode of material removal in elevated temperature erosion-corrosion.

Impingement velocity Our earlier erosion-corrosion studies [9] on 304 SS at 500°C indicated that mass loss rate is directly proportional to $(velocity)^{1.8}$. Since the velocity exponent reported under ambient conditions is 2 or above [4, 19], it implies that the mass loss rate at elevated temperatures is less sensitive to impingement velocity. Other investigators also observed the decreased sensitivity of mass loss rate to velocity at elevated temperatures. Levy et al. [8] found that the velocity exponent of 310 SS at 800°C was 1.23, which was only one-half of its room temperature value. Tabakoff et al. [6] also found the velocity exponent of less than 2 for 304 SS at 316, 482, and 649°C. The increased toughness and decreased strength at elevated temperatures could account for the decreased sensitivity to impingement velocity since these changes in properties would enable more energy of the impacting particles to be absorbed by the target material during impacting process.

Particle size Figure 8 shows the erosive mass loss rate of 304 SS by erosion-corrosion at 650°C with varying particle size. The mass loss rate increases rapidly with increasing particle size up to 40 μm beyond which there is no significant difference. This kind of variation is similar to that normally observed under room temperature condition. It should be noted that the difference in mass loss rate for

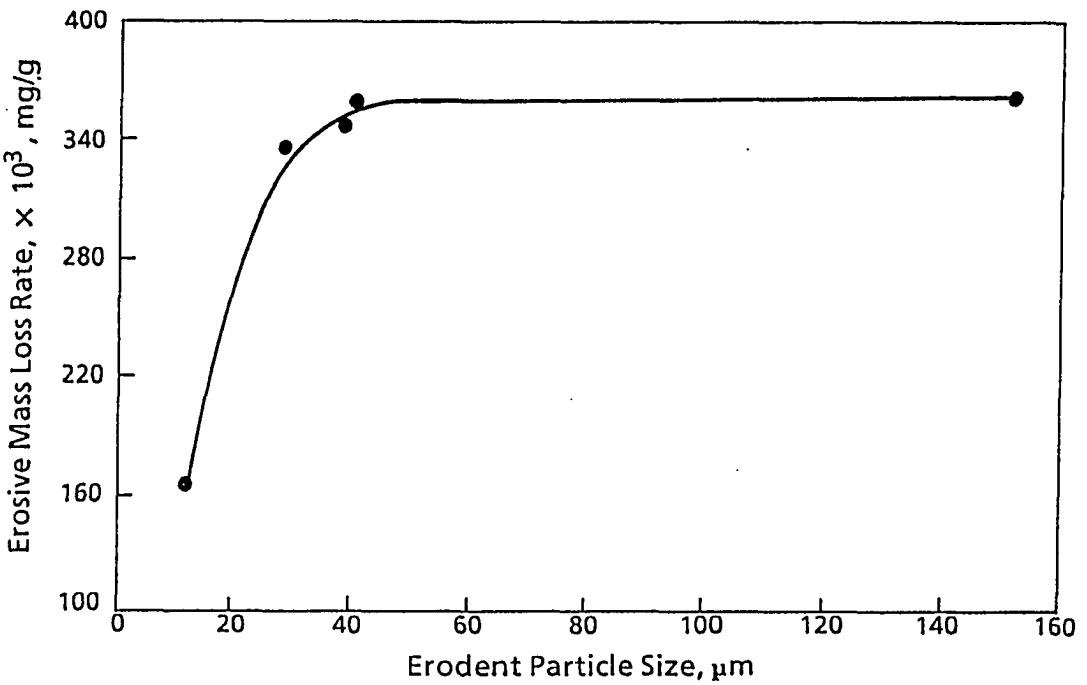

Figure 8: Variation of erosive mass loss rate of 304 SS as a function of particle size: temperature 650°C, velocity 65 m/s, erodent concentration 0.0026 g/mm^{2}s

the particles ranging in size from 28 to 151 μm is extremely small. This variation is explained in terms of the erosivity of different particle sizes. It is stated that the larger particles are more erosive than smaller particles, the angular particles are more erosive than smoother particles, and that the particle shape and size are closely related. SEM examination of the erodent particles in various grit sizes showed that the coarsest 120 grit particles were more angular than the finest 600 grit particles, and the angularity of particles in other grits was within these two extremes [20]. If all other conditions are fixed, the erosivity of particles is, to a great extent, dependent upon their angularity.

Levy and Man [21] measured the erosion of 9Cr1Mo steel at the temperature of 650 °C, impingement angle of 90° and velocity of around 60 m/s with the SiC particles in sizes 76, 130 and 280 μm. They found that the erosion by 76 μm particles was approximately the same as by 130 μm particles. This is consistent with the erosion behavior presented in Figure 8. They also found that unlike the behavior of metals where the erosion rates for particle sizes between 100 and 200 μm are generally similar [22] and become independent of particle size above some critical value [23-24], the erosion rate for 280 μm SiC was still significantly higher than for 130 μm at all velocities from 25 m/s to 85 m/s.

Figure 9 shows the erosive mass loss rate of 304 SS with varying sizes of particles, all accelerated in the air stream at a constant pressure of 0.0932 MPa and a temperature of 650°C. The unshaded portions represent the decrease in erosion rate due to the decrease in particle size while the shaded portions represent the net effect of the increase in erosion rate due to the increase in particle velocity. The latter occurs because the finer the particle the faster it is accelerated at a constant gas

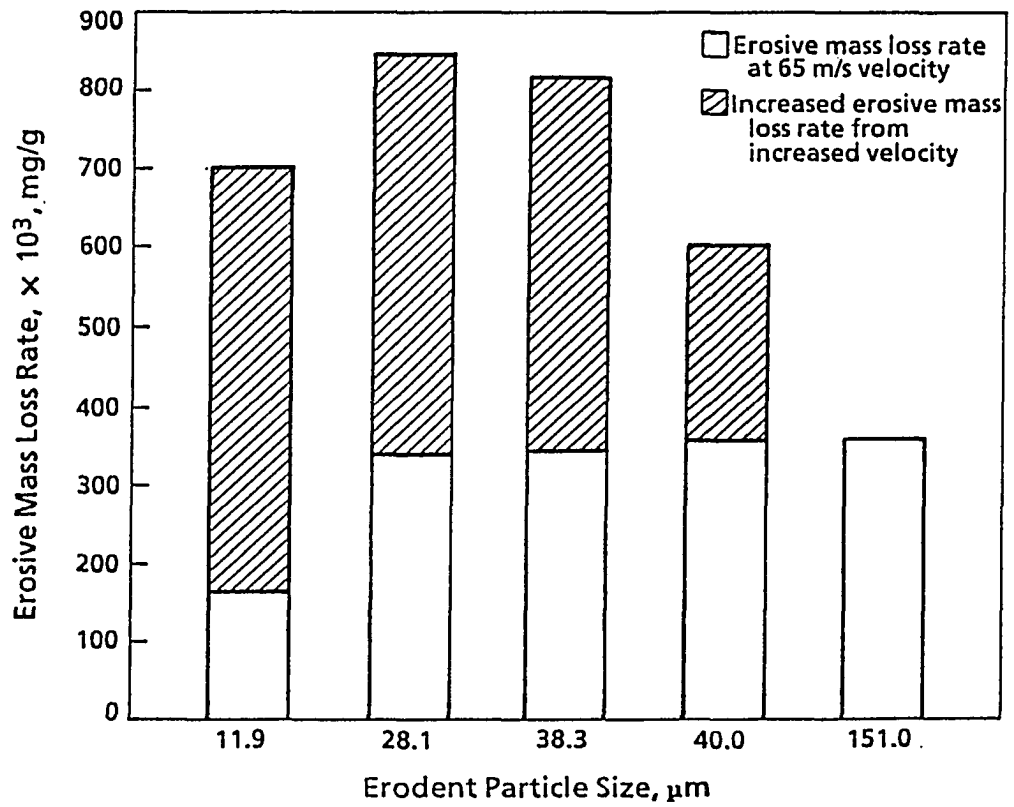

Figure 9: Erosive mass loss rate of 304 SS by different size particles accelerated with a constant air pressure of 0.0932 MPa: temperature 650°C, impingement angle 30°, erodent concentration 0.0026 g/mm^{2}s

pressure. It should be noted that the erosion rate increases with decreasing particle size except for the 600 grit size. This peculiar behavior of 600 grit size could be for two reasons: considerable reduced angularity and the inability of light particles to produce substrate deformation beyond the threshold level for erosion. It is thus seen that although the particle size in the range of 28 to 151 μm is not a big contributor to erosion rate change at elevated temperature and constant velocity, it manifests its effect on erosion rate through the fact that finer particles travel faster when accelerated in a fluid stream at constant pressure.

Erodent concentration It is generally considered to be a minor factor in the erosion at room temperature and so relatively less work on this aspect has been done. A decrease in erosion rate with increased sand concentration was reported in a slurry jet test [25]. Similar behavior has been reported for gas stream jets as well. Thus the general consensus is that erosion is reduced with increased erodent concentration. While, in general, the reduction in erosion could be small, in some cases a reduction as large as 50% has been reported for a fortyfold increase in concentration [19]. At elevated temperatures the effect of erodent concentration on mass loss rate is much more profound and so it becomes a significant variable. The variation of erosive mass loss rate with temperature for two erodent concentrations and two kinds of stainless steels is shown in Figure 10. It should be noted that there is no effect of erodent concentration on erosive mass loss rate up to 200°C. There is considerable difference in the erosive mass loss rate for two different concentrations at higher temperatures, and the higher the temperature, the greater is the difference. The erosive mass loss rate for both materials at 800°C at a particle flow rate of 0.0026 g/mm^{2}s is close to

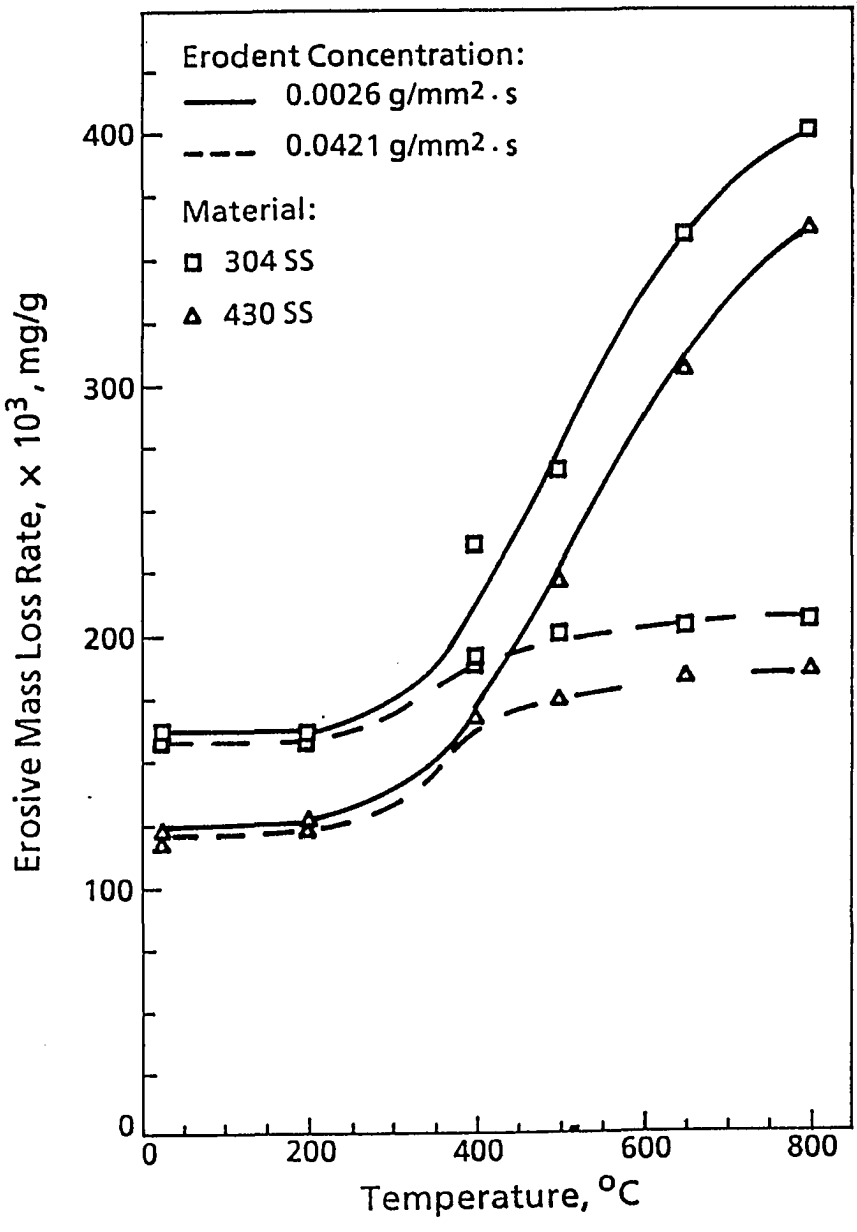

Figure 10: Variation of erosive mass loss rate of 430 SS and 304 SS with temperature for two erodent concentrations

twice that at 0.0421 g/mm^{2}s.

The variation of erosion with erodent concentration may be explained by considering the phenomena such as the interaction between the impinging particles and target material, time available for oxidation, intercollision between particles, mechanisms responsible for material removal and the like. A stream of particles travelling in a tube has a velocity distribution associated with it, that is, there is a range of velocities with an average velocity at the highest frequency [26]. The velocity differences occur not only between the particles at stream center and edges, but the particles in any flow plane are also moving at somewhat different speeds. In addition, the erodent particles have a size distribution along with the variation in angularities or shapes [27]. Considering these factors, we may express the erosivity (which is defined as the ability of an impacting particle to cause virtual damage or material removal) E of an individual impact particle as a function of the impingement velocity v, size s and angularity α, etc. as follows:

$$E = f(v, s, \alpha, ...)$$

It is reasonable to assume that the erosivities of a stream of particles would follow the Gaussian distribution as shown in Figure 11. For any erosion situation, there is expected to be a critical value E_C which implies that only those particles whose E is equal to or greater than E_C would participate in the virtual damage or removal of target material. Such particles could be called the active particles, and in the same sense, those particles whose impact would not contribute to either virtual damage or removal of target material (because E < E_C) as the dummy particles. Obviously, E_C is heavily dependent on temperature, since it increases with the increase in strength or the accompanying decrease in ductility of target material, and the strength of

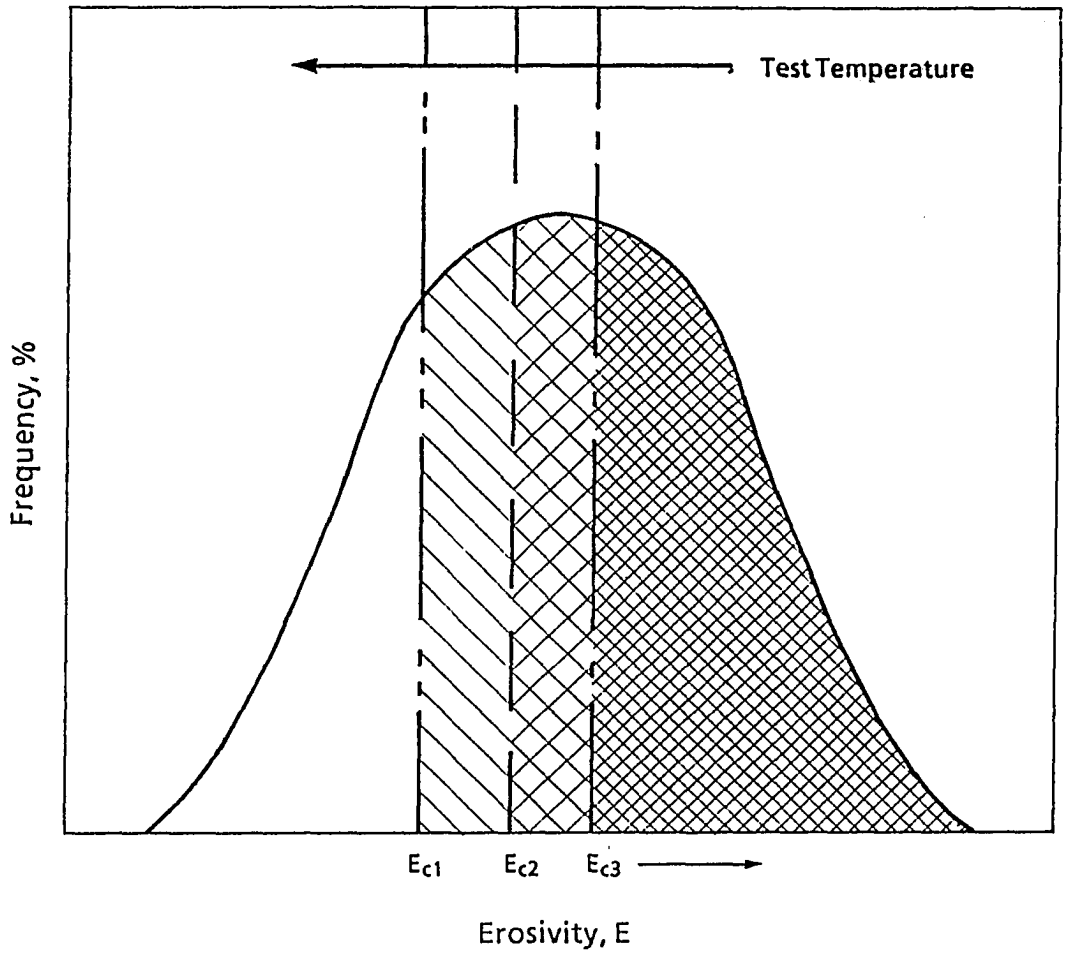

Figure 11: Schematic representation of erosivity distribution of the erodent particles in a fluid stream and the temperature-dependence of critical erosivity. The area bound by the curve to the right of E_C line represents the percentage of active particles

stainless steels is reduced by 60% or more over the temperature range from ambient to 600°C [9]. Erosion under ambient conditions involves localized extrusion and ploughing which produce work-hardening so that the subsequent repeated impacts on the piled-up material give rise to flake formation and finally the detachment of material. The same mechanism would apply to elevated temperature erosion as well with the exception that work-hardening may not occur at fairly high temperatures. In other words, elevated temperature fatigue would be the viable mechanism. It was further shown in our earlier work [9] that cutting action of the stream of particles into the substrate and tearing by the reflected stream also plays role in elevated temperature erosion. With the removal of material being controlled mostly by these two mechanisms, erosive mass loss rate would be expected to increase with decreasing strength. Since the strength of all stainless steels decreases with increasing temperature, their erosive mass loss rate would vary with temperature as shown in Figure 6. It would thus also follow that E_C would be lower at higher temperatures.

As the erodent particles accelerated in a gas stream approach a target surface, some of these will collide with the reflected particles. The higher the erodent concentration, the greater will be the number of particles undergoing interparticle collisions and vice versa. As a result of collisions, two kinds of events occur because of the distributions of the size and velocities of particles in the fluid stream. The incoming high-energy particles get deflected but are still able to impact the target surface. They participate in erosion irrespective of the temperature. On the other hand, the incoming low-energy particles (because of either low mass or low velocity) are pushed out of the erosion zone and so do not participate in erosion. The percentage of such particles is lower with lower erodent concentration because of the reduced likelihood

of interparticle collisions. In other words, some of the low-energy particles that are thrown out of the erosion zone at high erodent concentration are able to impact in the erosion zone at low erodent concentration level. In spite of their low energy, these particles effectively erode the target surface at elevated temperatures but are not able to do so at room temperature because the E_C needed for erosion at this temperature is higher than that needed at elevated temperatures. Consequently, whereas the erosive mass loss rate at elevated temperatures is lower with greater erodent concentration, it is virtually unaffected at room temperature by erodent concentration.

At elevated temperatures corrosion becomes an important factor in the erosion-corrosion process. At any instant, a part of the impact zone is exposed to impacting particles while the remainder is exposed to carrier gas and so to the corroding effect of it. Thus, with lower erodent concentration relatively fewer particles will be contacting the target at a particular instant and so a larger part of the area in the crater zone will be free to corrode. At the next instant, the bulk of the corroded areas will most likely be eroded while the adjacent surface produced by the removal of material in the previous impact will be undergoing rapid corrosion being in the transient state. In other words, the smaller the erodent concentration, the larger is the volume of corrosion products.

When erodent concentration is very low, the additional effects associated with the collision between incoming and reflected particles and corrosion will be fairly small. Therefore, it is expected that there would be a critical value of the erodent concentration below which erosive mass loss rate will not be significantly affected by it.

Morphological features of eroded-corroded surfaces

Figure 12 shows the details of the eroded surface of 304 stainless steel, both for the room temperature and elevated temperature conditions. Similar micrographs for other stainless steels were reported earlier [9]. Some fine differences in the microfeatures which reflect the effect of temperature and corrosion on erosion features are worth pointing out. As compared to room temperature, the domains produced by impacting particles on the surfaces of elevated temperature specimens are larger. The "rub" bands which were produced due to the sliding action of erodent particles are also wider at elevated temperature. There is a clear indication that the erosion process at elevated temperature involved considerable plastic deformation of the surface. Due to the repetitive impact of particles resulting in the intermittent damage and replenishment of oxide scales, the latter are very thin and the oxide crystallites are fairly small, as inferred from Figure 2 (b). Figure 12 (c) shows the features on the eroded-corroded surface of the same stainless steel impacted with 400 grit particles at 650 ^{o}C. The deformation features are similar but finer because of the finer size of particles.

The cross-sectional view through the crater of 430 SS formed by the erosion-corrosion process at the temperature of 500^{o}C is given in Figure 13. It exhibits the damage by the incoming particles impinging at 30^{o} to the surface as well as the outgoing particles leaving at about the same angle. Specifically, it shows that the high-velocity stream of erodent particles cuts through the base material separating the fragments of material on its way. As the particles are reflected back, they tend to tear the overhead material as shown. It could finally result in the detachment of a fairly large fragment of material. There is some evidence of flake formation on the

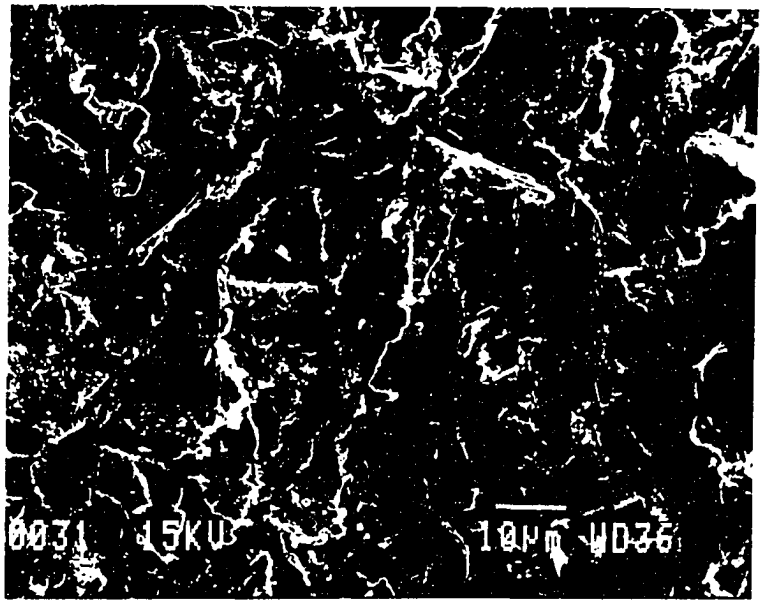

a

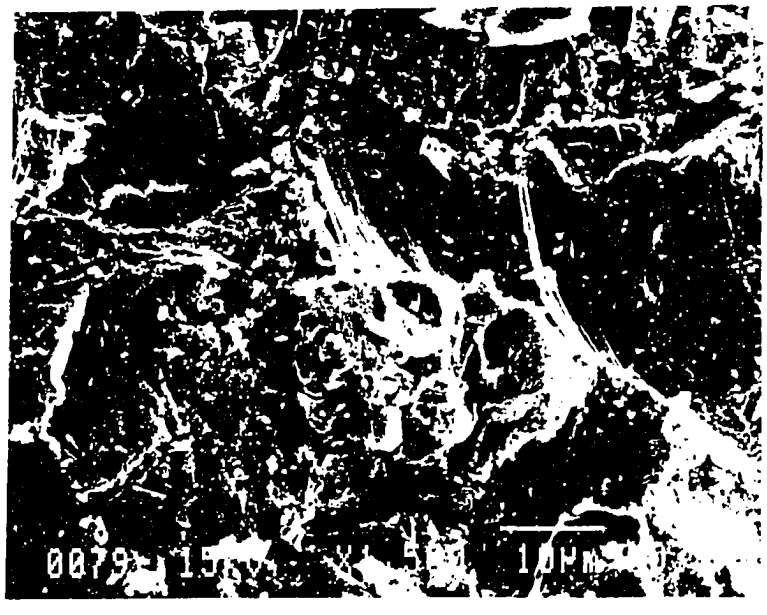

b

Figure 12: Electron micrographs of the craters of 304 SS: (a) 24°C, (b) 800°C, 120 grit SiC particles, erodent concentration 0.0421 g/mm^{2}s; (c) 650°C, 400 grit SiC particles, erodent concentration 0.0026 g/mm^{2}s

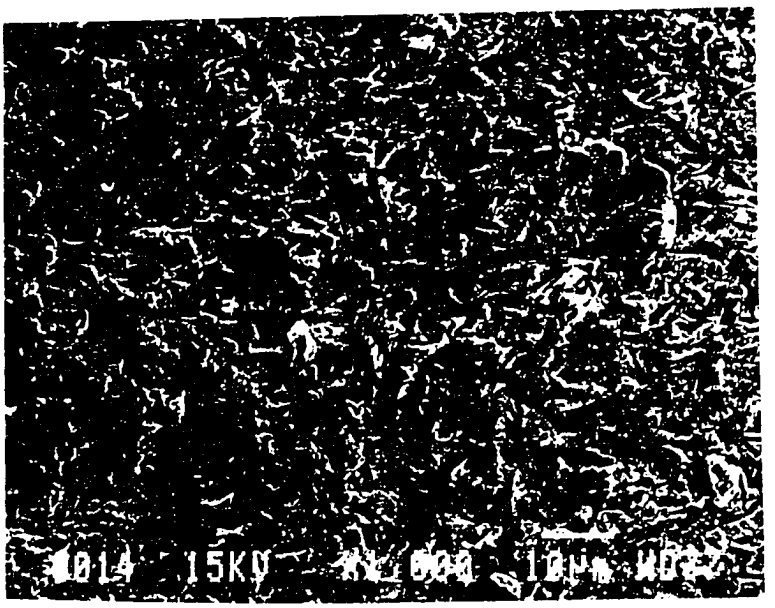

C

Figure 12 (Continued)

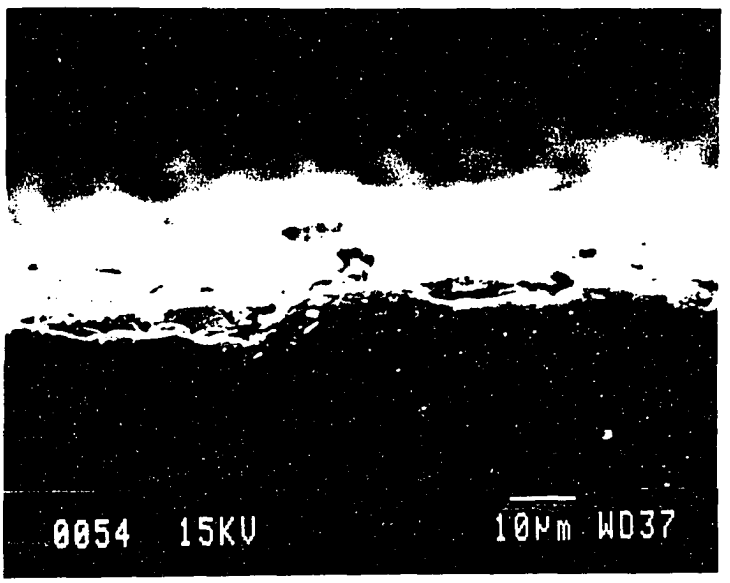

Figure 13: Cross-sectional view through the middle of crater of 430 SS eroded-corroded at 500°C

surface as well.

Figure 14 shows the slip bands produced in the substrate of the erosion crater of 304 SS where the particles were impacted at room temperature. It is noted that the slip bands are developed up to a depth of 20 μm. This indicates that a depth of 20 μm is affected below the impact location. There is obviously a deformation gradient with the deformation being maximum at the surface. Considering the impact of particles with a velocity of 70 m/s at an angle of 30° to the surface, it provides a strain rate of 3.0×10^6 /s.

Figure 15 shows how the deformation of grain boundaries occurs close to the surface of 304 SS as a result of the particle impacts at 800°C. The slip bands are not seen here because they were annealed out very quickly at the elevated temperature used in the test.

Interaction between Erosion and Corrosion

As the direct target of impacting particles, oxide scales play an extremely important role in elevated temperature erosion-corrosion. The role of oxidation in the erosion-corrosion of stainless steels cannot be simply treated in terms of mass gain, as some workers have suggested, since the mass gain due to oxidation is not significant for stainless steels, as shown earlier. It should instead be looked at in terms of the interactions between the oxide scales and impacting particles as well as the properties of oxide scales such as their adherence to the substrate, structure and mechanical properties.

Basically, there are four possibilities in which oxide scales may be damaged and/or removed. These are shown schematically in Figure 16. In type 1 a part

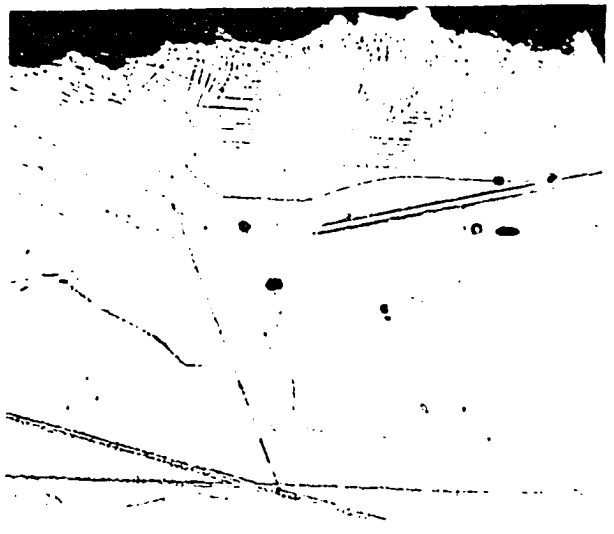

Figure 14: Slip bands on 304 SS due to particle impacts at room temperature.

Figure 15: Plastic deformation of grain boundaries of 304 SS due to particle impacts at 800°C

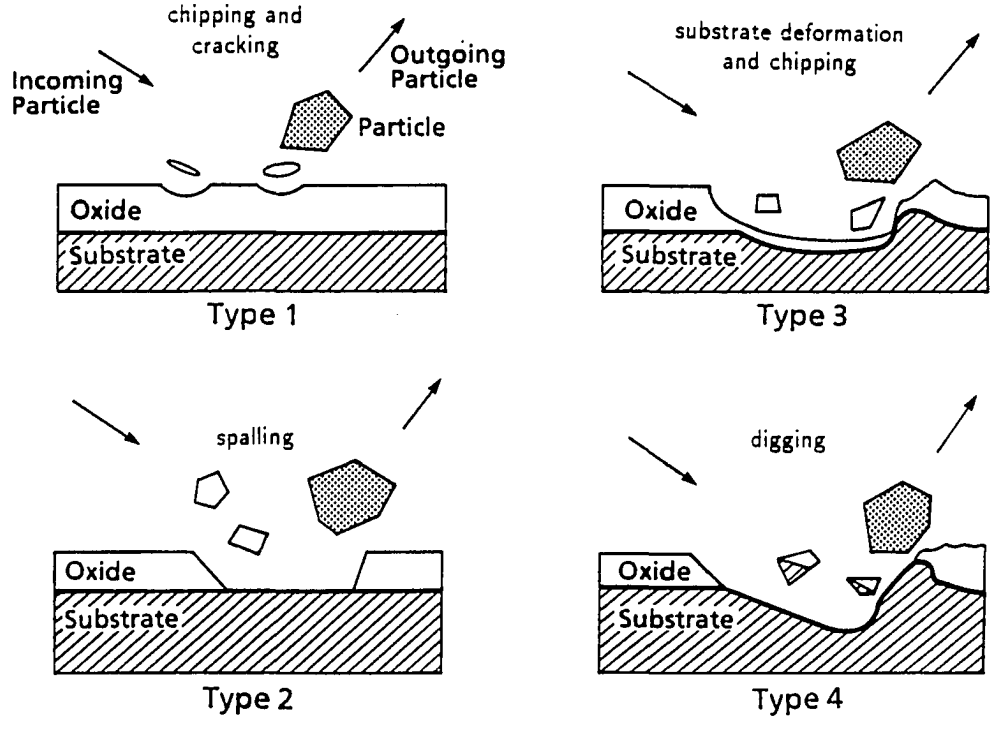

Figure 16: Schematic representation of the various possibilities of oxide scale removal or damage

of the oxide layer is chipped away by the impacting particles. The oxide scale get thinned locally, and some cracking might be induced in the scale. The events of this kind most likely occur in low-energy or low-erosivity (such as by round particles) impact situations. Type 2 is the case where the scale is completely knocked off the substrate (spalling) so that the bare material is exposed and the adherence of scale to the substrate is poor. This case would barely apply to stainless steels. When the adherence of oxide scale to the substrate is excellent and the oxide is pliable, the scale undergoes plastic deformation along with its substrate upon impact, and is consolidated or buckled with localized thinning due to scale chipping, as shown in type 3. There is some likelihood of cracking here due to good adhesion between the scale and its substrate and the localized severe plastic flow of substrate. Type 4 situation occurs where the oxide scale is removed along with some substrate material, as would be the case in high-energy or high-erosivity (such as by angular particles) impacts.

Some high magnification micrographs of the eroded craters for elevated temperature situation were taken so as to study the interaction between erosion and corrosion. Figure 17 (a) exhibits the features in the halo zone on the surface of 430 SS eroded at 800°C. Here the surface has undergone some plastic deformation. It is covered with oxide scales which are cracked in some locations but still seem to provide protection to the material underneath. In the location of erosion pits, the scales are consolidated and plastically deformed along with the substrate. This is the type 1 and 3 cases in Figure 16.

Figure 17 (b) shows an erosion pit on the surface of 304 SS eroded at 800°C. Here the oxide scales have been pushed to the sides. The substrate in the bottom of

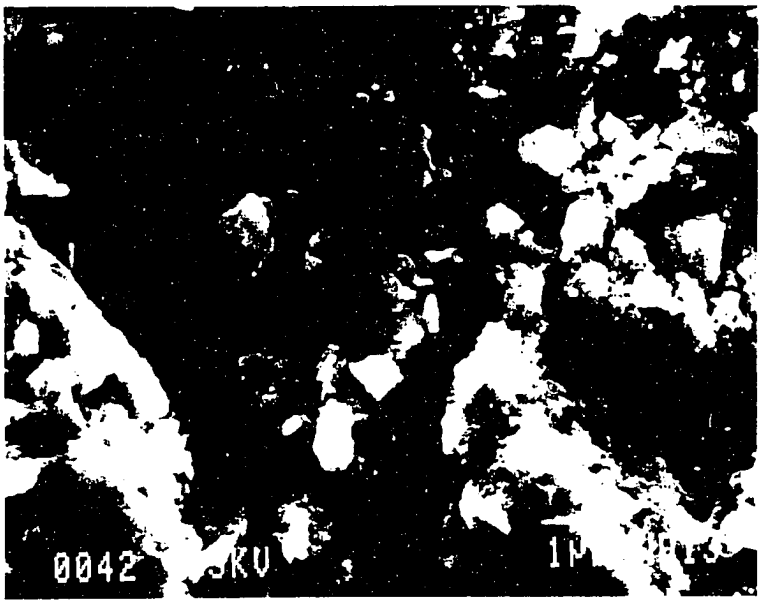

a

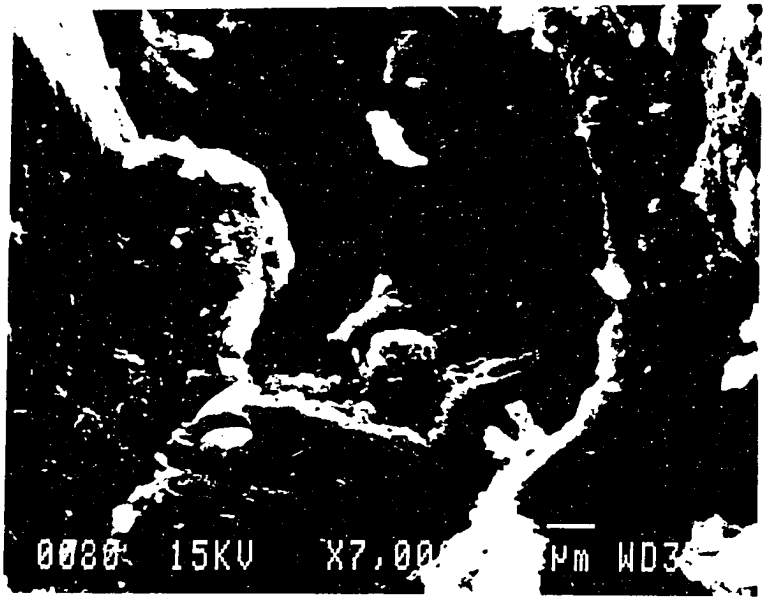

b

Figure 17: Electron micrographs of the surfaces eroded-corroded at 800°C (a) 430 SS [9], (b) and (c) 304 SS

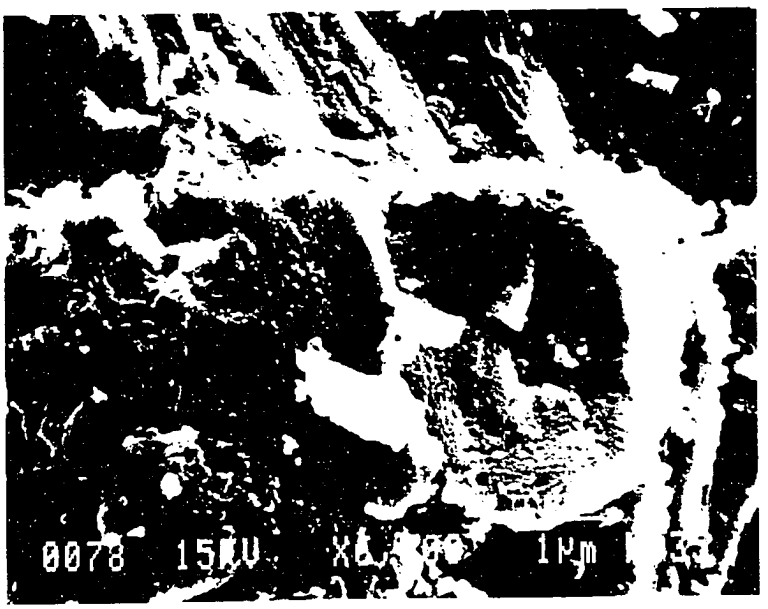

c

Figure 17 (Continued)

the pit is covered with thin oxide scales which seem to have buckled in some places. A lot of tiny erosion pits may be seen in the left side of the micrograph. These are produced either by fine particles or by the scattered particles resulting from the collision between incoming and outgoing particles. The features in this erosion pit are typical of type 3.

Figure 17 (c) provides the details of the central part of Figure 12 (b) which relates to the erosion-corrosion of 304 SS at 800°C. It shows extensive deformation, "rub" bands and oxidation of surface all over. There is also the evidence of condensed oxide scales by impacting particles.

Similar observations in the case of elevated temperature erosion-corrosion have been made by other workers as well. Working with six different kinds of chromium-containing steels, including 304, 310 and 410 SS, Levy and Wang [12] found that at shallow impingement angles and low particle velocities the oxide scales were segmented and removed by the slow cracking and chipping mechanisms. At steeper impingement angles and higher particle velocities, the scales were consolidated and removed at a higher rate by the spalling mechanism. The mechanisms in the first case correspond to type 1 and those in the second are close to type 2 in Figure 16. These workers [28] also pointed out that the oxide scale formed on these steels was thin when angular particles were used, resulting in the base metal participating directly in the wastage mechanism. This is the type 4 situation.

Wright et al. [11] examined the oxide formed in the erosion-corrosion of FeCrAlY (25% Cr) at 760 °C (velocity 43 m/s; angle 90°). They found that cracking, apparently as a result of particle impacts, occurred predominantly along oxide crystallite boundaries, and that the locations where buckling of oxide occurred did not appear

to coincide with alloy grain boundaries. They inferred from their observation on this alloy and also on AISI 446 steel (24% Cr) that the direct removal of oxide by impacts was small, although the cracking of oxide could well occur. It appeared that the impact produced localized flow in the substrate and so buckling of the oxide. This may be considered as the type 3 case in Figure 16.

As shown earlier, the oxide scale formed on the surface of stainless steel at elevated temperatures is strong, pliable, continuous, and has good adherence to the substrate. It would thus be expected to provide some protection from erosion to the surface of the metal. In order to check this aspect, erosion test [9] on 430 SS at 800°C with nitrogen as the carrier gas was carried out. It gave a slight increase in erosion compared to that in the oxidizing fluid stream. Similar observations were reported by Shida et al. [29] who tested various stainless steels at 650°C in both the argon and air atmospheres. Their results are shown in Figure 18. There is a marked decrease in the erosion rate of all stainless steels in air compared to that in argon. Levy and Man [21] also indicated that the formation of continuous scales on metal (9Cr1Mo steel) surface and their subsequent erosion appeared to provide some protection for the base metal. These workers also concluded that the presence of Cr_2O_3 in the scales of austenitic steels helped to reduce scale formation and removal and also the resultant metal wastage [13].

It should be realized that the oxide scale may provide protection in both possible situations. In the first case, the interaction of scale with impacting particles is basically within the scale layer so that the damage to the substrate material is negligible. In the second case, some substrate material along with the oxide film is removed, but since the scale has desirable properties such as high strength and pliability, it reduces

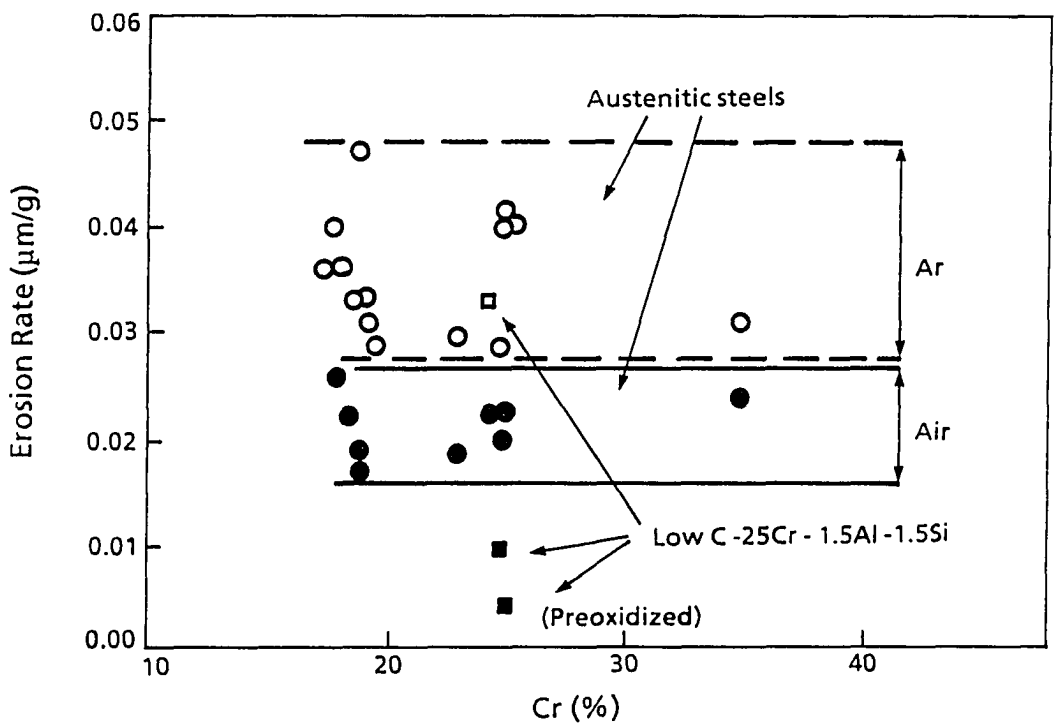

Figure 18: Results of erosion rate of various stainless steels tested in argon and air atmospheres at 650°C, 30° and 50 m/s by using the coal ash particles [29]

the substrate material loss due to its retardation effect on the efficiency of erosion impacts.

It may be added that even at elevated temperatures, where corrosion is dominant, the temperature-dependent properties of stainless steels play an important role. It is so because any deformation, stresses or cracks developed in the substrate will affect the oxide scale because of its strong adherence to the base metal.

CONCLUSIONS

1. The rate of oxidation is enhanced by the external mechanical damage of surface such as by erosion.

2. The dynamic impact and scratch tests revealed that the oxide scales formed on the surface of stainless steels by exposure to air at 800°C were strong and pliable and had excellent adherence to the substrate. Such oxide scales are expected to provide protection to the surface from erosion.

3. The variation of erosive mass loss rate with temperature is similar for all types of stainless steels. There is virtually no change in erosive mass loss rate from ambient to 200°C. It increases rapidly from 200 to 400°C. Above 400°C the rate of increase in erosive mass loss rate with increased temperature depends upon the erodent concentration.

4. The erosive mass loss rate is basically insensitive to erodent concentration at room temperature but is highly sensitive to it at elevated temperatures.

5. The variation of erosive mass loss rate with particle size at elevated temperature follows the same general trend as at room temperature.

6. When the particles of varying sizes are accelerated in a fluid stream at constant pressure, the erosive mass loss rate is higher for finer particles. It is so because the finer particles are accelerated at a higher velocity than the coarser particles.

7. The maximum in erosive mass loss rate for 304 SS occurs in the impingement angle range of 20° to 30° irrespective of temperature.

8. The erosive mass loss rate at elevated temperatures is less sensitive to impingement velocity than at room temperature.

9. The slip bands are formed in the substrate of 304 SS by particle impacts at room temperature.

10. As a result of the particle impacts at elevated temperatures, the grain boundaries in the substrate are severely deformed.

11. Erosion at elevated temperatures is greatly influenced by oxidation so that the interaction between erosion and oxide scales becomes an important consideration.

12. There are four possibilities suggested for the damage or loss of material by impacting particles. These are the chipping of oxide layer, the removal of oxide exposing bare metal, the plastic deformation of substrate and oxide scale resulting in the consolidation and buckling of the latter, and the removal of oxide scale along with some substrate material.

REFERENCES

[1] Fujikawa, H., H. Makiura, N. Fujino, J. Murayama, M. Yagi, and H. Yuzawa. "High Temperature Corrosion Behavior of Austenitic Stainless Steels for Utility Boilers." In High Temperature Corrosion, ed. Robert A. Rapp, 469-75. Houston: National Association of Corrosion Engineers, 1981.

[2] Satto, M. and H. Furuya. "Oxidation Behavior of Stainless Steel for Fast Breeder Reactor Fuel Cladding under Low Oxygen Pressure." High Temperature Corrosion of Metals and Alloys, Third JIM International Symposium Held in Japan 17-20 November 1982, 523-30. Japan: The Japan Institute of Metals, 1982.

[3] Kofstad, P. High Temperature Corrosion. New York: Elsevier Applied Science, 1988.

[4] Morrison, C. T., R. O. Scattergood, and J. L. Routbort. "Erosion of 304 Stainless Steel." Wear 111 (1986): 1-13.

[5] Gat, N. and W. Tabakoff. "Some Effects of Temperature on the Erosion of Metals." Wear 50 (1978): 85-94.

[6] Tabakoff, W., A. Hamed, and J. Ramachandran. "Study of Metals Erosion in High Temperature Coal Gas Streams." J. Engineering for Power 102 (1980): 148-52.

[7] Tabakoff, W. "Erosion Study of High Temperature Metals Used in Turbomachinery." In High Temperature Corrosion in Energy systems, ed. M. F. Rothman, 809-23. New York: Metallurgical Society of AIME, 1985.

[8] Levy, A., J. Yan, and J. Patterson. "Elevated Temperature Erosion of Steels." Wear 108 (1986): 43-60.

[9] Zhou, J. R. and S. Bahadur. "High-Temperature Erosion-Corrosion Behavior of Stainless Steels." In Corrosion and Particle Erosion at High Temperatures, 118th Annual Meeting of the TMS Held in Las Vegas, NV, 1989, edited by V. Srinivasan and K. Vedula, 315-33. Warrendale: TMS, 1989.

[10] Levy, A., E. Slamovich, and N. Jee. "Elevated Temperature Combined Erosion-Corrosion of Steels." Wear 110 (1986): 117-49.

[11] Wright, G., V. Nagarajan, and J. Stringer. "Observations on the Role of Oxide Scales in High-Temperature Erosion-Corrosion of Alloys." Oxidation of Metals 25 (3/4) (1986): 175-99.

[12] Levy, A. and B. Q. Wang. "Erosion-Corrosion of Steels in Simulated and Actual Fluidized Bed Combustor Environments." Wear 131 (1989): 85-103.

[13] Levy, A. and Y. F. Man, "Erosion-Corrosion Mechanisms and Rates in Fe-Cr Steels." Wear 131 (1989): 39-51.

[14] Yurek, G. J. "Mechanisms of Diffusion-Controlled High-Temperature Oxidation of Metals." In Corrosion Mechanisms, ed. F. Mansfeld, 397-446. New York: Marcel Dekker,Inc., 1987.

[15] Levy, A. and Y. F. Man. "Surface Degradation of Ductile Metals in Elevated Temperature Gas-Particle Streams." Wear 111 (1986): 173-86.

[16] Levy, A. "Mechanisms of Combined Erosion-Corrosion of Steels at Elevated Temperatures." In Corrosion and Particle Erosion at High Temperatures 118th Annual Meeting of TMS, Held in Las Vegas, NV, 1989, edited by V. Srinivasan and K. Vedula, 207-30. Warrendale: TMS, 1989.

[17] Levy, A. V. et al. "Contributions to US Department of Energy AR & TD Fossil Energy Materials Program" (Quarterly Progress Report, Oak Ridge National Laboratory, March 31, 1986).

[18] Sethi, V. K. et al. Proc. Conference on Erosion by Liquid and Solid Impact VI, paper no. 73, ed. J. E. Field. England: University of Cambridge, 1987.

[19] Tilly, G. P. "Erosion Caused by Impact of Solid Particles." In Treatise on Materials Science and Technology 13, ed. D. Scott, 287-319. New York: Academic Press, 1979.

[20] Zhou, J. R. and S. Bahadur. "Effect of Blending of Silicon Carbide Particles in Varying Sizes on the Erosion of Ti-6Al-4V." Wear 132 (1989): 235-46.

[21] Levy, A. and Y. F. Man. "Effect of Particle Variables on the Erosion-Corrosion of 9Cr1Mo Steel." Wear 131 (1989): 53-69.

[22] Tilley, G. P. "A Two Stage Mechanism of Ductile Erosion." Wear 23 (1973): 87-96.

[23] Sage, W. and G. P. Tilly, "The Significance of Particle Size in Sand Erosion of Small Gas Turbines." J. Roy. Aero. Soc. 73 (1969): 427-28.

[24] Ruff, A. W. and S. M. Wiederhorn, "Erosion by Solid Particle Impact." In Treatise on Materials Science and Technology 16, ed. C. M. Preece, 69-126. New York: Academic Press, 1979.

[25] Rurenne, S., M. Fiset, and J. Masounave, "The Effect of Sand Concentration on the Erosion of Materials by a Slurry Jet." Wear 133 (1989): 95-106.

[26] Kang, C. T., F. S. Pettit, and N. Birks, "Simultaneous Erosion and Oxidation of Nickel at High Temperatures," In Transport in Nonstoichiometric Compounds, ed. G. Simkovich and V. S. Stubican, 411-27. New York: Plenum Press, 1985.

[27] Bahadur, S. and R. Badruddin, "Erodent Particle Characterization and the Effect of Particle Size and Shape on Erosion." In Wear of Materials, International Conf. Held in Denver April 9-13, 1989, edited by K. C. Ludema, 143-53. New York: ASME, 1989.

[28] Levy, A. and B. Q. Wang, "The Effect of Test Conditions on the Erosion-Corrosion of Alternate Low Alloy Steel Tubing Alloys." Wear 131 (1989): 71-84.

[29] Shida, Y., N. Ohtsuka, and H. Fujikawa, "Influence of Particle Properties on the Solid Particle Erosion Behavior at High Temperature." High Temperature Corrosion in Energy Systems, ed. M. F. Rothman, 769-80. New York: Metallurgical Society of AIME, 1985.

PART III.

SEM STUDIES OF MATERIAL DAMAGE IN ALUMINA CERAMICS BY ANGULAR SINGLE AND MULTIPLE PARTICLE IMPACTS

ABSTRACT

The mechanisms of erosion in alumina ceramics have been investigated by scanning electron microscopy. The five commercial aluminas tested ranged from pure alumina to those containing different proportions of silicate glassy phase and zirconia. In single particle impact tests, the targets were impacted with 1035 μm angular SiC particles and in multiple particle tests with 151 μm SiC particles. The particles were always impacted under normal impact condition with an impingement velocity of 50 m/s. It was found that whereas brittle failure was the basic erosion mechanism, the morphological features of eroded surfaces were quite different for different materials and depended upon their compositions. The presence of secondary phases improved the bonding between alumina grains and also increased toughness by absorbing part of the impact energy. Therefore, the erosion resistance was enhanced by the presence of secondary phases in alumina. The erosion rates of these materials are analyzed briefly in terms of the erosion mechanisms. It was found that the classical lateral cracks which are typical of brittle indentation fracture were not present on the eroded surfaces of aluminas.

INTRODUCTION

In recent years, ceramics have found more and more applications because of some properties which are superior to those of other materials [1-3]. The main drawback of these materials is their inherent brittleness. When subjected to attack by hard particles as in erosion, their high brittleness makes them sensitive to surface cracking. This leads to surface degradation and material damage [4].

The mechanism of indentation fracture, produced by the impact of spherical particles, has provided fundamental theories for the erosion of ceramics. There are two commonly-accepted classifications of these theories: those based on a purely elastic fracture [5-8], and others based on an elastic-plastic fracture [5, 9-14]. These two theories are dependent upon the impacting particles size. The former theory holds good for particles whose radius at the point of impact is larger than a critical radius $R_c(> 200\mu m)$ and which produce Hertzian cone cracks. The latter theory is good for smaller particles which produce radial and lateral vent cracks. Whereas, in a purely elastic fracture the cooperative intersection of adjacent cone cracks is required for material removal, in an elastic-plastic fracture the material removal can occur by non-intersecting lateral cracks [5]. For the elastic-plastic fracture, two theories, namely, the quasi-static and the dynamic, have been developed. The major difference between these theories is that in the dynamic theory the calculation of the force from particle impact includes dynamic stress wave effects, while in the quasi-static theory the kinetic energy of particles is assumed to be absorbed completely by plastic flow.

The literature cites both the agreement and the discrepancy between the theoretical and experimental results [15-18]. In the erosion tests on glass by large spherical particles, several investigators found the direct evidence of material loss by the in-

tersection of Hertzian cone cracks [19-21], but some investigators could not see such cracks in their experiments [6-7]. In an erosion pit produced on alumina surface by 46 grit (508 μm diameter) SiC particles impacting at 75 m/s, both the cleavage and transgranular failures were noticed but no radial cracks were observed [22-23]. This is contrary to the indentation model in which both the radial and lateral cracks are expected to propagate out of the contact site. This kind of erosion pit was thought to be formed due to extensive grain-boundary cracking by the impact. Similar phenomenon was observed by Wiederhorn and Hockey [24] in the erosion of alumina [24]. On the other hand, Morrison et al. [25] characterized the single impact damage on mullite ($3Al_2O_3 \cdot 2SiO_2$) by Al_2O_3 particles of 270 μm diameter impacted at 100 m/s and 90°. Here, the damage zone consisted of the central impact crater from which radial cracks emanated and a lateral crack zone having approximately the dimensions of the impacting particle. They also made same observations with the erodent particles of 37 μm in size. Söderberg et al. [26] reported that the damage on 94% and 99% purity Al_2O_3 by single particle impacts at an impingement angle of 45° and a velocity of 66 m/s was mainly because of intercrystalline fracture. In some cases, transcrystalline fracture was also observed. In the case of 99.7% Al_2O_3, the impact point was found to be covered with a layer of erodent particle fragments. The erosion mechanism for all three ceramics was considered to be the same.

The erosion of Al_2O_3 seems to have some different characteristics from those of other brittle materials. It was found that the erosion damage in soda-lime glass could be modeled by indentation fracture mechanics, but the experimental results for sintered alumina could not be explained by the theory [17]. More work is, therefore, needed to develop the understanding of the erosion mechanisms for ceramics. The

present work is a continuation of our earlier work [15] on the commercial alumina ceramics. Its objective is to study the material surface damage by single and multiple impacts on alumina ceramics with emphasis on the differences because of the other phases present in the material.

EXPERIMENTAL DETAILS

The experimental conditions for both the single particle and multiple particle erosion tests were as follows:

Impingement velocity:	50 m/s
Impingement angle:	90°
Temperature:	24 °C
Erodent material:	SiC
Erodent particle size:	120 grit/151 μm (for multiple particle impacts)
	1035 $\pm$ 110μm (for single particle impacts)
Test duration:	70 minutes (for multiple particle impacts)
Erodent impacted:	250 g (for multiple particle impacts)
	one particle each impact (for single impacts)

A linear gas gun which was described in detail elsewhere [27] was used in single particle impact experiments. The single SiC particle of 1035 $\pm$ 110 μm was accelerated by high pressure air in a glass tube, 4 mm inside diameter and 1.2 m long. The specimen was mounted inside a test chamber and the distance between the specimen surface and the end of the acceleration tube was about 20 mm. The multiple particle erosion experiments were performed in a vertical sand-blast type of erosion test rig described earlier [28], and the experimental procedure is also described there.

The five commercial alumina ceramics which were used as the target materials are listed in Table 1. Their compositions, grain sizes and designations as also given in this table. Some of the relevant mechanical properties of these materials are given in

Table 1: Compositions and mean grain sizes of alumina ceramics

Manufacturer code[a]	Composition	Mean grain size (μm)	Designation used here
2140	90% alumina + 10% silicate glassy phase	7.6	Al10Si
6928	96% alumina + 4% silicate glassy phase	6.2	Al4Si
M-RCHP-4PD	99.5% alumina	8.0	Al
6935	zirconia-toughened alumina + 4% silicate glassy phase	6.0	ZTA4Si
ZTA-GF-A	zirconia-toughened alumina	6.0	ZTA

[a]Champion Spark Plug Company, Detroit, Michigan.

Table 2: Mechanical properties of alumina ceramics

	Al	ZTA	ZTA4Si	Al4Si	Al10Si
Hardness, VHN	1,710	1,610	1,260	1,660	1,250
Fracture toughness, MPa$\sqrt{m}$	4.0	5.5	5.5	4.1	3.9
Modulus of elasticity, MPa	344,740	289,580	289,580	303,370	268,900
Compressive strength, MPa	2,758	2,900	2,900	2,620	2,410

Table 2. All of these materials were ball-milled with water, spray dried, and pressed in a steel die at 82.5 MPa and sintered at 1550 °C for 2 hours.

The eroded surfaces were examined by scanning electron microscopy. The specimens were coated with gold and an accelerating voltage of 15 kV was used.

RESULTS AND DISCUSSION

Single Particle Impacts

Single particle impact experiments were performed by impacting 1035 μm angular SiC particle normal to the ceramic specimen surface at 50 m/s velocity. Figure 1 (a) shows the details in the impacted region of the single phase alumina (Al) target and Figure 1 (b) exhibits the central part of the impacted region at a higher magnification. It may be seen that the impact produced mostly intergranular cracking, while transgranular cracking also occurred in some places. There is no sign of plastic deformation. In some locations, cracks initiated and propagated partways so that the detachment of grains did not occur. In Figure 1 (a) some radial cracks emanating from the edge of the damaged site may be seen. Such cracks are typical in classical indentation fracture. In the upper right location of the impact site (marked by an arrow), a network of cracks has developed with the result that several fragments will be separated from this location on subsequent impacts.

When Al4Si was impacted by a single particle, profuse transgranular cracking occurred, as shown in Figure 2. In the lower right corner of Figure 2 (a), an erosion pit may be seen. It was created by the loss of material from this location. Around the pit edges, a lot of fragments which have been shaken loose from the target material are located. Figure 2 (b) is a higher magnification photograph of Figure 2 (a) and shows intensive transgranular cracking. As mentioned in the introduction section, one of the theories for the erosion of ceramics is based on indentation fracture produced by impacting spherical particles. It points out that pure elastic fracture generally occurs when the radius of contact on impact is larger than a critical radius ($> 200\mu m$). In

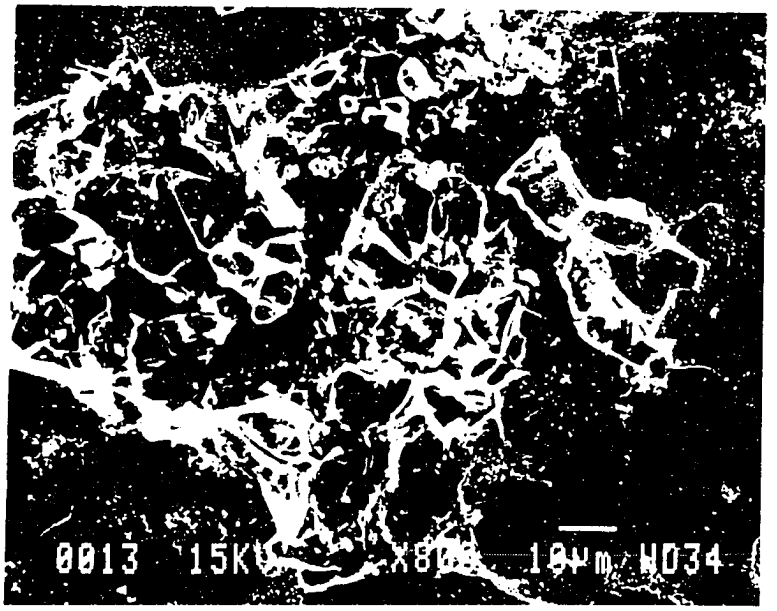

a

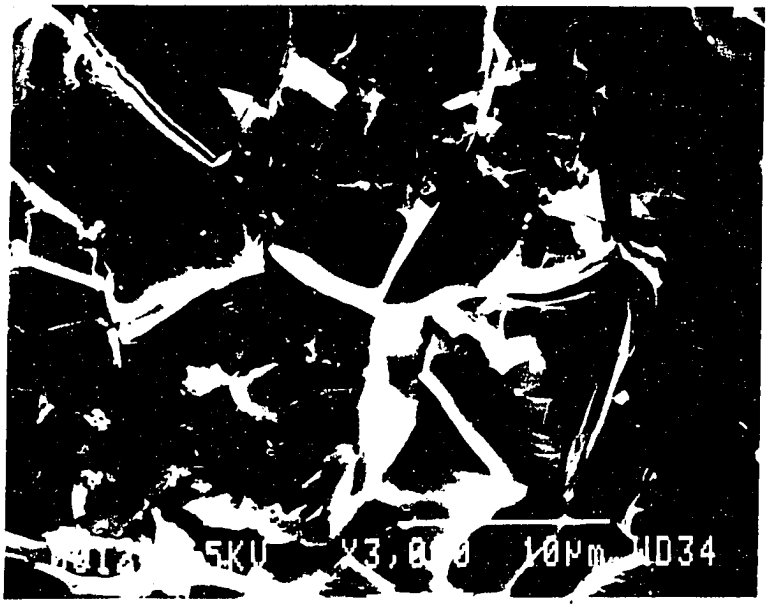

b

Figure 1: Erosion damage by the normal impact of a single angular particle on single phase alumina: particle size 1035 μm; impingement velocity 50 m/s

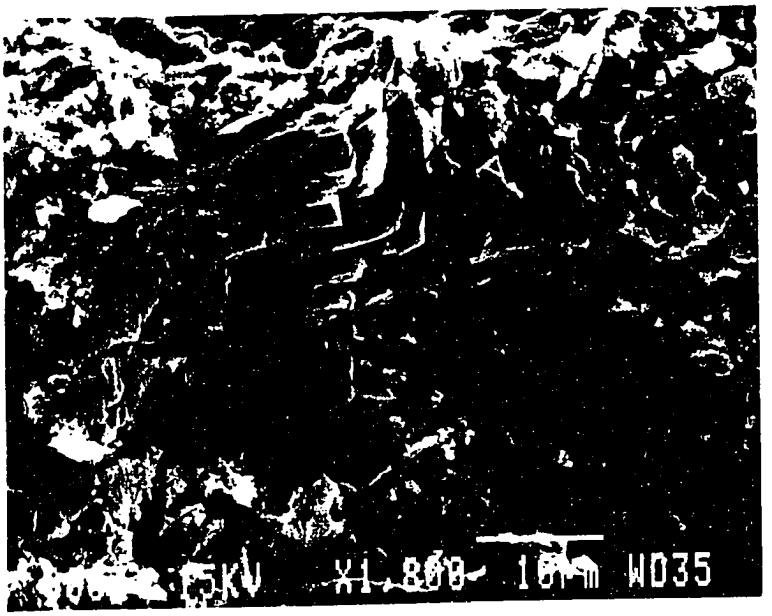

a

b

Figure 2: Morphology of erosion damage by a single particle impacted normally on Al4Si target

c

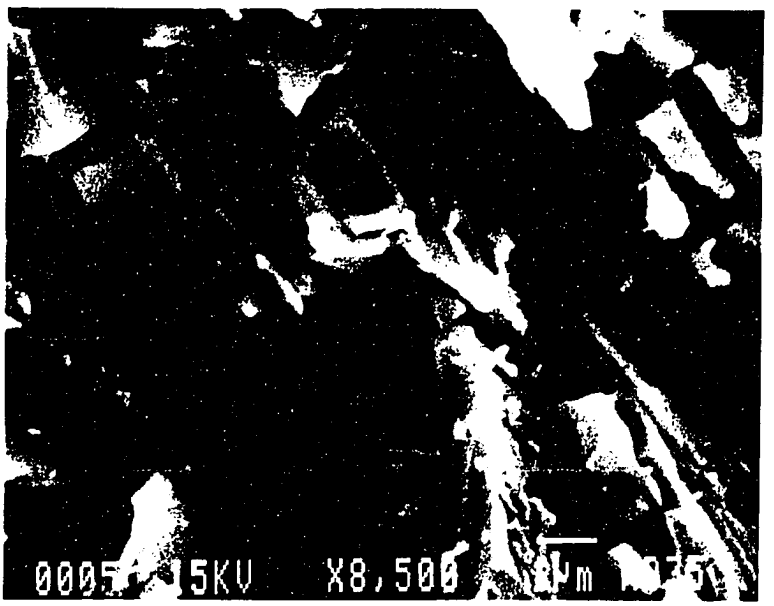

d

Figure 2 (Continued)

the present work, the impacted particles were angular as opposed to being spherical. The individual particle might impact the target surface either on a blunt side or on a sharp edge so that the radius of contact in these two cases would be different. This would also change the mechanism of erosion from elastic to elastic-plastic fracture. The erosion in Figure 2 (c) appears to be the case of pure elastic fracture where mostly transgranular cracks developed parallel to each other so that multiple laminar fragments were formed. Such cracking was caused by high-speed loading and because of the poor resistance of material to crack propagation. Figure 2 (d) shows at a higher magnification the fragmentation of material by parallel cracking.

The comparison between the morphological features in Figures 1 and 2 for the impact-damaged surfaces of single phase alumina (Al) and the alumina containing a secondary glassy phase (Al4Si) revealed the following differences. In the single phase alumina, the main mechanism of cracking was intergranular and the density of cracks was lower, so that the size of fragments removed was larger being about the size of the grains. Once these fragments were formed, they were completely removed so that a "clean" impact site was left. In contrast to this, the size of the fragments removed in the case of Al4Si was finer because of transgranular cracking and a higher crack density which resulted in subgrain size fragments. The impact site left here was not "clean" because numerous fragments remained loosely attached to the target surface. The differences were observed on many specimens and so are typical of the materials studied.

The above differences may be accounted for in terms of the microstructure and mechanical properties of these two aluminas. The higher the modulus of elasticity of a material, the higher is the contact stress induced in it on impact. Similarly, the

higher the hardness, the greater is the stress needed to initiate failure on indentation. Once a crack initiates, its propagation leading to fracture is governed by the fracture toughness of material. Since the modulus of elasticity of Al was higher than that of Al4Si (Table 2), the contact stress in this material was also higher. From the microstructural aspect, alumina grains were much stronger than their grain boundaries which were weakened by the presence of impurities, pores, and the mismatch of lattice, etc. Therefore, the impact in alumina produced a relatively higher stress field which initiated cracks in the weak grain boundary region. This process was aided also by the internal stresses in stressed grain boundaries due to the mismatch of lattice. The cracks propagated along the grain boundaries because the stressed volume at the impact site which was in unstable high energy state tried to revert to the stable low energy state by releasing energy and thereby inducing further stresses. Because of the lower resistance to crack propagation along grain boundaries, the cracks were able to develop fully and propagate to the surface, thereby releasing energy further. This energy served as a part of the driving force for further crack propagation. On the other hand, in the two phase Al4Si alumina, alumina grains were strongly bonded by a silicate glassy phase so that the grain boundaries were no longer vulnerable to either crack initiation or crack propagation. Here, cracks initiated at any site of stress concentration, such as a pore, a pre-existing fine crack, or an impurity location. For the same reasons as indicated above, the nucleation density of cracks was high so that the driving force for crack propagation was lower, and the individual cracks could not develop fully. The morphology of the eroded surface was dominated here by transgranular fracture because the grain boundaries were no longer weaker than the grains.

Figure 3 shows a set of micrographs of the surface of Al10Si impacted by a single particle under the same conditions as above. Figure 3 (a) shows an overall surface damage at low magnification. The actual impact site here was between the two arrows marked. There are radial cracks seen emanating out of this region. The stresses induced in the central part of the crater were so concentrated that cracks initiated and propagated everywhere regardless of the glassy phase, alumina grains and grain boundaries. The damage of material occurred here by both the intergranular and transgranular fracture processes. The top and the bottom parts of the pit in Figure 3 (a) are less severely damaged than the central part. The features in the top part, which are quite different from those in the central part, are shown in Figure 3 (b). The material removal from the grains occurred here by transgranular processes in the locations indicated by arrows. Here the cracks were fully developed within a very shallow layer, and the fragments were completely removed. Figure 3 (c) shows the severely damaged area of another pit. There is an indication of plastic deformation occurring here in the glassy phase which is seen much better in Figure 3 (d). The features in Figure 3 (d) are quite different from those observed in the cases of Al and Al4Si. Most of the area in this micrograph seems to be covered by a deformed glassy phase. The presence of a substantial amount of glassy phase in Al10Si degraded its strength because the glassy phase is a weaker material. The cracking would thus occur predominantly within the glassy phase. Based on these observations, it can be seen that the features on the eroded surface of Al10Si are a combination of the brittle fracture of alumina grains and the deformed structure of glassy phase.

When zirconia-toughened alumina was subjected to a single particle impact, it underwent localized plastic deformation presumably in the zirconia region. This is

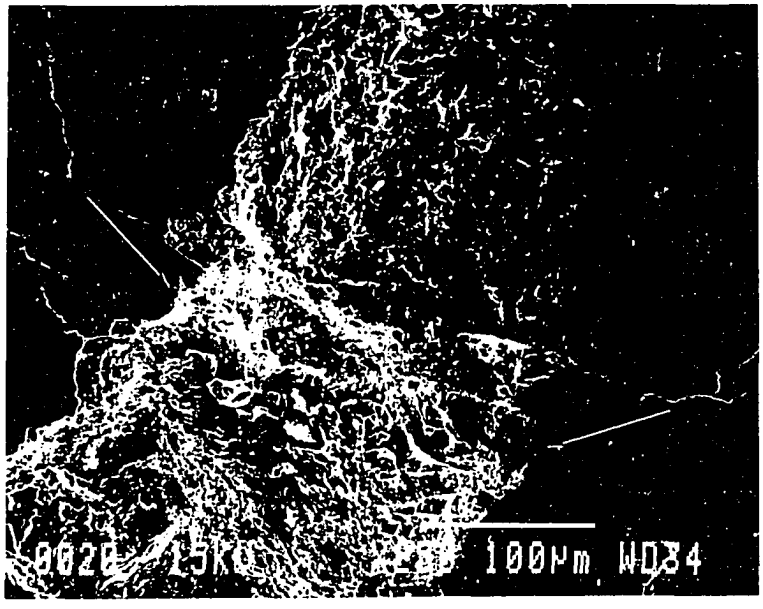

a

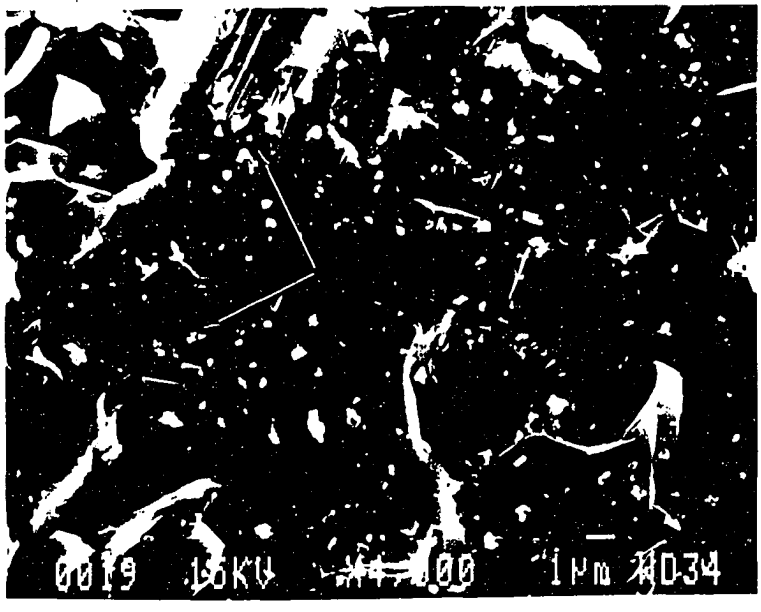

b

Figure 3: Morphology of erosion damage by a single particle normal impact on Al10Si

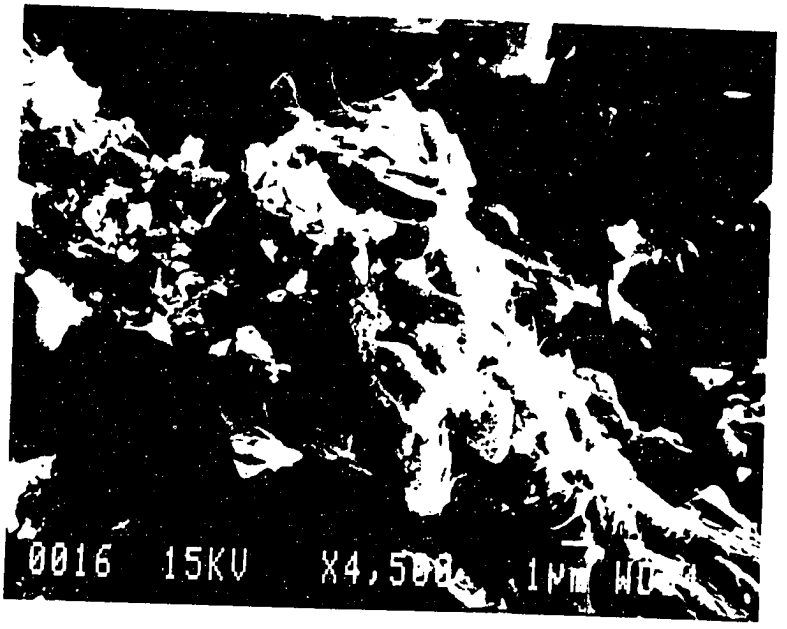

c

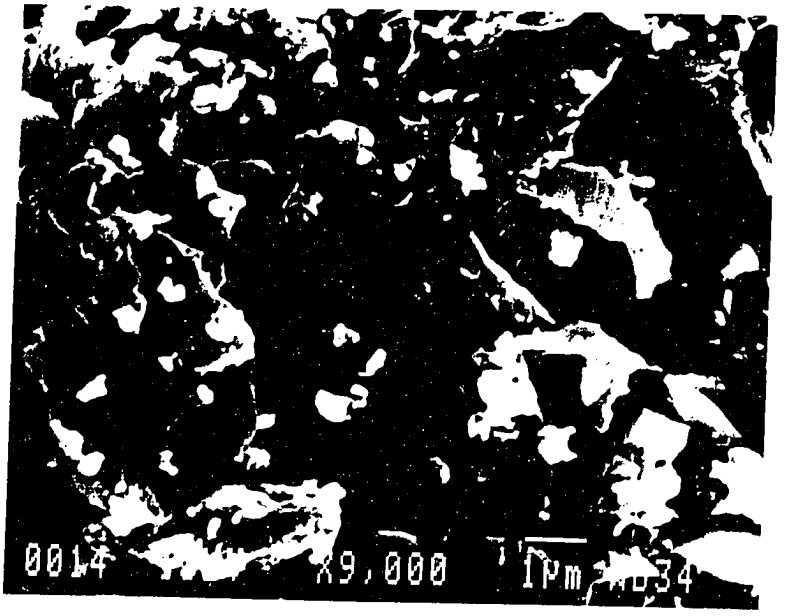

d

Figure 3 (Continued)

seen in many locations in Figure 4 (a). For example, the location marked by arrow 1 shows a plowing groove and that marked by arrow 2 shows deformed lips or stringers with rounded shape. In addition, there is an evidence of typical brittle fracture, as seen in Figures 4 (b). Figure 4 (c) shows the central part of Figure 4 (b) at higher magnification. It presents the typical intergranular fracture appearance as seen for single phase alumina. This feature is also indicated by the arrow 3 in Figure 4 (a).

Multiple Particle Impacts

Figure 5 shows the typical surface features of single phase alumina (Al) eroded by 120 grit SiC particles at 50 m/s velocity and normal impingement angle. There are many small "flat" zones seen in Figure 5 (a). These can be seen more clearly at a higher magnification in Figure 5 (b). These zones were presumably produced by the impact of low erosivity particles which had either relatively low velocity or small size (as there is a statistical distribution of velocities and sizes involved in a travelling stream of particles) or by the contact of impacting particles with the target surface on their blunt sides. Due to the low erosivity of these particles and the high hardness of alumina, such particles were not able to inflict severe damage. They could neither effectively chip the target material nor produce concentrated stresses high enough to initiate and propagate surface cracks. The damage was thus possibly limited to being superficial. The worn zone, as marked by an arrow in Figure 5 (b), indicates brittle damage which is characterized by the cracks and the brittle wavy appearance. Such flat zones were observed on the eroded surfaces of other alumina materials as well. Figure 5 (c) shows both intergranular and transgranular cracking in the eroded

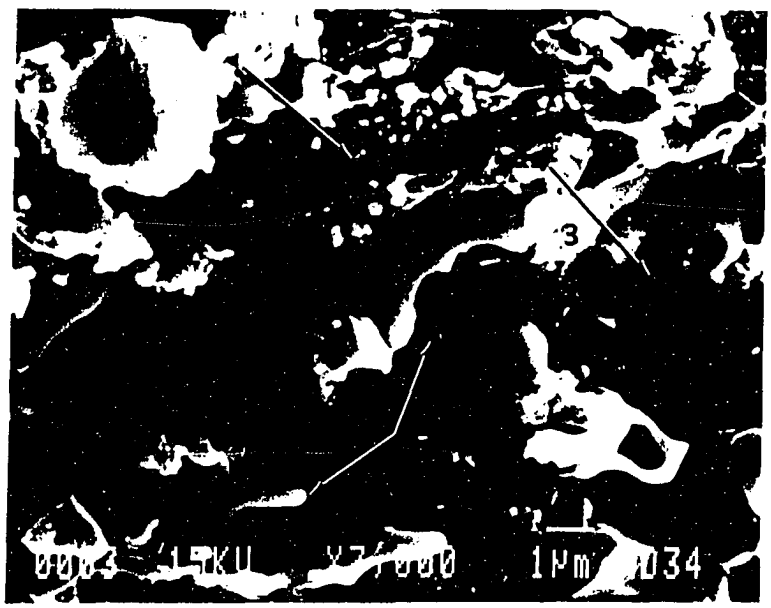

a

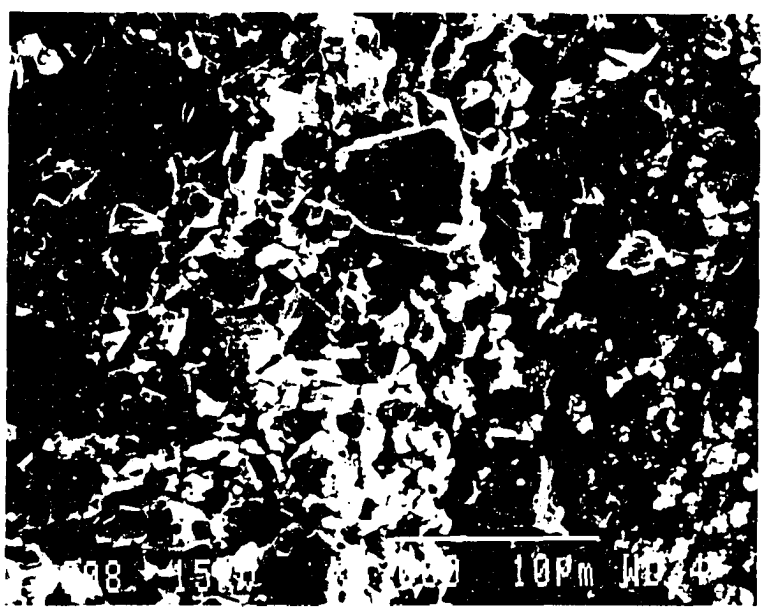

b

Figure 4: Morphology of erosion damage by a single particle impact on ZTA surface

c

Figure 4 (Continued)

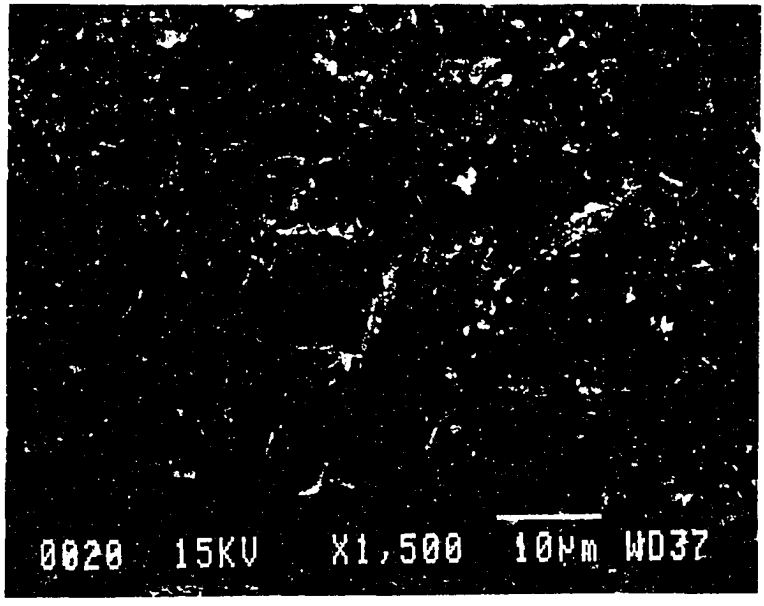

a

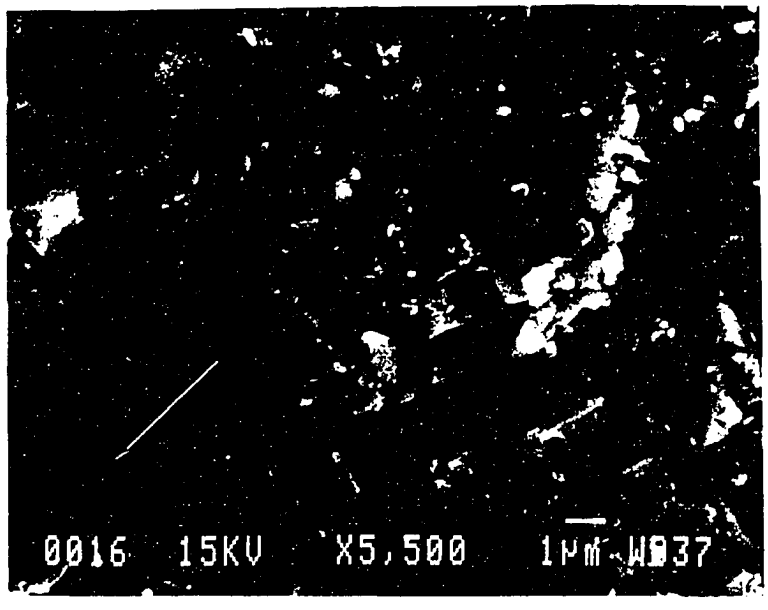

b

Figure 5: Surface morphology of single phase alumina Al eroded at normal angle and 50 m/s impingement velocity

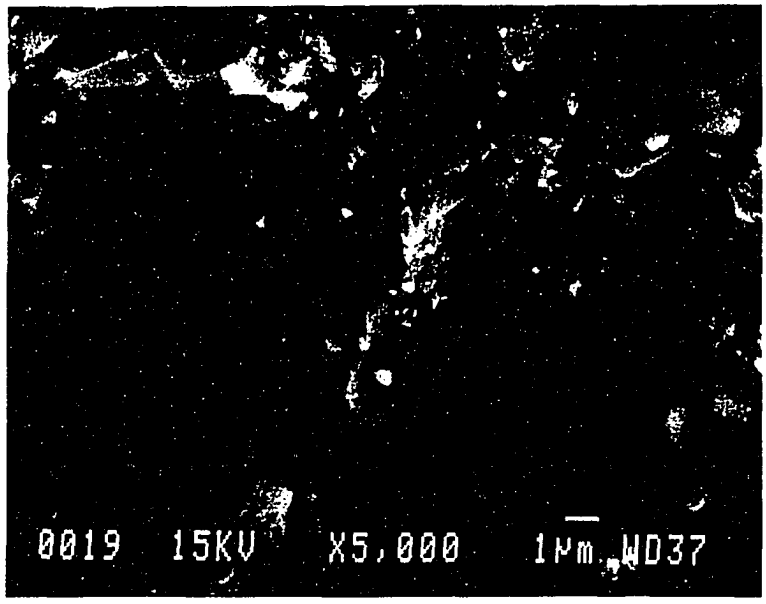

c

Figure 5 (Continued)

region.

Figure 6 shows the surface features of Al4Si eroded under the same conditions as above. The microfeatures in Figure 6 (a) are essentially identical to those in Figure 5 (a), characterized by small flat zones. The center of the crater in Figure 6 (b) is clean and presents the appearance of the grains having been pulled out of this region. The erosion morphology is typical of brittle failure where the fracture occurred along grain boundaries. Similar characteristics appear even in Figure 6 (c) which shows the halo zone of the erosion crater. The erosion damaged zone is jagged and faceted, which is characteristic of brittle fracture.

The eroded surface features of Al10Si are similar to those of Al4Si discussed above. These are shown in Figure 7 in which a big pit produced by erosion is seen. Obviously, this pit was created by the loss of several alumina grains. This happened because of the relatively lower strength, toughness and hardness of the material compared to those of other aluminas.

The eroded surface of zirconia-toughened alumina, shown in Figure 8 (a), appears to have the same features as discussed above for Al and Al4Si, but the surface exhibits some plastic deformation. This is seen better in Figure 8 (b) which should be compared with Figure 6 (b) for Al4Si to judge the difference in the extent of plastic deformation. On the eroded surface of ZTA, one can see brittle fracture as well as severely deformed zones, where the latter were most likely formed by the deformation of zirconia particles. In the presence of zirconia, alumina particles will be protected somewhat from severe damage because the impact energy will be partially absorbed by the zirconia particles undergoing deformation. Thus, there will be less energy available to cause damage in the brittle alumina grains.

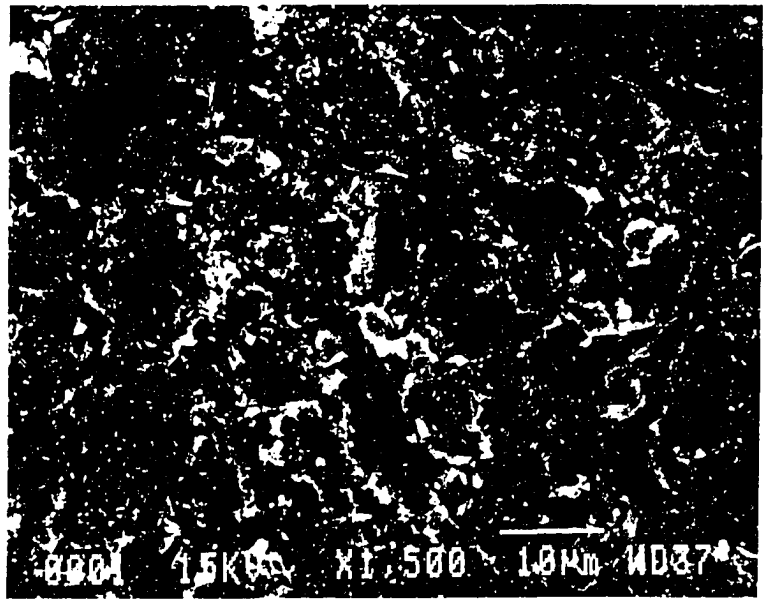

a

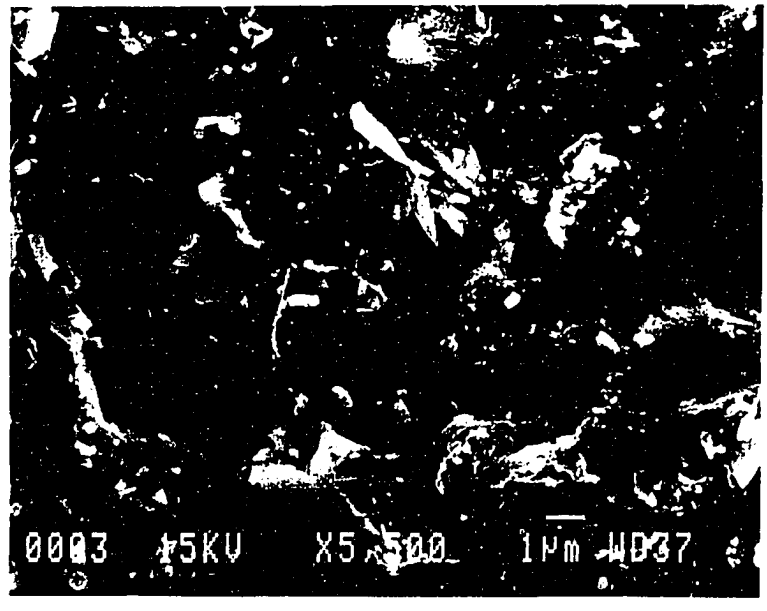

b

Figure 6: Surface features of Al4Si eroded at normal angle and 50 m/s impingement velocity: (a) and (b) center of crater; (c) halo zone of crater

c

Figure 6 (Continued)

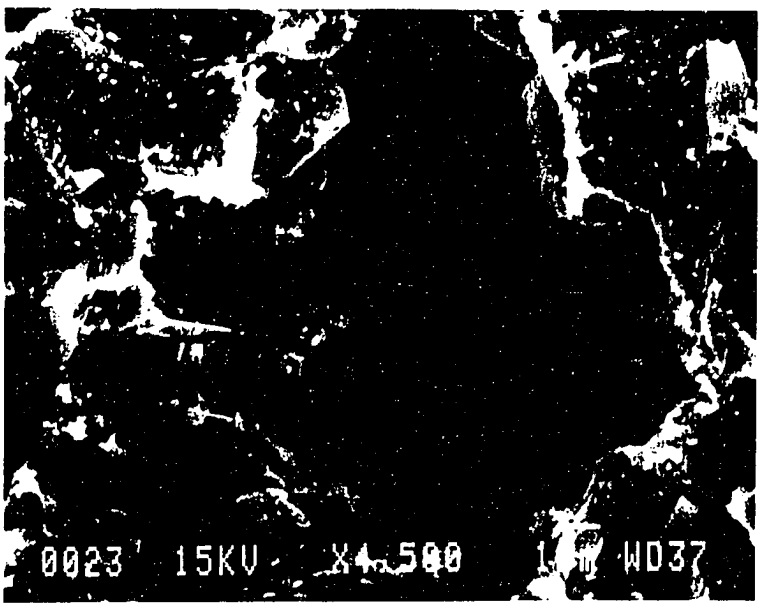

Figure 7: SEM micrograph of the eroded surface of Al10Si: 90° impingement angle, 50 m/s impact velocity

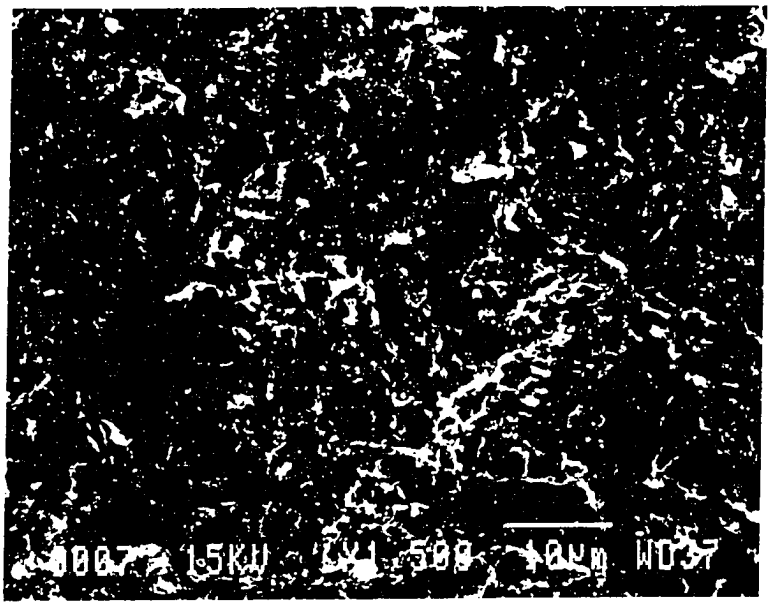

a

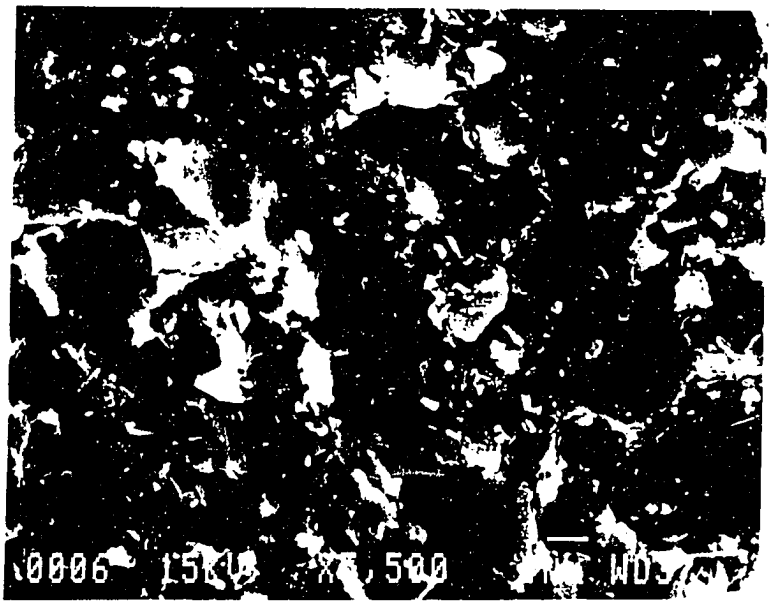

b

Figure 8: Eroded surface features of zirconia-toughened alumina: 90° impact angle, 50 m/s velocity

Figure 9 (a) shows the features in the halo zone of the erosion crater of ZTA. There are a number of hemispherical pits seen all over the surface. The details of the features inside the pit are shown at a higher magnification in Figure 9 (b). The average size of these pits was about 45 μm. Since the grain size of the material was about 6 μm, it implies that a number of grains were removed in the formation of this hemispherical pit. According to the elastic-plastic fracture theory, material removal from an impact location occurs by lateral cracks which are nucleated at the erodent-target contact site. These cracks propagate and terminate at the target surface. This enables the material within the damage zone to be separated from the substrate or be loosely attached to it. This material removal process can occur independently, without the need of the intersection of adjacent lateral cracks. It is believed that the hemispherical pits here were produced by a similar process. Furthermore, the development of these pits involved the impacts of high-erosivity particles (those with high velocity, large size, or contacting target surface at their sharp corners) which either travelled in the outer region of the particle stream or diverged from the main stream by collision with reflected particles. As may be seen from the erosion crater profile, the impact here was not at exactly 90°. The erosion pits were seen in the halo zone of erosion crater only. It is possible that such pits were produced all over the eroded surface but are not seen in the crater center region because these get obliterated by the severe damage caused by a succession of impacts in this region. Such pits were also observed in the halo zones of other kinds of aluminas.

It should be noted that these pits are not necessarily created by a single impact. The impact may nucleate an annular or lateral crack which may propagate but not necessarily to the target surface. Subsequent impacts would then be needed to com-

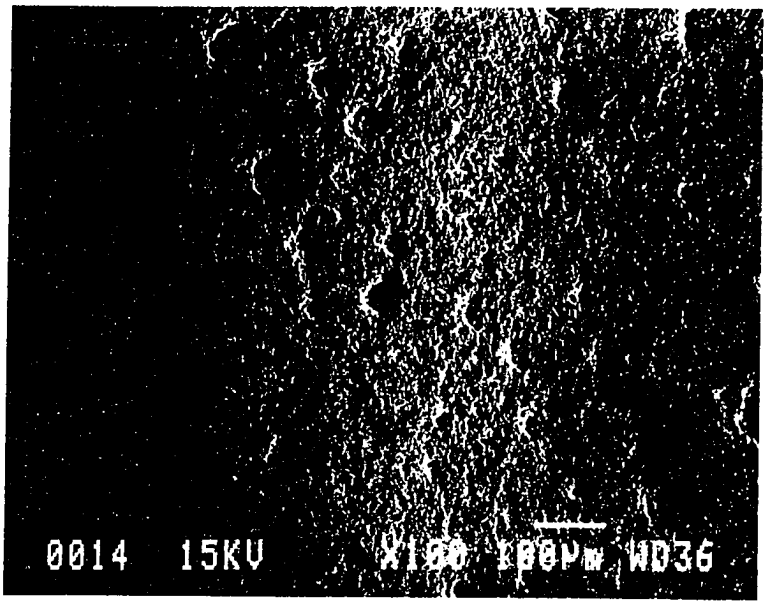

a

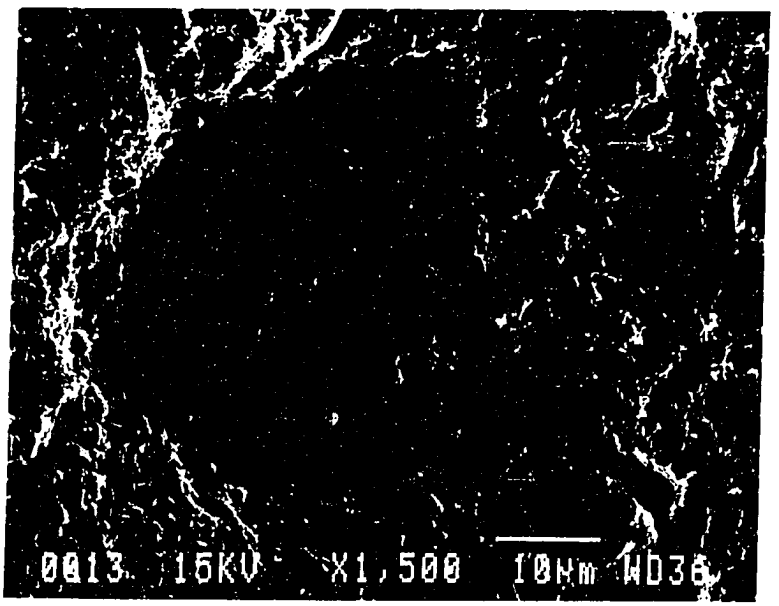

b

Figure 9: Hemispherical erosion pits in the halo zone of the erosion crater of ZTA

pletely remove material by further propagating the cracks to the outside surface. It is also possible that most particles might not even initiate annular or lateral cracks upon impacting the target surface because the contact stresses induced in the impact location might not be sufficiently high enough to initiate the indentation fracture.

Erosion Behavior

The above observations on the mechanisms of material removal support the erosion behavior of alumina ceramics in multiple particle impacts. Figure 10 gives the erosion rates of alumina ceramics for an impingement velocity of 50 m/s and an angle of 90°. It may be seen that single-phase alumina had the highest erosion rate and the erosion resistance was enhanced by the presence of secondary phases, such as silicate glassy phase and zirconia. It seems that an optimum quantity of the secondary phase is beneficial for erosion resistance because with further increase in it the degradation in erosion resistance occurred. The erosion behavior depicted in Figure 10 is related to the fracture mechanisms involved in the erosion of these aluminas. In single-phase alumina, grain boundaries were weak and so served as the sites for crack initiation and further provided easypaths for crack propagation. The cracks thus developed along grain boundaries and the complete grains were removed in erosion thereby resulting in a big loss of material. With the addition of an optimum amount of silicate glassy phase or zirconia, the bonding between the grains improved so that the impact energy was transferred to neighboring grains and a part of the impact energy was absorbed by secondary phases. Now the grain boundaries no longer served as the favorite locations for crack nucleation so that transgranular cracking occurred. This resulted in chipping and the fragmentation

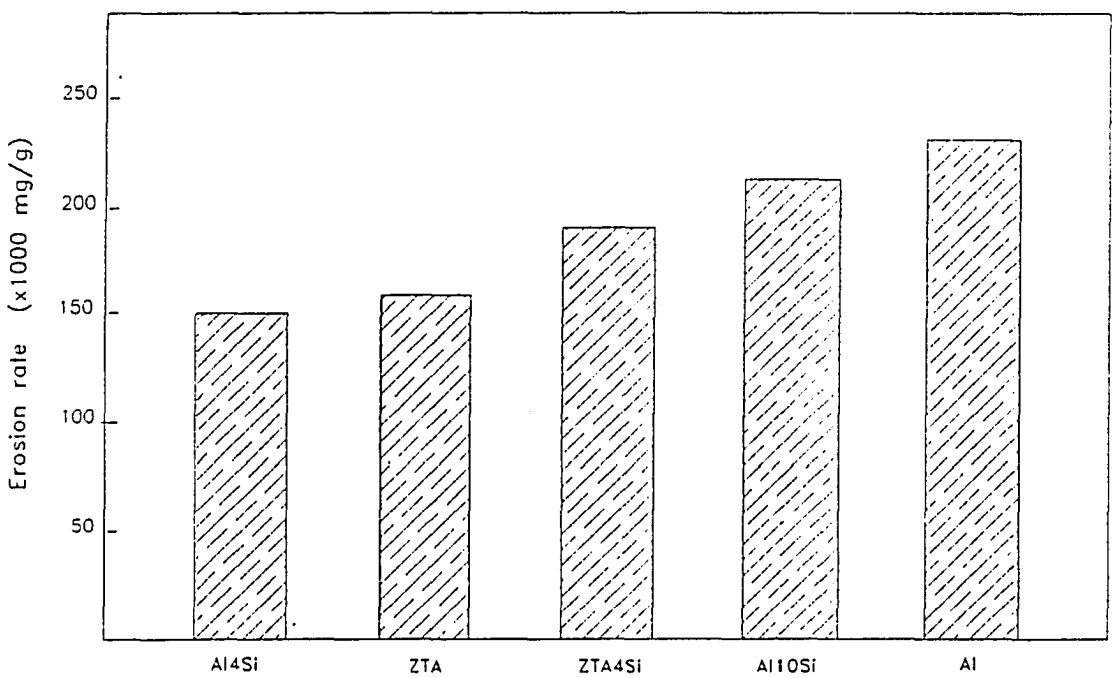

Figure 10: Erosion rate of aluminas at normal impact: velocity 50 m/s, 120 grit SiC particles

of grains. The cracks formed were not able now to develop fully. There was also plastic deformation of ZTA grains. Because of these phenomena, the erosion rate of the aluminas with secondary phases was lower than that of the single phase alumina. When the secondary phases were increased beyond their optimum values, degradation in the mechanical properties of aluminas occurred so that the materials became more vulnerable to erosive damage.

CONCLUSIONS

From the single particle and multiple particle impact studies on different kinds of aluminas, the following conclusions were drawn:

A. Single particle impacts

(1) Intergranular failure was the dominant mode of material removal in single phase alumina. Here the cracks were fully developed, the crack density was low, and the removal of fragments was complete.

(2) In the case of alumina containing 4% silicate glassy phase, the material removal occurred by transgranular cracking. The crack density here was higher than for single phase alumina. While some fragments were removed, others remained attached loosely to the crater surface.

(3) With the increase in glassy phase from 4 to 10% in alumina, the erosion features represented a combination of the brittle fracture of alumina grains and the plastic deformation of the glassy phase.

(4) The zirconia particles in ZTA were deformed plastically but some intergranular cracking still occurred.

B. Multiple particle impacts

(5) Brittle failure was the predominant mechanism in the erosion of all alumina ceramics. There were differences in the morphological features because of the differences in the compositions and the microstructures of these materials.

(6) The "flat" zones and the hemispherical erosion pits were the two characteristic features observed in all materials. The flat zones were formed because of material deformation under the low-erosivity impact condition while the hemispherical pits were produced by severe damage.

(7) The classical lateral cracks which are typical of brittle indentation fracture were not observed on the eroded surfaces of materials. Instead, the erosion features indicated that the mechanisms responsible for material removal were chipping, plowing, condensing, and localized cracking.

(8) There was localized plastic deformation observed in zirconia-toughened alumina.

(9) The presence of secondary phases, such as silicate glassy phase and zirconia, increased the erosion resistance of alumina ceramics.

REFERENCES

[1] Butler, E. G. "Engineering Ceramics: Applications and Testing Requirements." In Mechanical Testing of Engineering Ceramics at High Temperatures, ed. B. F. Dyson, R. D. Lohr, and R. Morrell, 1-10. New York: Elsevier Applied Science, 1989.

[2] Kato, K. "Tribology of Ceramics." Wear 136 (1990): 117-33.

[3] Bhushan, B. and L. B. Sibley. "Silicon Nitride Rolling Bearing for Extreme Operating Conditions." ASLE Transactions 25 (4) (1981): 417-28.

[4] Wiederhorn, S. M. and B. R. Lawn. "Strength Degradation of Glass Impacted with Sharp Particles - I Annealed Surfaces." Journal of American Ceramic Society 62 (1979): 66-70.

[5] Conrad, H. "Erosion of Ceramics." In Corrosion Erosion Wear of Materials at Elevated Temperatures, ed. A. V. Levy, 77-94. Houston: NACE, 1987.

[6] Sheldon, G. L., "Similarities and Differences in the Erosion Behavior of Materials." Journal of Basic Engineering 92 (1970): 619-26.

[7] Sheldon, G. L. and I. Finnie. "On the Ductile Behavior of Nominally Brittle Materials During Erosive Cutting." Journal of Engineering for Industry 88 (1966): 387-92.

[8] Mehrotra, P. K., G. A. Sargen,t and H. Conrad. "A Model for the Multiparticle Erosion of Brittle Solids by Spherical Particles." In Corrosion-Erosion Behavior of Materials, ed. K. Natesan, 127-45. Warrendale: The Metallurgical Society of AIME, (1980).

[9] Gulden, M. E. "Solid Particle Erosion of Si_3N_4 Materials." Wear 69 (1981); 115-129.

[10] Evans, A. G., M. E. Gulden, and M. Rosenblatt. "Impact Damage in Brittle Materials in the Elastic-Plastic Response Regime." Proc. Roy. Soc. Lond. A. 361 (1978): 343-65.

[11] Gulden, M. E., "Solid-Particle Erosion of High-Technology Ceramics (Si_3N_4, Glass-Bonded Al_2O_3, and MgF_2)." In Erosion: Prevention and Useful Applications, ed. W. F. Adler, 101-121. Philadelphia: ASTM STP 664, 1979.

[12] Gulden, M. E. "Effect of Number of Impacts on Erosion of Polycrystalline MgF_2 in the Elastic-Plastic Response Regime." Journal of American Ceramic Society 63 (1980): 121-26.

[13] Evans, A. G. "Impact Damage in Ceramics." In Fracture Mechanics of Ceramics Vol.3, ed. R. C. Bradt, D. P. H. Hasselman and F. F. Lange, 303-331. New York: Plenum Press 1978.

[14] Preece, C. M., ed., Treatise on Materials Science and Technology Vol. 16, 69-126. Erosion by Solid Particle Impact, by A. W. Ruff and S. M. Wiederhorn. New York: Academic Press, 1979.

[15] Zhou, J. and Bahadur S. "The Effect of Material Composition and Operational Variables on the Erosion of Alumina Ceramics." to appear in Wear.

[16] Scattergood, R. O. and J. L. Routbort. "Velocity Exponent in Solid-Particle Erosion of Silicon." Communications of the American Ceramic Society (October 1983): C-184-C-186.

[17] Ritter, J. E., P. Strzepa, K. Jakus, L. Rosenfeld, and K. J. Buckman. "Erosion Damage in Glass and Alumina." Journal of the American Ceramic Society 67 (1984): 769-74.

[18] Scattergood, R. O. and J. L. Routbort. "Velocity and Size Dependences of the Erosion Rate in Silicon." Wear 67 (1981): 227-232.

[19] Mehrotra, P. K., G.A. Sargent, and H. Conrad. "A computer simulation of the time dependence of the erosion of Pyrex glass by glass beads." Journal of Materials Science 17 (1982): 1049-58.

[20] Finnie, I. "Erosion of surfaces by solid particles." Wear 3 (1960): 87-103.

[21] Mehrotra, P. K., G. A. Sargent, and H. Conrad. "A Model for the Multiparticle Erosion of Brittle Solids by Spherical Particles." In Corrosion-Erosion Behavior of Materials, ed. K. Natesan, 125-45. Warrendale: The Metallurgical Society of AIME, 1980.

[22] Ritter, J. E. Jr. and R. W. Davidge. "Strength and Its Variability in Ceramics with Particular Reference to Alumina", Journal of the American Ceramic Society, 67 (6) (1984): 432-37.

[23] Evans, A. G., "Structural Reliability: A Processing Dependent Phenomena", Journal of American Ceramic Society, 65 (3) (1982): 127-37.

[24] Wiederhorn, S. M. and B. J. Hockey. "Effect of Material Parameters on the Erosion Resistance of Brittle Materials." Journal of Materials Science, 18 (1983): 766-80.

[25] Morrison, C. T., J. L. Routbort, and R. O. Scattergood. "Solid Particle Erosion of Mullite." Wear 105 (1985): 19-27.

[26] Söderberg S., S. Hogmark, U. Engmant, and H. Swahnt. "Erosion Classification of Materials Using a Centrifugal Erosion Tester." Tribology International 14 (6) (1981): 333-43.

[27] Naim, M. "Mechanisms of Erosion in Single Particle Impacts" (MS thesis, Iowa State University, 1981).

[28] Zhou, J. R. and S. Bahadur. "High-Temperature Erosion-Corrosion Behavior of Stainless Steels." In Corrosion & Particle Erosion at High Temperatures, ed. V. Srinivasan and K. Vedula, 315-33. Warrendale: TMS, 1989.

PART IV.

EROSION CHARACTERISTICS OF ALUMINA CERAMICS AT HIGH TEMPERATURES

ABSTRACT

The elevated temperature erosion behavior of alumina ceramics has been studied. There were five kinds of aluminas used in this study, with and without the silicate glassy phase and zirconia. The variables studied included temperature variation, material composition and microstructure, and impingement velocity and angle. The erosion mechanisms were also investigated for both the normal and oblique impacts. Erosion experiments were run in a sand-blast type of test rig using 120 grit silicon carbide particles. The variation in erosion as a function of temperature is explained in terms of the changes in material properties and microstructures. The examination of eroded surfaces revealed that the erosion characteristics of aluminas at elevated temperatures were significantly different from those at ambient temperature. There was plastic deformation occurring on the eroded surfaces at high temperatures and shallow impingement angles. The erosion of aluminas at elevated temperatures was thus not uniquely governed by the indentation fracture model and new modifications and factors needed to be considered.

INTRODUCTION

In recent years there has been increased interest in using ceramics for energy production, aerospace and other advanced engineering applications because of their chemical stability, relatively high hardness and strength at high temperatures. Above some critical high temperature, metallic alloys (which generally cannot sustain continuously temperatures in excess of 850 ^{o}C in the stressed condition) undergo substantial changes in properties and severe oxidation, both of which dramatically affect the life and efficiency of a device. Compared to metals, ceramics are also much less prone to damage from corrosive environments. The utilization of ceramics in energy production offers improvements in thermal efficiency, avoids the necessity of complex cooling system, decreases weight, lowers stresses in rotating components, and allows higher thrust-to-weight ratios. If ceramics are to become a reality in these applications, the problem of high temperature erosion, besides reproducibility, uniformity and reliability, must be solved, since many applications for ceramics involve erosive environments. The typical examples of such potential applications are the key components in the hot section of a gas turbine engine such as blades, nozzle guide vanes, shroud rings, reheater and combustor components.

The two elastic-plastic fracture models, namely, the quasi-static and the dynamic, have been used to explain the erosion of ceramics [1-8]. It was reported that the indentation model predicted well the impact damage in glass [9] and small grain size hot-pressed silicon nitride [10], but not in large grain size sintered alumina [11]. Ritter et al. [12] also reported that the erosion damage in soda-lime glass could be modeled by the indentation fracture mechanics, but the latter could not account for the erosion of sintered alumina. This shortcoming was attributed to

the microstructural aspects of erosion damage that were not modeled by indentation fracture. Wiederhorn and Hockey [13] examined the erosion data for a variety of ceramics in the light of these two theories. Although a semi-quantitative agreement of the data with the theories was obtained, some discrepancies were apparent. In particular, the dependence of erosion rate on hardness and critical stress intensity factor was greater than that predicted by either of the two theories. Therefore, more work needs to be done so that additional factors may be introduced in the modeling of the erosion of aluminas.

A number of workers [8, 14-15] studied the microfeatures of erosion. They could not find the radial cracks propagating out of erosion pits, which was contrary to the expectation based on the indentation model. Ritter et al. [10] found that the impact damage by SiC particles at room temperature in fine-grained high-and low-purity alumina was characterized by the formation of lateral and radial cracks. Yust and Crouse [16] observed that the erosion damage in bricks, castable alumina and mullite refractories at room temperature and at 470 °C was a combination of brittle fracture and plastic shear.

As for the operational parameters of erosion, it was found [1, 13] that, in general, the erosion rate of ceramics did not vary appreciably with temperature, and that the effect of temperature was larger at shallower impact angles. On the other hand, some studies showed that temperature had a significant influence on erosion rate [1]. It was observed [11] that the angle for maximum erosion in the case of sintered alumina decreased from 90° at 23°C to 45° at 1000°C. These observations indicate that more work is needed to develop an understanding of the role of temperature in erosion. Morrison and Routbort [17] reported that for impingement angle $\alpha > 15^{\circ}$ only the

normal component of velocity had to be considered since brittle fracture was the main mechanism, but for smaller values of α there was evidence of plasticity as observed in the erosion of mullite ($3Al_2O_3 \cdot 2SiO_2$ with approximately 12% glass phase).

It is normally accepted that for brittle materials, such as ceramics, maximum erosion occurs at normal impact (90° impact) and for ductile materials at shallow impact angles. It was also reported [18] that brittle materials might show a ductile signature as the erodent particle size was decreased.

Since alumina is one of the most versatile refractory ceramic oxides, it finds many applications. Because of its great potential in engineering applications, a good understanding of the high-temperature erosion behavior of alumina ceramic is desired. The present work is a continuation of our earlier work [19] on the erosion of alumina, and involves the investigation of the erosion behavior in terms of the changes in temperature and composition along with other factors.

EXPERIMENTAL DETAILS

Al_2O_3 is a chemically inert material which is stable up to its melting point of 2050 °C, and has a high Young's modulus of elasticity of 400 GN/m^2 [21]. There were five kinds of aluminas used in this study. Their compositions and designations are given in Table 1. Table 2 lists some mechanical properties of the aluminas. The microstructures of these materials were described in our earlier paper [19]. All of these materials were ball-milled with water, spray dried, and pressed in a steel die at 82.5 MPa and sintered at 1550 °C for 2 hours. The specimens were polished with diamond paste and lapping oil to remove surface contaminations and surface flaws.

Erosion experiments were run in a vertical sand-blast high temperature erosion test rig whose details were reported elsewhere [20]. The test temperatures were 25, 200, 400, 500, 650 and 800 °C. SiC particles in grit size 120 (average diameter 151 μm) were used as the erodents. These were accelerated in air and their concentration in the fluid stream was 0.0066 g/mm^2s. Most experiments were performed at an impingement velocity of 50 m/s. A number of velocities in the range of 40 to 90 m/s were used to study the effect of changes in the dynamic energy of impact particles on erosion. The impingement angles were varied from 10° to 90° in order to study the dependence of erosion rate on impact angle. Most erosion experiments were carried out at an impingement angle of 90° because maximum erosion in brittle materials occurs under normal impact. The duration of each test was 70 minutes with a total of 250 g particles impacted.

The features of the eroded surfaces and the substrates were examined by scanning electron microscopy. The scratch tests were also performed with the objective of understanding the mechanisms involved in erosion.

Table 1: Compositions and mean grain sizes of alumina ceramics

Manufacturer code[a]	Composition	Mean grain size (μm)	Designation used here
2140	90% alumina + 10% silicate glassy phase	7.6	Al10Si
6928	96% alumina + 4% silicate glassy phase	6.2	Al4Si
M-RCHP-4PD	99.5% alumina	8.0	Al
6935	zirconia-toughened alumina + 4% silicate glassy phase	6.0	ZTA4Si
ZTA-GF-A	zirconia-toughened alumina	6.0	ZTA

[a]Champion Spark Plug Company, Detroit, Michigan.

Table 2: Mechanical properties of alumina ceramics

	Al	ZTA	ZTA4Si	Al4Si	Al10Si
Hardness, VHN	1,710	1,610	1,260	1,660	1,250
Fracture toughness, MPa$\sqrt{m}$	4.0	5.5	5.5	4.1	3.9
Modulus of elasticity, MPa	344,740	289,580	289,580	303,370	268,900
Compressive strength, MPa	2,758	2,900	2,900	2,620	2,410

RESULTS AND DISCUSSION

Variation of Erosion

Temperature Erosion experiments were performed at six different temperatures and under normal impact condition. The variation of erosion rate with temperature for five kinds of aluminas is shown in Figure 1. Here erosion rate was calculated by dividing the total mass loss of target material by the total mass of erodent particles impacted. From this figure, several general trends can be observed. For most aluminas, erosion rates are almost unaffected by the changes in temperature from ambient to 400 °C. The effect of temperature on erosion is significant above 400 °C and the rate of increase in erosion rate is greater at higher temperatures. For the three aluminas (Al4Si, Al10Si and ZTA4Si) containing silicate glassy phase, there is a slight drop in erosion rate at 200 °C. In general, it can be concluded that erosion rate is affected very little by temperature below 400 °C, and above that it increases with increasing temperature. The erosion rate at 800 °C is 1.7 - 2.2 times that at room temperature. It is further noted that the erosion rate of single phase alumina is the highest whereas that of alumina with 4% silicate glassy phase is the lowest.

Based on the elastic-plastic theory, the theoretical model proposed [2, 18] for the erosion of brittle materials at normal impact is

$$\dot{\epsilon} \propto V^n D^m \rho^u K_c^p H^q$$

where $\dot{\epsilon}$ is erosion rate, V, D and ρ are the particle velocity, diameter and density, and K_c and H the fracture toughness and hardness of the target material, respectively. Here, the exponent p has a negative value. In agreement with this, our study on the erosion of aluminas at room temperature also showed that erosion resistance

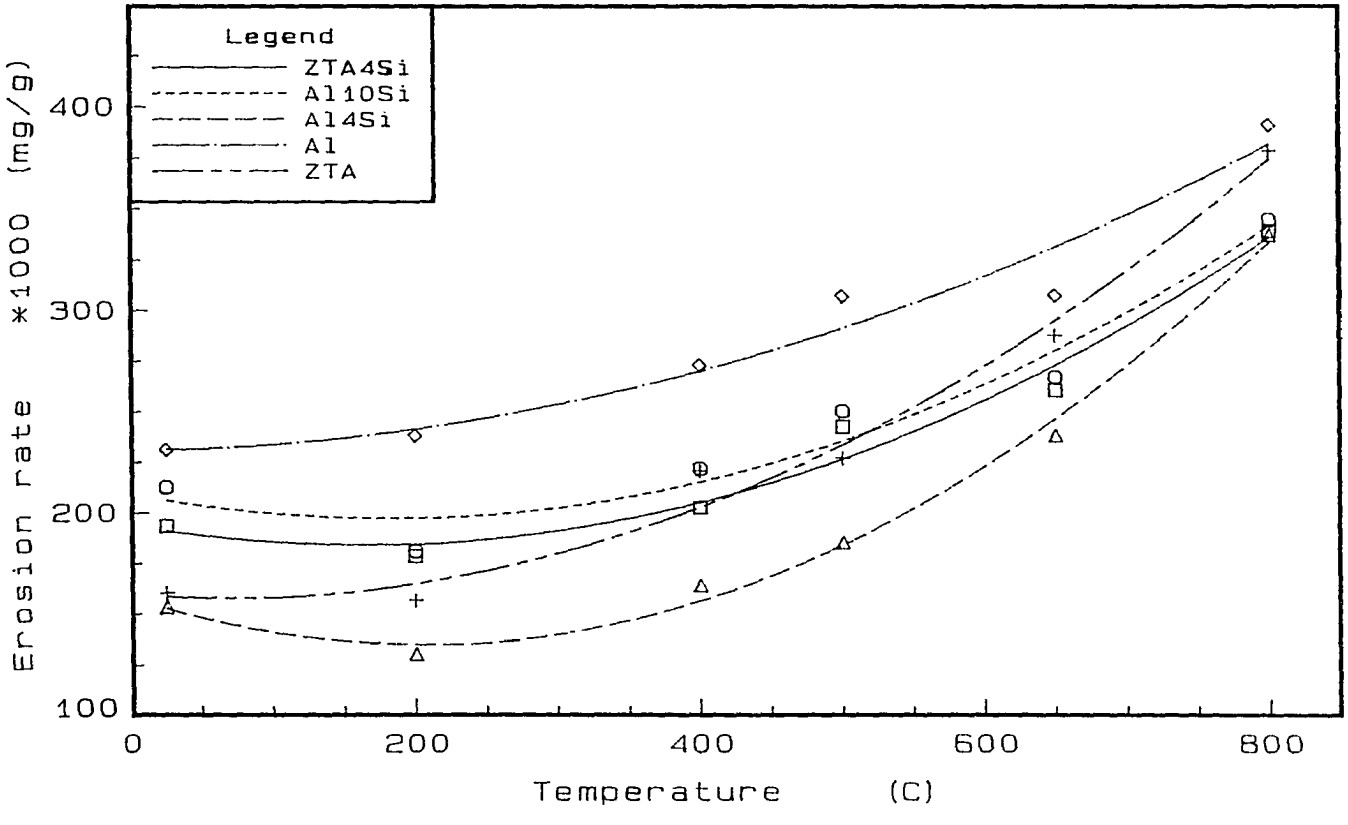

Figure 1: Variation of erosion rate as a function of temperature at normal impact (velocity: 50 m/s)

Table 3: Tensile strength of sintered alumina [24]

Temperature °C	Tensile strength, MPa	Temperature °C	Tensile strength, MPa
20	259.87	1200	127.49
300	251.05	1300	44.13
800	235.36	1400	29.42
1050	233.40	1460	10.79
1130	216.73		

increased with the increase in hardness [19]. It should thus be possible to examine the variation of erosion rate with temperature in terms of the changes in the relevant properties with temperature.

It has been found [23] that the yield strength of alumina drops with increasing temperature to quite a marked degree. This drop in hardness with temperature occurs even more rapidly. The decline in strength is more if a substantial amount of glassy phase is present. Table 3 gives the variation of the tensile strength of 98% sintered alumina with temperature. It shows a modest drop in tensile strength up to 1130 °C and after that the drop occurs rapidly. With the presence of glassy phase in alumina, the drop in strength will occur at much lower temperature because of the softening of secondary phase. In the long-term (as would be the case in practice), subcritical crack growth is enhanced by increased temperature, and the decline in strength is more significant than it is in short-term. The impact strength of sintered alumina also decreases slightly with increasing temperature and falls sharply after 800 °C [23]. Since the decrease in the hardness and the strength of aluminas with temperature will lead to the increased penetration of particles on impact, surface damage, enhanced subcritical crack growth etc., the erosion resistance will also be decreased, as observed in Figure 1.

According to the erosion equation presented above, erosion resistance increases with increased fracture toughness. Whereas erosion at room temperature under normal impact condition involves damage by brittle mechanisms, there is evidence of plasticity in erosion as the temperature is increased. Thus, although brittle fracture is still operative, more ductile fracture mechanisms will be involved with increasing temperature. When heated to a temperature high enough, alumina undergoes a progressive increase in plastic deformability and approaches the plastic behavior of metals at room temperature [22]. For aluminas which contain glassy phase at grain boundaries, the change from brittle to semiplastic behavior occurs at lower temperatures. For instance, sintered alumina eroded by 46 grit SiC particles was reported [11] to undergo the transition in maximum erosion rate from an impingement angle of 90° at 23 °C to 45° at 1000 °C. This observation indicates that the above change occurred because brittle erosion at 23 °C changed to ductile erosion at 1000 °C. The enhanced dislocation activity and other plastic flow characteristics are specially promoted at shallow impact angles. From the above observations, it was concluded that the role of brittle cracking and, therefore, fracture toughness will not be significant at high temperatures.

It was reported by some workers [1, 13] that the change in temperature had a marginal effect on erosion rate. This conclusion was derived from the comparison of erosion data at 1000 °C with that at room temperature or at low-medium temperatures. As seen from our results in Figure 1, this is not universally true. It is possible that in some materials there is no significant change in erosion rate due to the considerable improvement in ductility which competes with the decrease in strength/hardness of material. It should be noted in this context that enhanced duc-

tility tends to lessen the concentration of stresses around the vicinity of cracks and other defects and thus reduces erosion while decreased strength results in increased erosion.

It is possible to explain the erosion rate of various alumina compositions in terms of their microstructures. From Figure 1 it is seen that the aluminas with secondary phase and zirconia are more erosion-resistant than pure alumina at all temperatures. This is so because the mechanical properties and the microstructures of aluminas are changed beneficially by the addition of these phases. For example, the presence of zirconia in alumina enhances its compressive and flexural strengths and fracture toughness which contribute to increased erosion resistance. For those two aluminas with silicate glassy phase (Al4Si and Al10Si), the presence of glassy phase at grain boundaries makes these regions less prone to brittle cracking both at room and elevated temperatures.

The impurities initially dissolved in alumina tend to migrate to grain boundaries during the periods of grain growth in firing and subsequent cooling [22]. Then, there are grain boundary regions in which the lattices from adjacent grains do not match because of different orientations of the neighboring grains and are, therefore, subject to internal stresses. The contaminated and stressed grain boundaries make single phase alumina weak and prone to damage by external impacts, because these provide easy paths for crack propagation. In contrast to that, with the presence of glassy phase along grain boundaries or the uniform distribution of zirconia particles between alumina grains, a new kind of "boundary" is formed. The glassy phase and/or zirconia particles provide relief from external impacts by either transferring load to neighboring grains or consuming a part of impact energy by stress-induced

toughening. The glassy phase may also improve ductility at elevated temperatures. By comparison, almost all of the impact energy in single phase alumina is consumed by brittle crack initiation and propagation because there is much less resistance to cracking.

It is also seen from Figure 1 that the erosion rate of alumina containing 4% silicate glassy phase is lower at all temperatures than that with 10% silicate glassy phase. This could be so because with the increased percentage of glassy phase the deterioration in strength occurs. It is possible that there is an optimum percentage of glassy phase for maximum erosion resistance. The lower erosion resistance of the higher percentage glassy phase alumina is attributable to the presence of a substantial amount of glassy phase which causes deterioration in the strength of alumina.

Impact velocity The variation of erosion rate $\dot{\epsilon}$ with particle impact velocity V for materials is found to be of the form, $\dot{\epsilon} \propto V^n$. This dependence was studied for Al4Si at 650 $^{\circ}$C and in normal impact condition, and the results are plotted in Figure 2. From the straight line behavior on log-log scale, the velocity exponent of 1.6 was determined. This value is lower than 2.6 that was obtained for room temperature erosion [19]. The velocity exponent n has also been reported to decrease with the increase in particle size [1, 24-26]. The decrease here was attributed to the heating effects associated with large particle impacts. The external heating, as in our case, would also thus be expected to reduce the value of the exponent.

The decrease in the value of n for Al4Si at the elevated temperature is attributed to the dissipation of impact energy by the secondary glassy phase. At high temperatures, the secondary glassy phase softens and so undergoes more plastic deformation

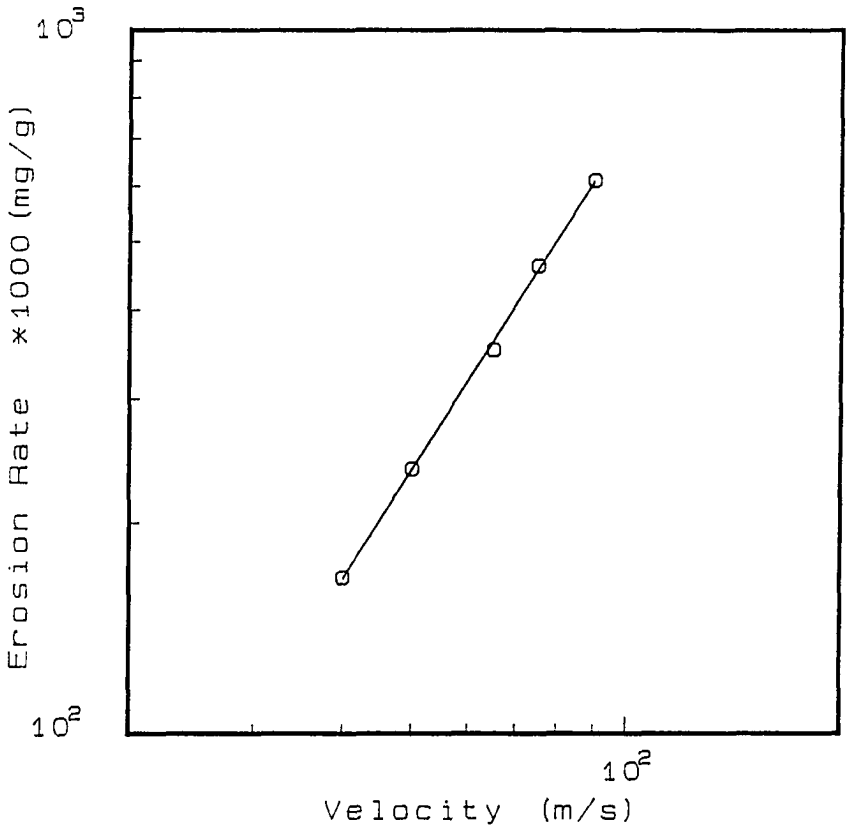

Figure 2: Variation of erosion rate as a function of impingement velocity at 650°C and normal impact

upon external impacts. This results in the dissipation of impact energy, and the higher the impact energy, the more energy is absorbed. Some of this energy is consumed in the form of internal friction. Generally, the effect of internal friction is small below 900 °C for high-purity alumina, because the plasticity of individual grains is not significant in this temperature range. But for aluminas containing secondary glassy phase, the internal friction effect will be significant at much lower temperatures. For instance, 95% alumina showed significant internal friction above 400 C, with the damping rising rapidly beyond 700 °C, and 88% alumina showed a high level of damping even at temperatures between 200 °C and 400 °C [23]. It is the viscous nature of the secondary glassy phase at elevated temperatures that serves as the main contributor to internal friction, which is evident at all frequencies. It should be recognized that the loading in erosion is a cyclic loading and unloading process at the point of impact where the target surface layer undergoes localized stress-release cycle, similar to the case of low cycle fatigue.

Impingement angle Considering the brittle character of ceramic materials, maximum erosion rate would be expected to occur at normal impact. This was indeed found to be the case for room temperature erosion [19]. The dependence of erosion on impingement angle was examined in this work for Al4Si at 650 °C and at an impact velocity of 50 m/s. The plot in Figure 3 shows that even at 650 °C erosion rate peaks at 90°. This indicates the dominance of the brittle fracture mechanism in the erosion of the material at as high a temperature as 650 °C. With increased temperature the brittle fracture in erosion is likely to be reduced, particularly so in the presence of secondary phases. In that case, maximum erosion would occur at

lower impact angles.

The material removal mechanism is strongly affected by impact angle. It changes from brittle to ductile especially at shallow impact angles. This is revealed by the microtopography of impact damaged surfaces and will be discussed later.

Erosion Mechanisms

Normal impacts Figures 4 (a) and (b) show the surface features of Al4Si eroded at 800 °C at an impingement angle of 90° and a velocity of 50 m/s, while Figure 4 (c) shows the features for room temperature erosion under the same conditions. There are distinct differences between the microfeatures of the two cases. The morphology of the surface eroded at room temperature is typical of brittle failure where material is chipped mainly along grain boundaries. The features corresponding to 800 °C indicate plastic deformation as well as brittle failure. Figure 4 (a) shows that an erodent particle penetrated deeply into the substrate. There are no cracks and the surrounding material has undergone severe plastic deformation. After the alumina grain was chipped away, the material left in its location seems to be the silicate glassy phase in plastically deformed condition. Some morphological differences can also be seen in the halo zone of the erosion crater formed at 800°, as shown in Figure 4 (d). The damaged surface gives an appearance of localized rounded features and there is some evidence of plowing. In contrast to this, the halo zone for erosion at room temperature was reported earlier [19] to be jagged and faceted, giving an appearance of brittle fracture.

The morphological features of pure alumina(Al) eroded at 800 °C and shown in Figure 5 are different from those described above. At room temperature, the

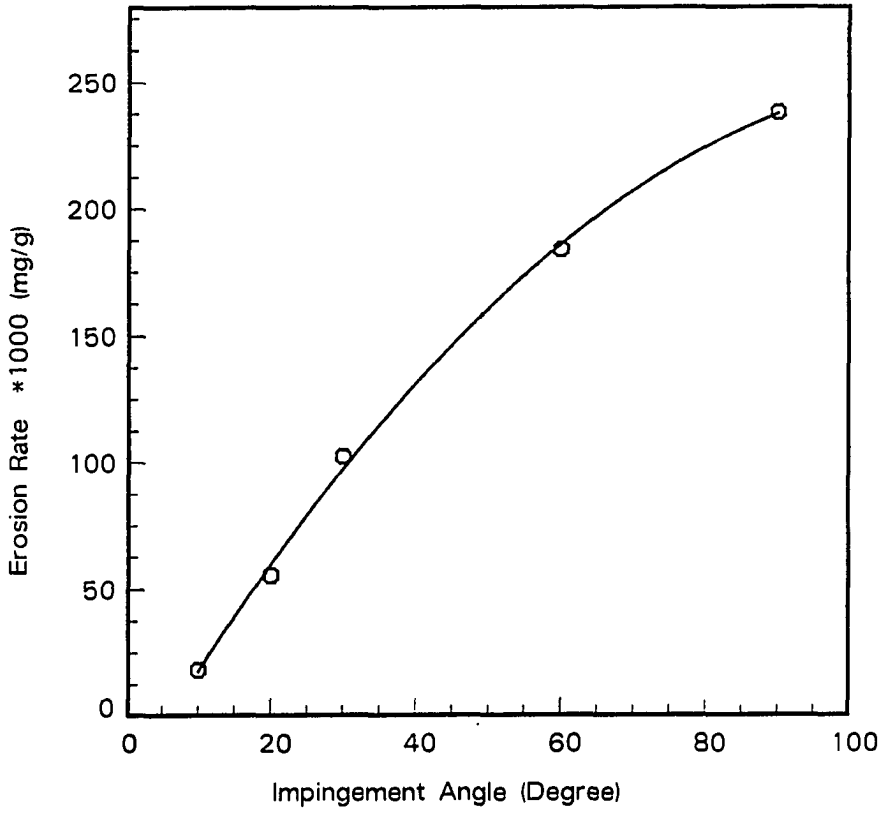

Figure 3: Variation of erosion rate as a function of impingement angle at 650°C and impingement velocity 50 m/s

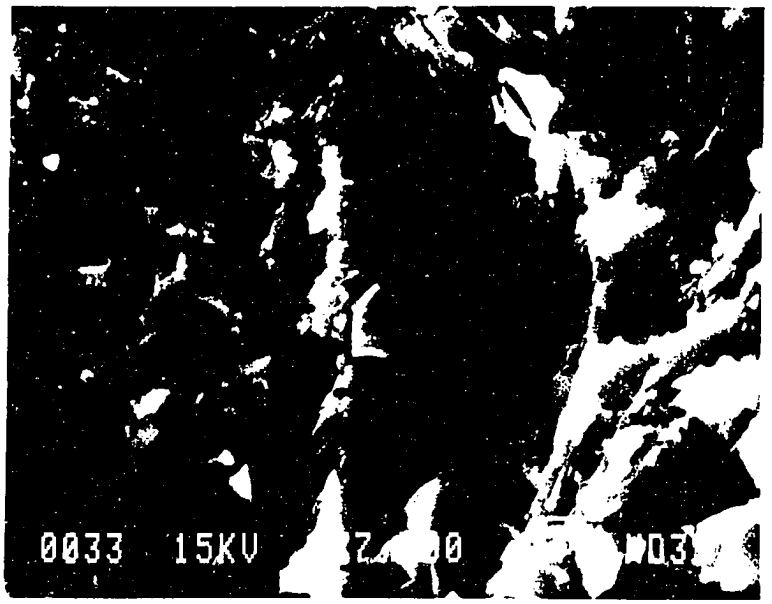

a

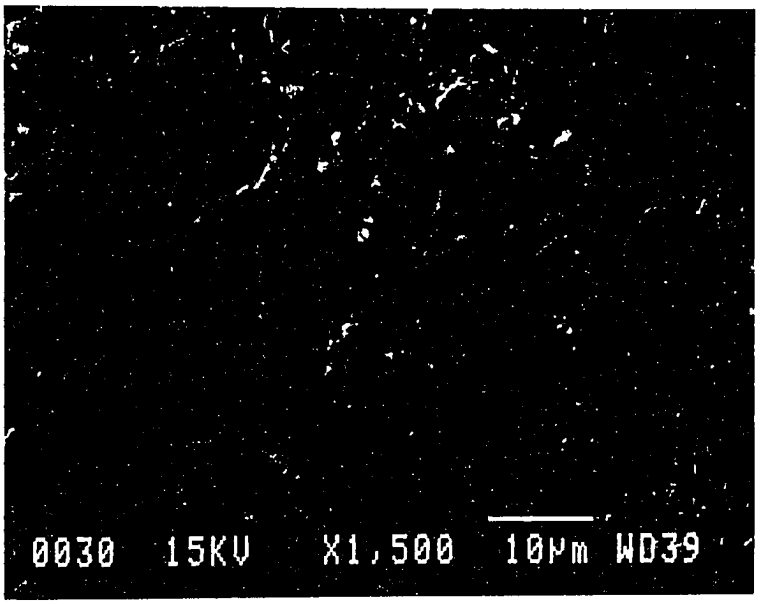

b

Figure 4: SEM micrographs of Al4Si surfaces eroded at normal impingement angle and at (a) 800°C, (b) 800°C, (c) 25°C, and (d) 800°C, halo zone

c

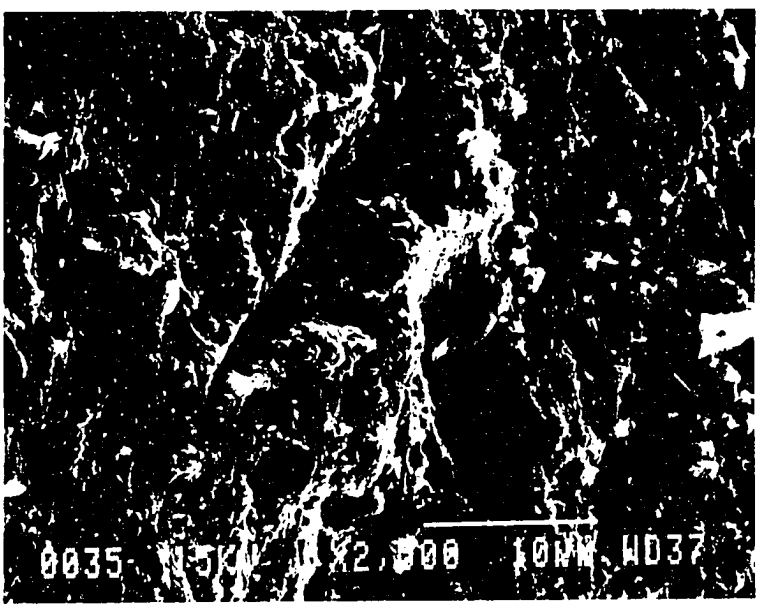

d

Figure 4 (Continued)

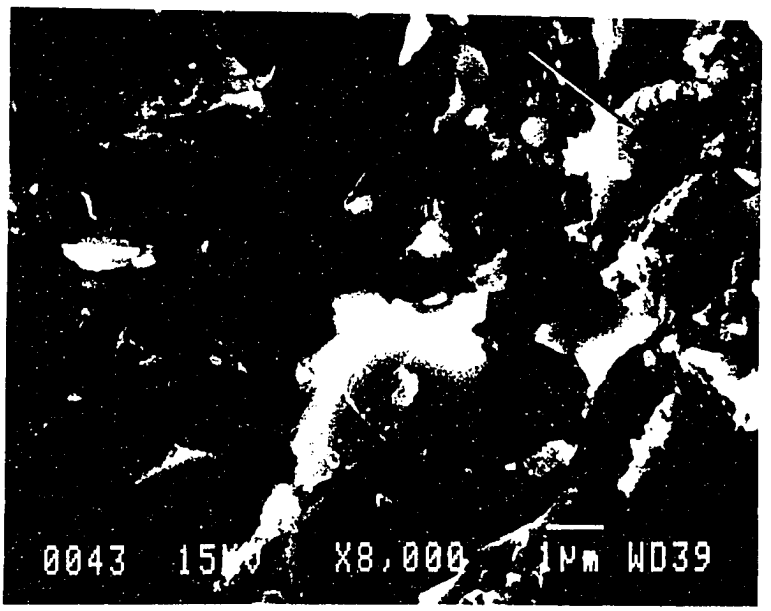

a

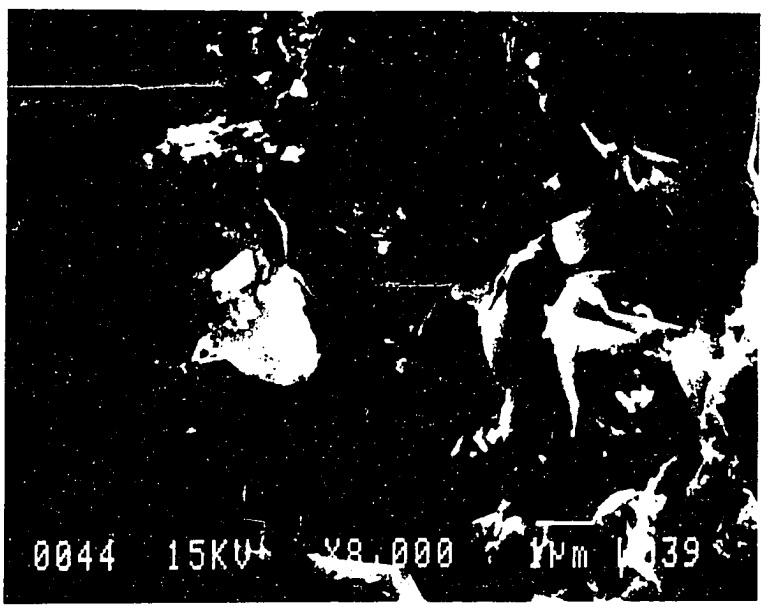

b

Figure 5: SEM micrographs of single phase alumina Al surfaces (for two locations) eroded at 800°C at normal impact angle

microstructural features of Al for room temperature erosion were basically the same as those of Al4Si, with only brittle failure being operative [19]. In case of erosion at 800 °C, unlike Al4Si, single phase alumina showed hardly any plastic deformation except for some traces of it, as indicated by an arrow in Figure 5 (a). This lack of plastic deformation is due to the higher hardness and brittleness of Al and its better ability to retain high hardness at elevated temperatures than the other aluminas with secondary phases. Figure 6 gives the cross-sectional view of the damaged substrate of single phase alumina eroded at 800 °C and normal impact. Here an erosion pit was formed by the loss of a single or perhaps a couple of grains due to intergranular cracking or chipping. The arrow points to a crack located a few microns below the surface, which seems to propagate along a grain boundary. Subsequent impacts would contribute to further growth of the crack so that more grains would be lost.

In ZTA the alumina grains are completely surrounded by smaller size zirconia particles. These particles significantly influenced the morphology of eroded surface, as shown in Figure 7. Figure 7 (a) shows severe plastic shear deformation produced by the sliding action of erodent particles, which is a characteristic feature of ductile metal erosion. Figure 7 (b) shows an erosion pit formed by an impacted particle which is surrounded by the material deformed plastically, as indicated by an arrow. The features of this plastically deformed material are very fine. The morphological features in the micrographs in Figure 7 may be identified as: the faceted grains of relatively large size, and the severely deformed domains with fine features. These two features provide the appearance of typical brittle and plastic behaviors, respectively. Referring to the microstructure of this material, it was concluded that the faceted grains were produced by brittle erosion causing exposure of alumina grains and the

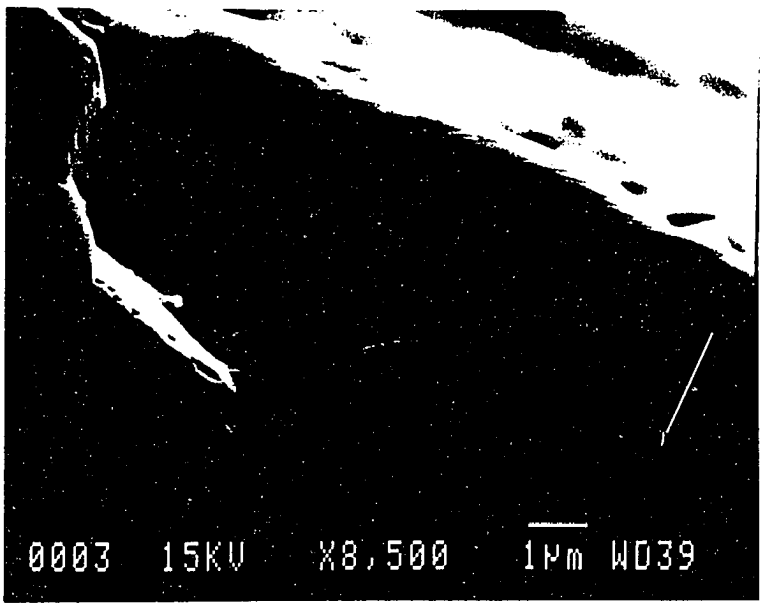

Figure 6: Cross-sectional views of the erosion crater of single phase alumina Al eroded at 800°C and at normal angle

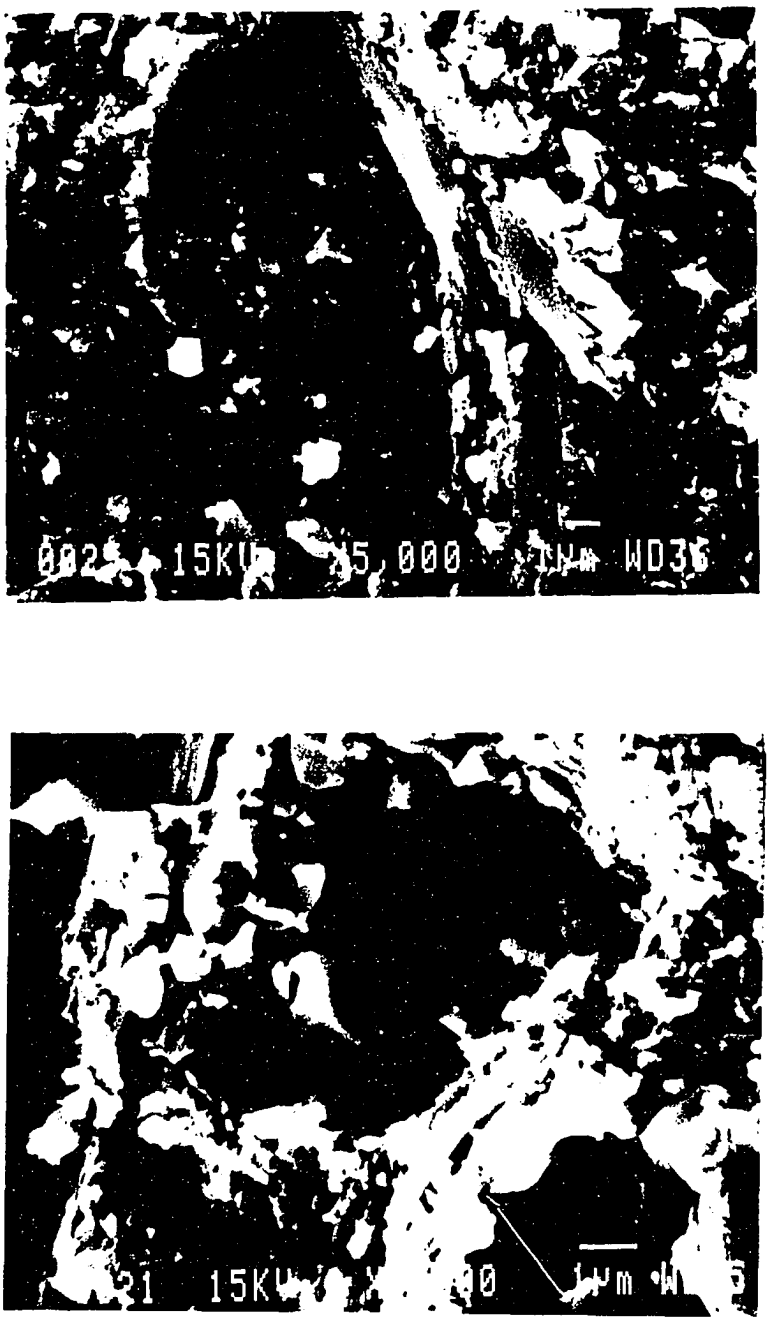

Figure 7: SEM micrographs of ZTA surface from two locations eroded at 800°C and at normal impact angle

deformed domains by the plastic deformation of zirconia particles.

In the case of Al10Si, the glassy phase was softened in erosion at 800 °C, as shown in Figure 8. As such, the glassy material was plastically deformed and condensed by external impacts. It covered most of the area so that alumina grains beneath it could barely be seen.

The morphology of the eroded surface of ZTA4Si exhibited the characteristic erosion features of both Al4Si and ZTA, as shown in Figure 9. Here an embedded particle is seen to have cut deeply into the substrate, comprised mostly of glassy phase or zirconia particles, and fine fragments of the deformed material are formed as seen in Figure 9 (a). Figure 9 (b) shows a domain formed by plastic shear in the glassy phase or zirconia region.

From the above discussion, it is obvious that the morphology of aluminas eroded at elevated temperatures provided sufficient evidence of plastic deformation accompanied by brittle fracture failure. This is in profound contrast to the evidence of room temperature erosion where only brittle fracture mechanism seemed to work. It thus implies that the erosion behavior of aluminas at elevated temperatures would no longer be uniquely governed by the indentation fracture model. Therefore, modifications to the model or additional factors need to be considered.

Oblique impacts The effect of impingement angle on the erosion mechanism was also investigated. Figure 10 shows the surface of Al4Si eroded at 650 °C and at an impingement angle of 10°. Figure 10 (a) provides an overall view of the erosion damaged area in which numerous extended stringers or grooves running along the particle impact direction (from top to bottom) can be seen. These stringers were

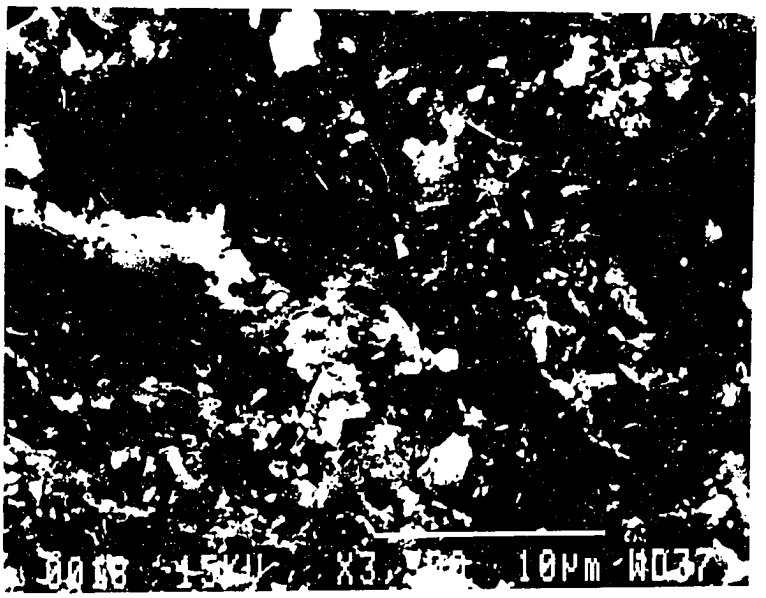

Figure 8: SEM micrograph of Al10Si surfaces eroded at 800°C and at normal impact angle

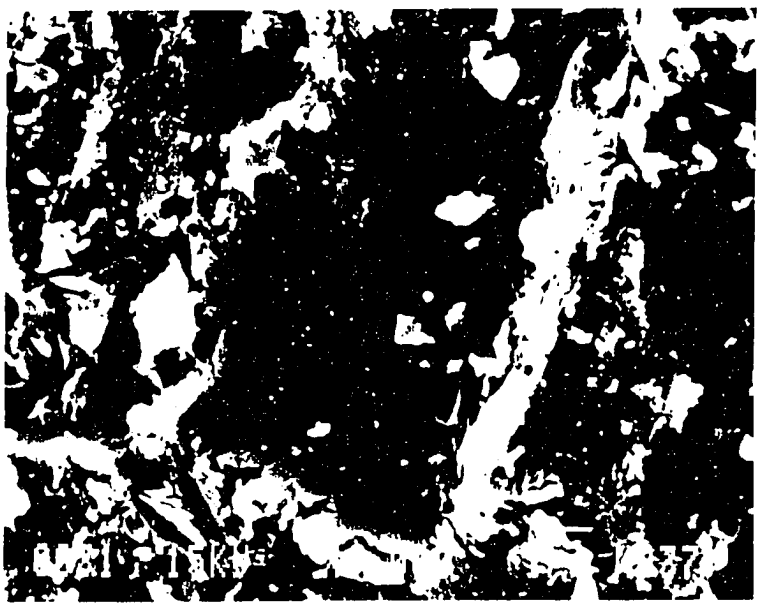

Figure 9: SEM micrograph of ZTA4Si surfaces eroded at 800°C and at normal impact angle

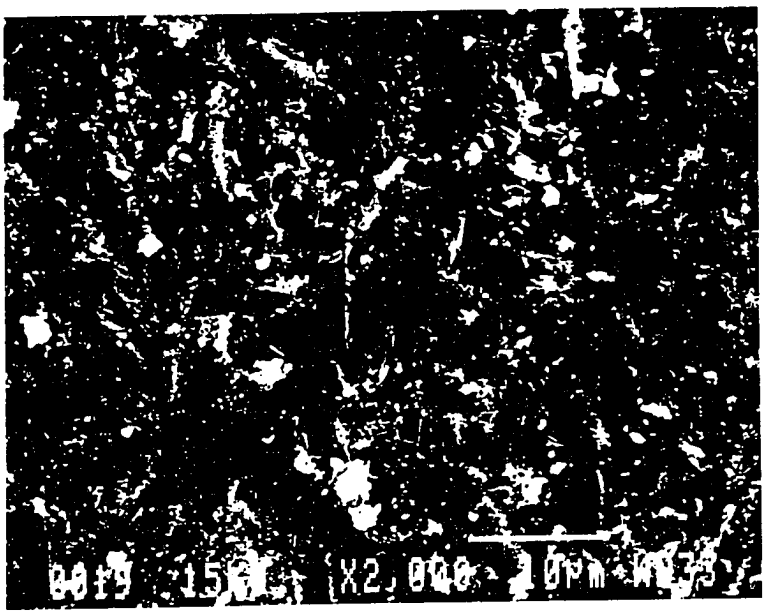

a

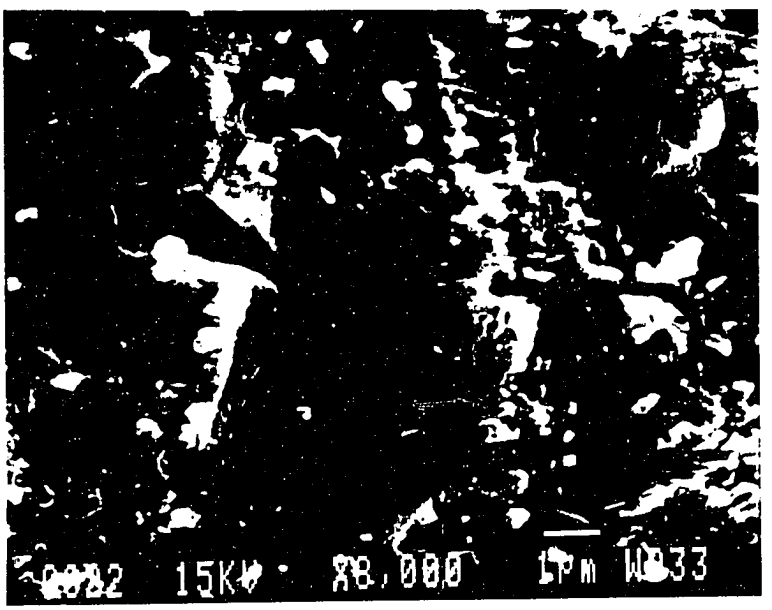

b

Figure 10: Microfeatures of Al4Si eroded at 650°C and at an impingement angle of 10°

c

Figure 10 (Continued)

created by the rubbing, extrusion, ploughing and cutting actions of the impact particles and are typical of ductile erosion. There is also an evidence of brittle cracking which finally led to the fragmentation of material. The morphological features here are quite different from those seen at normal impacts in Figures 4 to 9 at comparable magnifications. The details of plastic deformation can be seen in Figure 10 (b) where a particle cut deeply into the substrate. It produced severe plastic deformation and a groove with smooth bottom. This kind of plowing action is typically observed in the ductile erosion of metals. The other areas in Figure 10 (b) show brittle-fracture features. This kind of combined ductile and brittle features are also seen in Figure 10 (c). Here, in the right part of the micrograph, particles rubbed on the surface producing plastic shearing and forming rub bands. On the left side, an erosion pit was formed by cracking. Since, at the shallow impact angle of 10°, the contact of erodent particles with target surface contributed mainly to plowing and very little to brittle cracking, the erosion at this impact angle is quite low, as seen in Figure 1.

In order to observe the response of alumina materials to the external loading action of the sharp edge of an impacting particle, scratch tests at room temperature were performed. Here a diamond stylus under a load of 70 g was traversed over the polished surfaces of single phase alumina, Al4Si and ZTA. Figure 11 shows that the penetration of diamond stylus was very shallow because of the low load and high hardness of the materials. In all cases, the substrate underwent plastic shear deformation so that smooth bands were formed but the band edges were fractured by brittle mode. The debris resulting from this brittle failure is seen scattered along the sides of the scratch bands. The failure of the edges occurred due to induced tensile stresses. This behavior is different from the case of ductile erosion where

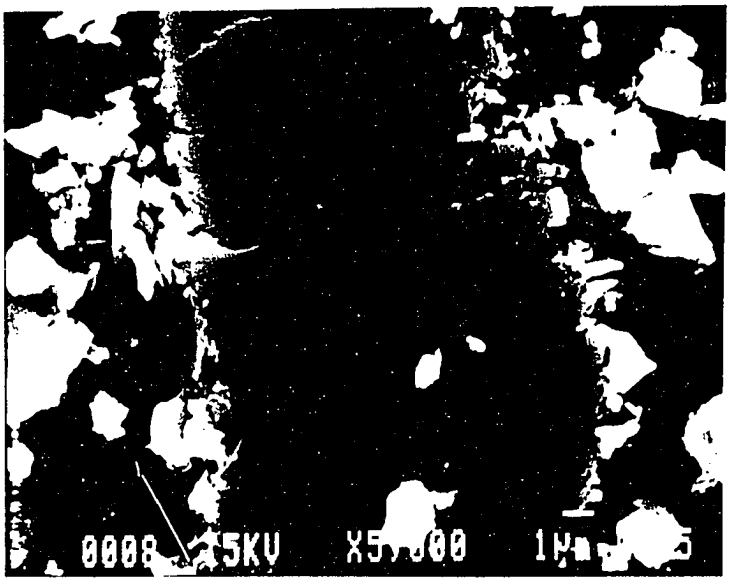

a

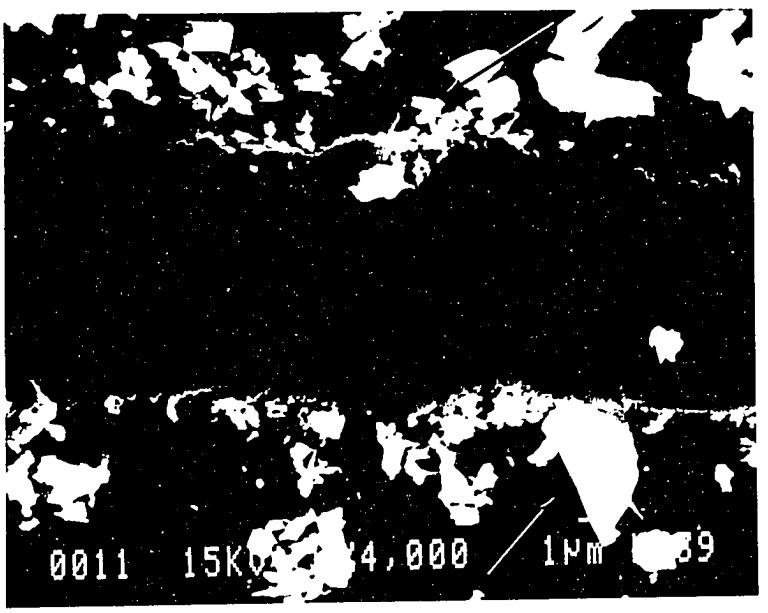

b

Figure 11: Scratches made by diamond stylus on: (a) Al4Si; (b) single phase alumina Al; (c) ZTA

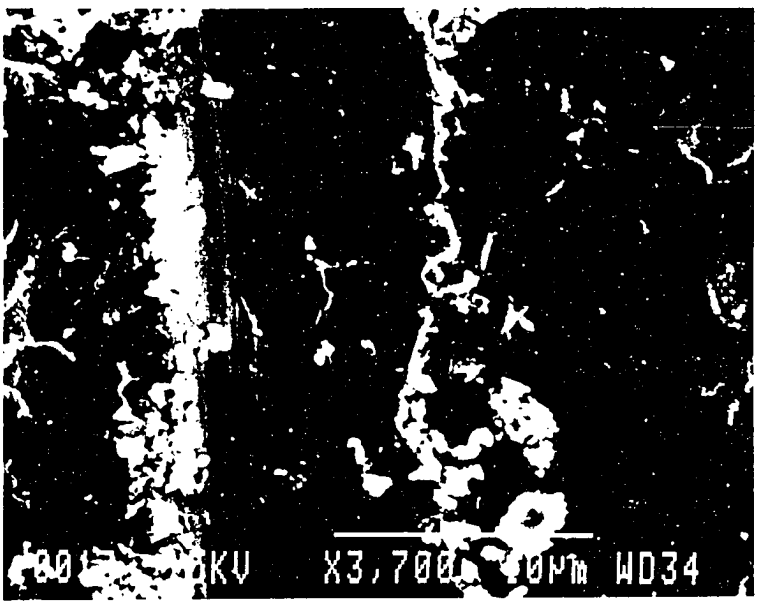

c

Figure 11 (Continued)

the rubbing action of particle usually does not cause direct material loss. There are also lots of cracks seen along the boundaries of the groove which would contribute to fragmentation during subsequent rubbing. The rub band features of ZTA are somewhat different. Here many stringers are extended along the scratch band, which is an indication of more ductile deformation. The latter occurs because of the presence of zirconia particles which deform more easily. Since scratching simulates partially the particle action in oblique impact, the shear deformation as observed here would be expected in oblique erosion as well. The amount of plastic deformation will be much less in actual erosion because of the dynamic impact of particles as opposed to the smooth sliding action of a stylus.

When the impact angle was increased to 20°, the plowing features changed, as seen in Figure 12. Figure 12 (b) shows a rub band formed by plastic shear and the arrow points to a slip band. The material was lost here at the end of the rub band so that a pit is created. The smooth surface of the bottom of the pit indicates that the "bulk" material was separated from the substrate by grain boundary cracking.

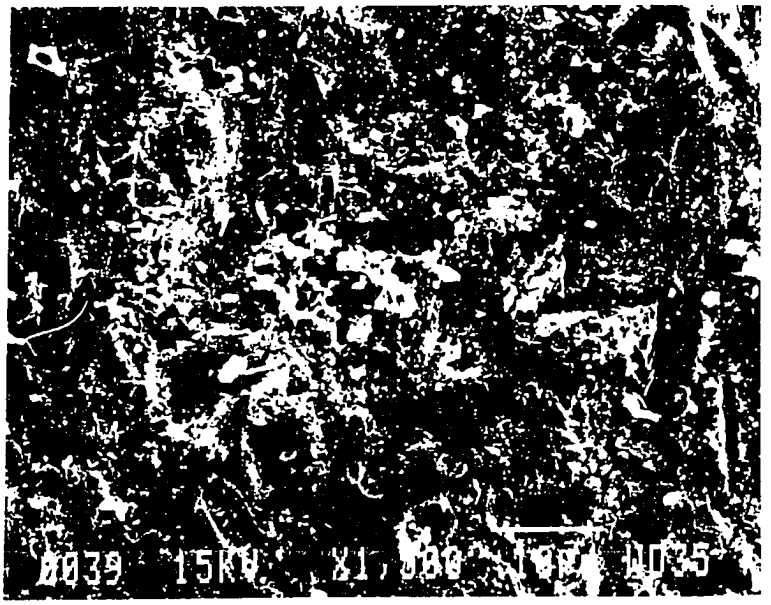

a

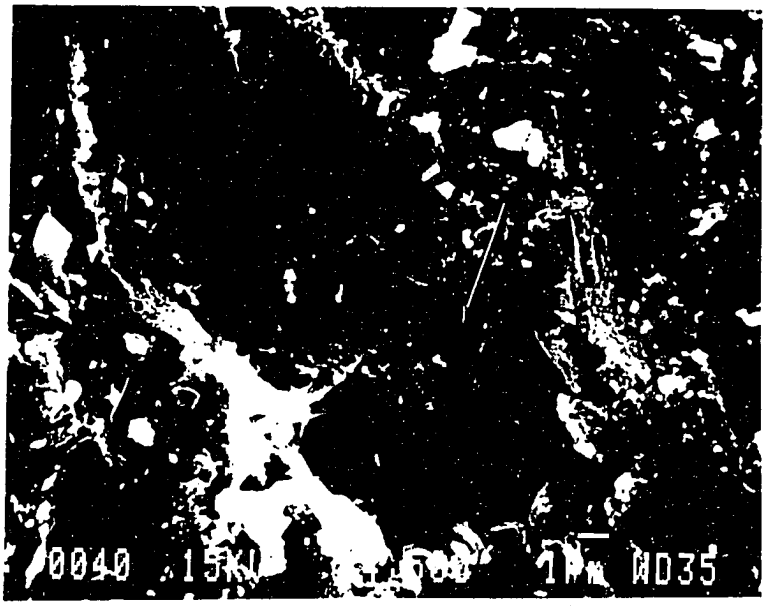

b

Figure 12: Microfeatures of Al4Si eroded at an impingement angle of 20° and at 650°C

CONCLUSIONS

From the erosion studies on alumina ceramics, the following conclusions were drawn:

(1) Erosion rate was not much affected by temperature below 400 °C, but above this temperature it increased with increasing temperature resulting in a larger increase in erosion rate at 800 °C.

(2) The aluminas containing silicate glassy phase and zirconia were more resistant to erosion than single phase alumina at all temperatures.

(3) The erosion rate at 650°C peaked at an impingement angle of 90° which indicates the dominance of brittle failure in the erosion process.

(4) Erosion rate $\dot{\epsilon}$ varies with velocity V according to the relationship $\dot{\epsilon} \propto V^n$ where the exponent n for high temperature is lower than that for room temperature.

(5) Along with erosion rate, the mechanism of erosion also depended upon the impingement angle. At shallower impact angles, there was evidence of more plastic deformation than under normal impact condition.

(6) At elevated temperatures and under normal impacts, there was evidence of plastic deformation on the eroded surface of single phase alumina as opposed to mostly brittle fracture at room temperature. The amount of plastic deformation was considerably more in the case of aluminas with silicate glassy phase and zirconia.

(7) Aluminas can undergo plastic deformation even at room temperature during plowing. Scratch tests exhibited plastic shear deformation on the groove surfaces accompanied by brittle failure of the groove edges.

(8) The erosion conditions, as used in this work, did not produce classical indentation fracture. The likelihood of such a fracture is much less at elevated tempera-

tures because of the evidence of ductile fracture mechanisms. As such, the erosion behavior of aluminas at elevated temperatures will not be uniquely governed by the indentation fracture model.

REFERENCES

[1] Conrad, H. "Erosion of Ceramics." In Corrosion-Erosion- Wear of Materials at Elevated Temperatures, ed. A. V. Levy, 77-94. Houston: NACE, 1987.

[2] Evans, A. G., M. E. Gulden, and M. Rosenblatt. "Impact Damage in Brittle Materials in the Elastic-Plastic Response Regime." Proc. Roy. Soc. Lond. A. 361 (1978): 343-65.

[3] Bradt, R. C., D. P. H. Hasselman, and F. F. Lange, ed. Fracture Mechanics of Ceramics Vol. 3, 303-31, Impact Damage in Ceramics, by A. G. Evans. New York: Plenum Press, 1978.

[4] Gulden, M. E. "Solid-Particle Erosion of High-Technology Ceramics (Si_3N_4, Glass-Bonded Al_2O_3, and MgF_2)." In Erosion: Prevention and Useful Applications, ed. W. F. Adler, 101-21. Philadelphia: ASTM STP 664, 1979.

[5] Preece, C. M., ed. Treatise on Materials Science and Technology. Vol. 16, 69-126. Erosion by Solid Particle Impact, by A. W. Ruff and S. M. Wiederhorn. New York: Academic Press, 1979.

[6] Gulden, M. E. "Solid Particle Erosion of Si_3N_4 Materials." Wear 69 (1981): 115-29.

[7] Wiederhorn, S. M. and B. R. Lawn. "Strength Degradation of Glass Impacted with Sharp Particles - I Annealed Surfaces." Journal of American Ceramic Society 62 (1979): 66-70.

[8] Marshall, D. B., B. R. Lawn, and P. Chantikul. "Residual Stress Effects in Sharp Contact Cracking, II. Strength Degradation." J. Mater. Sci. 14 (1979): 2225-35.

[9] Ritter, J. E., P. Strzepa, and K. Jakus. "Erosion and Strength Degradation in Soda-Lime Glass." Phys. Chem. Glasses 25 (1984): 159-62.

[10] Ritter, J. E., K. Jakus, M. Viens, and K. Breder. "Effect of Microstructure on Impact Damage of Polycrystalline Alumina." Erosion by Liquid and Solid Impact, ed. J. E. Field and J. P. Dear, 55.1-55.6. England: Cambridge, 1987.

[11] Ritter, J. E., L. Rosenfeld, and K. Jakus. "Erosion and Strength Degradation in Alumina." Wear 111 (1986): 335-46.

[12] Ritter, J. E., P. Strzepa, K. Jakus, L. Rosenfeld, and K. J. Buckman, "Erosion Damage in Glass and Alumina." Journal of the American Ceramic Society 67 (1984): 769-74.

[13] Wiederhorn, S. M. and B. J. Hockey. "Effect of Material Parameters on the Erosion Resistance of Brittle Materials." Journal of Materials Science 18 (1983): 766-80.

[14] Lawn, B. R., A. G. Evans, and D. B. Marshall. "Elastic/Plastic Indentation Damage in Ceramics: The Medium/Radial Crack System." Journal of American Ceramic Society 63 (1980): 574-81.

[15] Marshall D. B., "Surface Damage in Ceramics: Implications for Strength Degradation, Erosion and Wear." In Nitrogen Ceramics, ed. F. L. Riley, 635-56. The Hague: Nijhoff, 1983.

[16] Yust, C. S. and R. S. Crouse. "Melting at Particle Impact Sites During Erosion of Ceramics." Wear 51 (1978): 193-96.

[17] Morrison, C. T., J. L. Routbort, and R. O. Scattergood. "Solid Particle Erosion of Mullite." Wear 105 (1985): 19-27.

[18] Sheldon, G. L. and I. Finnie. "On the Ductile Behavior of Nominally Brittle Materials During Erosive Cutting." Journal of Engineering for Industry 88 (1966): 387-92.

[19] Zhou, J. R. and S. Bahadur. "The Effect of Material Composition and Operational Variables on the Erosion of Alumina Ceramics." Wear (accepted).

[20] Zhou, J. R. and S. Bahadur. "High-Temperature Erosion-Corrosion Behavior of Stainless Steels." In Corrosion & Particle Erosion at High Temperatures, ed. V. Srinivasan and K. Vedula, 315-33. Warrendale: TMS, 1989.

[21] Morrell, R. Handbook of Properties of Technical & Engineering Ceramics Part 2: Data Reviews. London: H. M. S. O., 1987.

[22] Ryshkewitch, E. and D. W. Richerson. Oxide Ceramics 109-256. Orlando: Academic Press, Inc., 1985.

[23] Morrell, R. Handbook of Properties of Technical & Engineering Ceramics Part 1: An Introduction for the Engineer and Designer. London: H. M. S. O., 1985.

[24] Routbort, J. L. and R. O. Scattergood. "Anomalous Solid-Particle Erosion Rate of Hot-Pressed Silicon Carbide." Journal of American Ceramic Society 63 (1980): 593-95.

[25] Scattergood, R. O. and J. L. Routbort. "Velocity and Size Dependences of the Erosion Rate in Silicon." Wear 67 (1981): 227-32.

[26] Scattergood, R. O. and J. L. Routbort. "Velocity Exponent in Solid-Particle Erosion of Silicon." Journal of American Ceramic Society 66 (1983): C184.

PART V.

EROSION-CORROSION OF TI-6AL-4V IN ELEVATED TEMPERATURE AIR ENVIRONMENT

ABSTRACT

The erosion-corrosion behavior of Ti-6Al-4V exposed to air environment up to 800°C has been studied. Erosion experiments were performed in a sand-blast type of test rig at eight different temperatures. The specimens were heat treated by annealing and solution treating and aging. The target specimens were eroded with 120 grit silicon carbide particles at impact velocities from 55 to 110 m/s and impingement angles from 10° to 90°. The oxidation behavior was studied by scanning electron microscopy and X-ray diffraction, and the deformation characteristics of oxide scales by static indentation tests. The morphological features of eroded surfaces were studied by scanning electron microscopy. It was found that erosion rate increased with temperature from 200 ° to 800°C where the increase in erosion rate with temperature was fairly rapid from 650 ° to 800 °C. Oxidation was also fairly high in this temperature range and the interaction between erosion and corrosion was quite significant.

INTRODUCTION

Titanium alloys are inferior to heat-resistant alloys such as stainless steels and superalloys for very high temperature applications. Because of their high strength-to-weight ratio and good oxidation resistance, these alloys are very attractive for medium high temperature situations. Since these are widely used in the industries in which elevated temperature erosive environment is often involved, the investigation of their high temperature erosion-corrosion behavior is of a great practical significance. Of all the titanium alloys, Ti-6Al-4V is the most widely used in practice. It is even being considered for the blading section of steam turbines, aircraft turbines and engine compressors. Its current use in the low pressure stages of gas turbines makes it vulnerable to degradation by the high velocity impacts of ingested sand.

The erosion behavior of Ti-6Al-4V at room temperature has been investigated by a few workers [1-4]. The work relating its erosion behavior with its microstructure and mechanical properties has shown that its erosion rate increases on aging due to the precipitation of β phase and α_2 particles and decreases with overaging due to the agglomeration of these precipitates [1]. As for mechanical properties, erosion rate increases with the increase in yield and ultimate strengths and with the decrease in percent area reduction [1]. Emiliani and Brown [3] studied the erosion of this alloy by impacting 210 μm diameter silica spheres normally to the target surface at a velocity of 61 m/s. They reported the development of a smooth protective glassy layer on the eroded surface which, they thought, was produced by the thermal softening of erodents upon impact. This layer was considered to protect the surface partially from erosion because it shielded the surface from direct impacts.

There is very little reported on the high temperature erosion behavior of this alloy. Gat et al. [5] studied erosion rate as a function of temperature up to 204°C at three impingement angles. They found that erosion rate decreased with increasing temperature. The decrease in erosion rate was small at the impact angles of 60° and 90° but it was much larger at 20°. Tabakoff [6] measured the erosion of this alloy by varying temperatures from 16 ° to 704°C, impingement angles from 5° to 90° and impact velocities from 60 to about 300 m/s. It was found that erosion rate increased with the increase in temperature at all velocities, and maximum erosion rate occurred at the impingement angle of 30° at all temperatures. The reasons for these changes were not examined and the erosion mechanisms were not studied.

The present work is an extension of the above studies. It looks specifically at the mechanisms of high temperature erosion-corrosion and the interaction between erosion and corrosion in Ti-6Al-4V.

EXPERIMENTAL

The target material Ti-6Al-4V was used in this study under two heat treatment conditions: solution treated and aged and annealed. The former treatment was done by holding the specimens at 940°C for 1 hour and followed by water quenching, and then aging at 480°C for 4 hours and followed by air cooling. The annealing was carried out by holding the specimens at 770°C for 3 1/2 hours and followed by air cooling.

Erosion-corrosion experiments were performed in a vertical sand-blast type high temperature test rig described elsewhere in detail [7]. The high temperature corrosion-only experiments were done in the same test facility by using the same air flow rate as used in the erosion-corrosion experiments but the erodent particles were missing. The carrier gas used for accelerating the erodent particles was also air.

The test temperatures selected were 25, 100, 200, 400, 500, 650 and 800°C. The impingement velocities were varied from 55 to 110 m/s, and the impingement angles from 10° to 90°. The erodent material was commercial angular silicon carbide particles in 120 grit size. A total of 100 g erodent particles were impacted in 110 minutes. This gave a mass flow rate of 0.0421 g/mm^2s. Erosion rate was calculated by dividing the mass loss of the target material by the total mass of erodent particles impacted. The repeatablility in erosion data was found to be within ± 15%.

Scanning electron microscopy and X-ray diffraction techniques were used to examine the characteristics of oxide films, morphological features, and substrate damage.

RESULTS AND DISCUSSIONS

Erosion

Among the many variables affecting the erosion behavior of Ti-6Al-4V, temperature is an important factor. Figure 1 shows the erosion behavior of Ti-6Al-4V, in both the annealed and the precipitation hardened conditions, as a function of temperature for an impingement velocity of 65 m/s and an impact angle of 30°. For the solution treated and aged specimens, the test temperature was limited to 500°C because higher temperatures would cause overaging of the specimens. There was no significant difference found in the erosion rates of these two differently heat-treated specimens. As for the variation of erosion rate with temperature, there are three distinct ranges of behaviors seen in Figure. In the first range which extends from room temperature to about 200°C, erosion rate was insensitive to temperature changes. Beyond 200°C erosion rate increased moderately with increasing temperature. In the third range which started above 650°C, erosion rate increased rapidly with increasing temperature.

Erosion tests were also carried out on annealed Ti-6Al-4V for the normal impact condition while using the same impingement velocity as in Figure 1. These results are given in Figure 2. By comparing these two figures, it can be seen that similar ranges in terms of the variation of erosion rate with temperature exist for both 30° and 90° impact angles. Although the change in erosion rate with temperature below 650°C is not great in the case of 90° impingement angle, it does show a moderate increase with temperature above 200°C if it is considered that the erosion rate values for normal impingement are much lower than those for 30° impingement. The increase

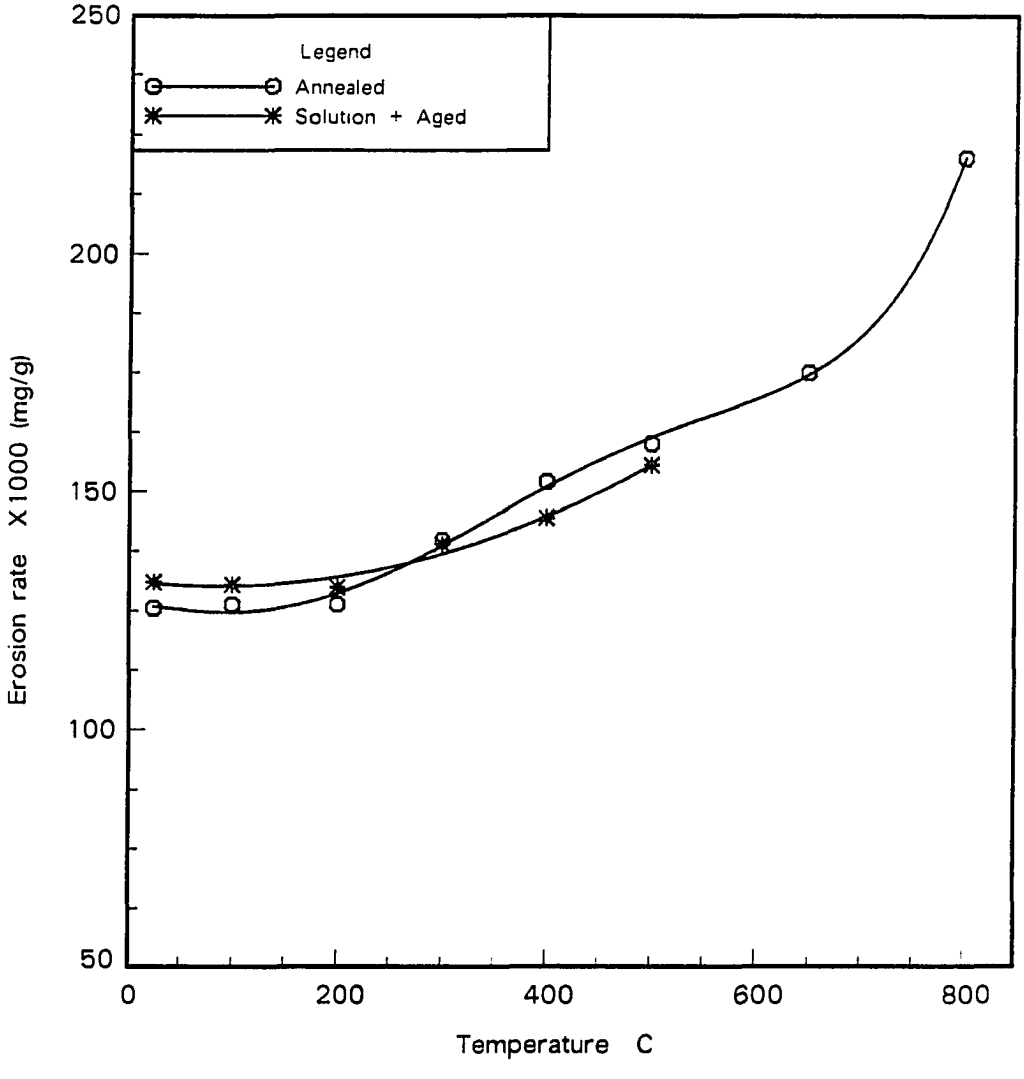

Figure 1: Variation of erosion rate with temperature for Ti-6Al-4V: impingement angle 30°, impingement velocity 65 m/s

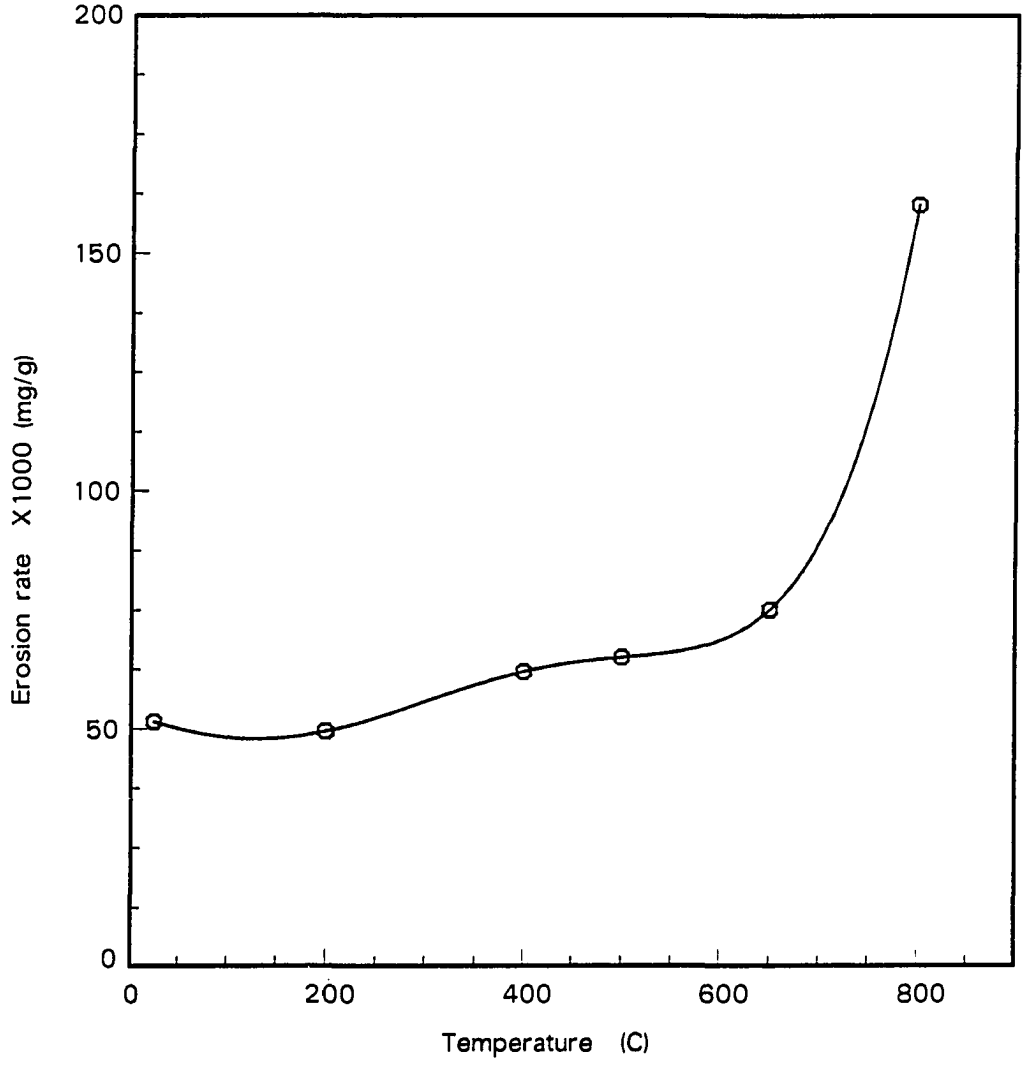

Figure 2: Variation of erosion rate with temperature for annealed Ti-6Al-4V at an impingement angle of 90° and an impact velocity of 65 m/s

in erosion rate above 650°C is much higher for normal impingement than for oblique impingement.

There are two ways in which erosion is influenced by temperature. These are the physical and chemical changes. The physical change manifests itself in terms of the changes in properties with temperature. Whereas titanium alloys exhibit superior stable mechanical properties up to about 550°C, significant changes in mechanical properties occur at higher temperatures. This will be expected to affect the high temperature erosion behavior of the alloy. Figure 3 shows the tensile properties of Ti-6Al-4V as a function of temperature for both the annealed and the precipitation hardened conditions where the conditions for the second treatment are close to those used in this work. It can be seen that tensile strength decreases as temperature increases and at 600°C is about half of that at room temperature. The percent elongation initially increases with temperature, shows a distinct drop between 200 and 400°C, and increases again with further increase in temperature. The erosion behaviors shown in Figures 1 and 2 are closely related to these changes in mechanical properties. The decrease in the mechanical strength of the alloy makes it less resistant to erosion while the increase in ductility contributes to increased erosion resistance [7]. The three distinct ranges of behaviors in Figures 1 and 2, as described above may be explained in terms of the changes in mechanical properties. In the first range from ambient to 200°C, the changes in strength and ductility compete each other in affecting the erosion behavior so that erosion rate practically remains unchanged. Erosion rate increases in the range 200-400°C because both ductility and tensile strength drop with temperature. When the temperature is raised above 650°C, the chemical activity of the alloy becomes a predominant factor in controlling the erosion-

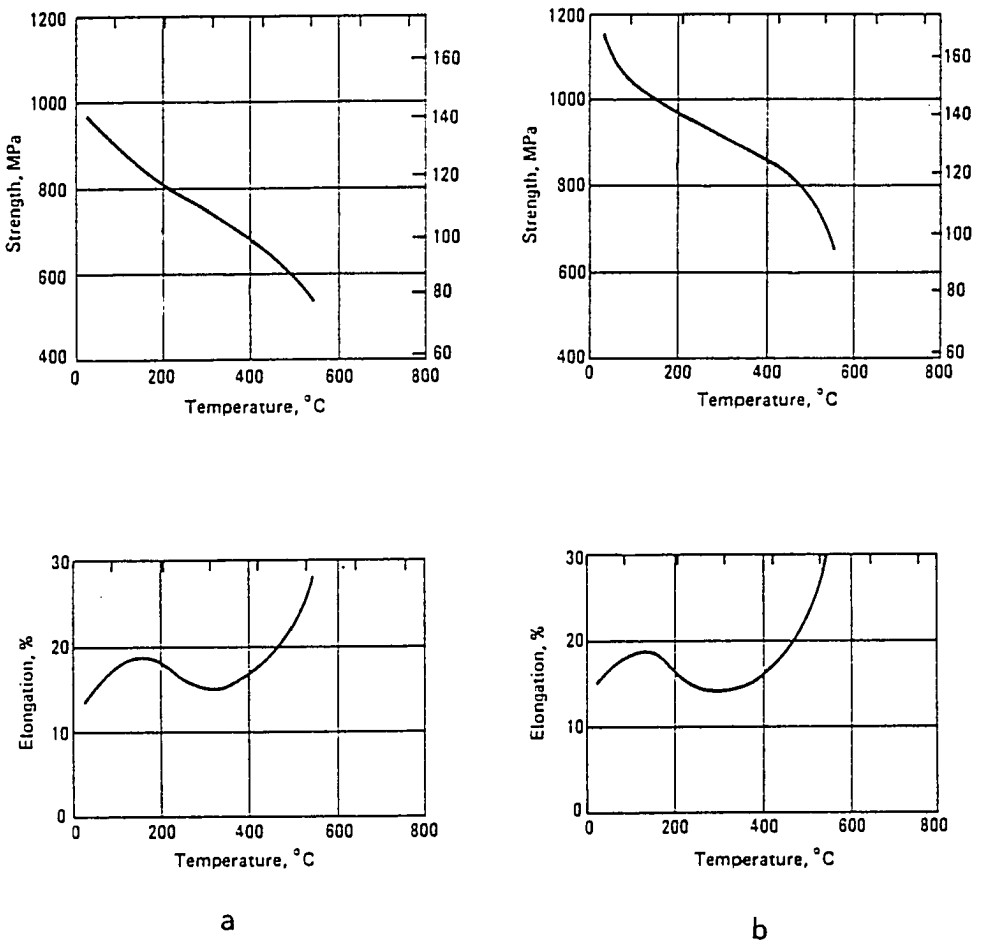

Figure 3: Variations in tensile properties of Ti-6Al-4V with-temperature (a) annealed condition and (b) solution treated for 1 h at 955°C and aged for 4h at 525°C [15]

corrosion behavior. Rapid corrosion and poor properties of the oxide scale formed on the specimen surface contribute to accelerated erosion rate in the temperature range 650- 800°C, as will be analyzed later.

The effect of impingement angle on erosion rate was investigated by performing erosion experiments at 500°C and varying the impingement angles from 10° to 90°. As shown in Figure 4, erosion rate peak appeared around 20°. Since the erosion peak at room temperature for this material was reported [1] at 30°C, there is a small shift in peak to a lower impingement angle at the higher temperature. The erosion rate peak in the impingement angle range of 20 to 30° is typical for ductile materials at room temperature [8-10]. Similar behavior was also reported [7] for 304 stainless steel which exhibited the erosion peak at 30° for room temperature and 20° for 500°C.

Figure 5 shows the effect of impingement velocity on the erosion rate at 500°C and at an impingement angle of 30°. If an exponential relation between erosion rate ($\dot{\epsilon}$) and velocity (V) of the form $\dot{\epsilon} \propto V^n$ is assumed, the plot provides the exponent value of 1.89. The value of this exponent reported for room temperature is usually more than 2 [1, 11]. This indicates that erosion is less sensitive to impingement velocity at high temperatures. The change in the value of the exponent noted here is consistent with the earlier observations on other materials [9,11,12].

Corrosion

As the test temperature is increased, high temperature corrosion becomes more important in the erosion-corrosion process. It has been reported [13] that under some conditions corrosion becomes the dominant mechanism in erosion-corrosion. The mechanism of high temperature erosion is complicated by the simultaneous occur-

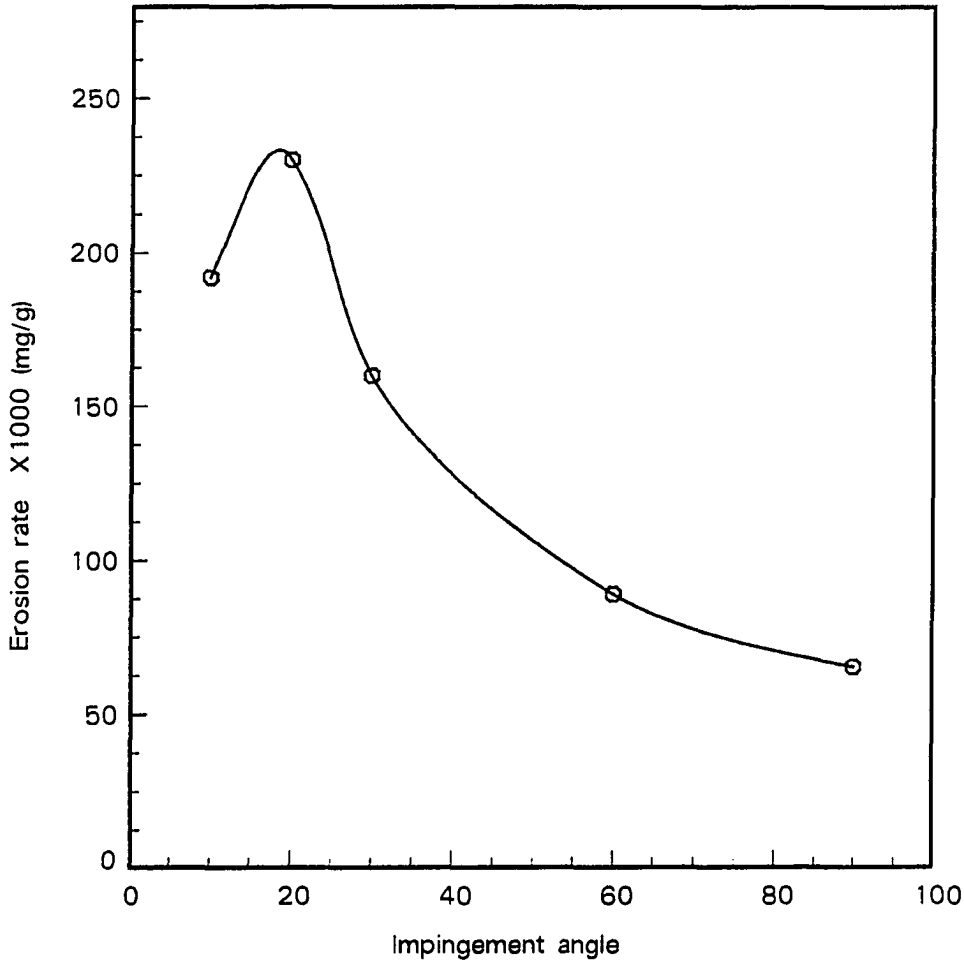

Figure 4: Impingement angle dependence of erosion rate at 500°C and an impingement velocity of 65 m/s

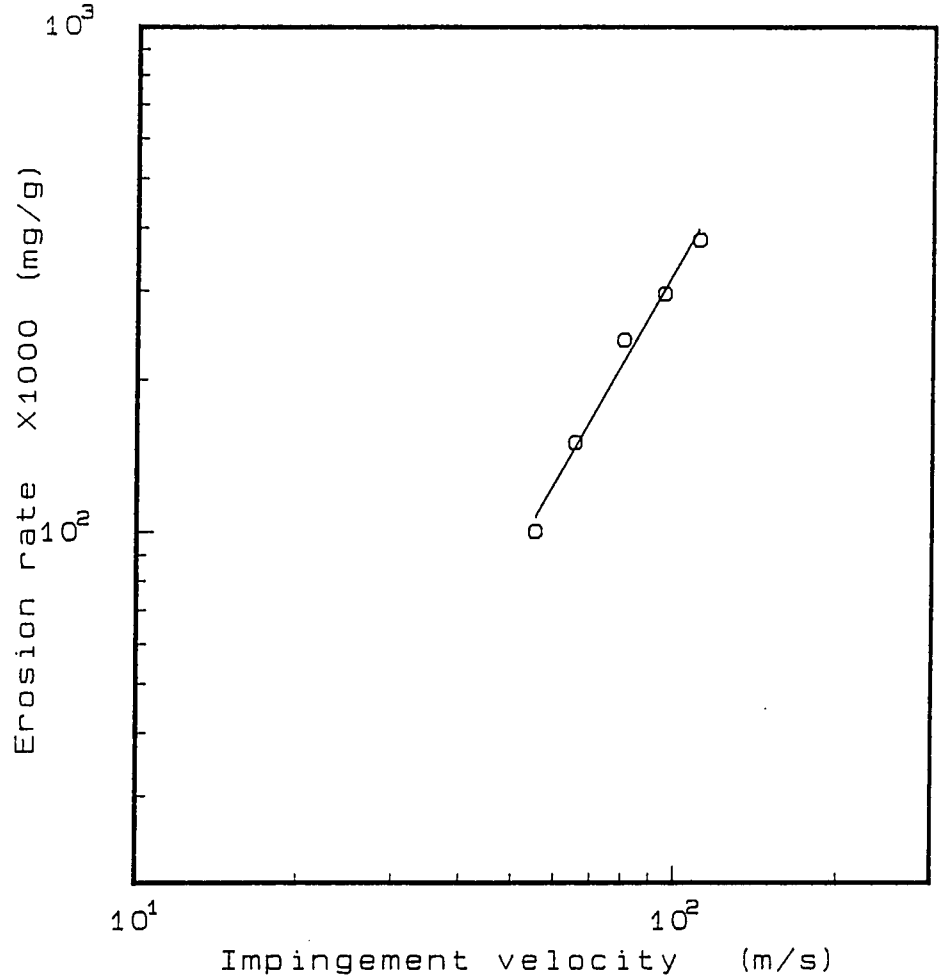

Figure 5: Impingement velocity dependence of erosion rate at 500°C and an impingement angle of 30°

rence of corrosion and erosion. This is all the more so because titanium is chemically reactive and the chemical activity of Ti-6Al-4V increases with increasing temperature. As can be seen, oxidation rate is a unique function of temperature and time. The thickness of oxide formed alloy layer on this alloy surface during exposure to air for different lengths of times and at different temperatures is given in Figure 6 [14].

The dependence of the oxidation of this alloy on temperature and time was studied by scanning electron microscopy. When exposed for 10 minutes at 650°C, the crystallites of oxide barely formed on the titanium specimen surface (Figure 7 (a)). The crystallite dimensions are fairly tiny indicating that the nucleation and growth rates were low at this temperature. With longer exposure over a period of 110 minutes, the surface was more densely covered by crystallites but the crystallite dimensions were still very small. There appears to be a transition from relatively low nucleation and growth rates to high ones above 650°C, because with 10 minutes exposure at 800°C the surface was completely covered by crystallites of approximately one-tenth micrometer dimension, as shown in Figure 7 (b). These oxide crystals appear to be cylindrical in shape. Figure 7 (c) shows the surface oxidation features for 110 minutes exposure at 800°C. The crystallites are stacked in multiple layers and have a large scatter in dimensions, varying from a tenth to above one micrometer. This indicates that the nucleation and growth of new crystallites and the agglomeration of pre-existing crystallites occurred simultaneously. Figure 7 (d) gives the cross-sectional view of oxide scale on the above specimen. It shows the multilayer development of oxide scale. The thickness of oxide layer, as estimated from this figure, is a little less than 1 μm.

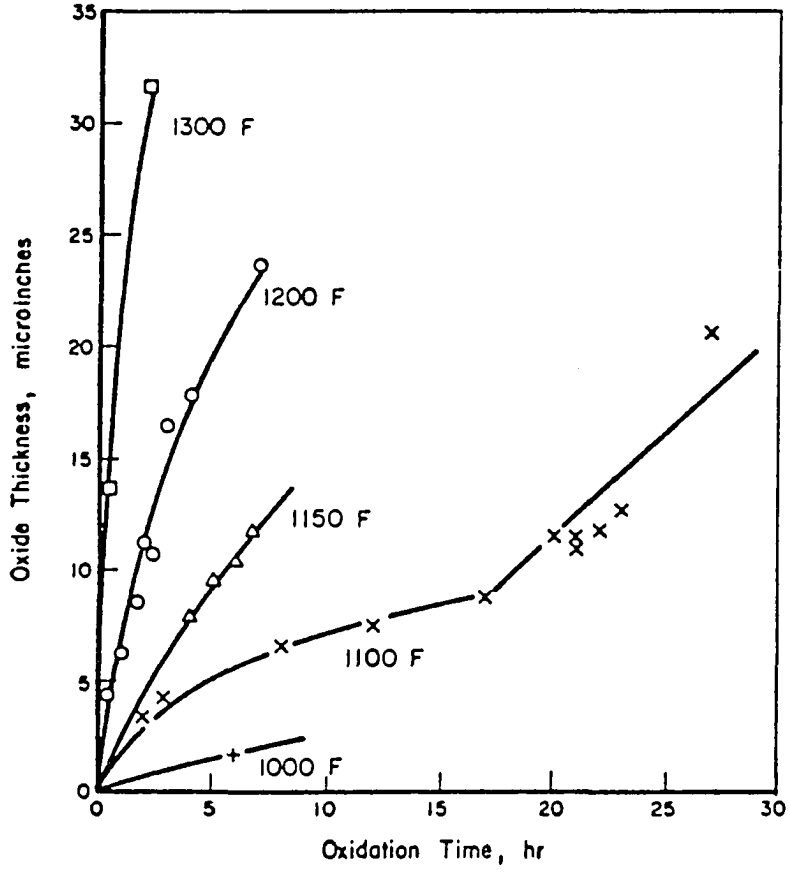

Figure 6: Oxide thickness formed on Ti-6Al-4V alloy after various air exposure times at several temperatures [14]

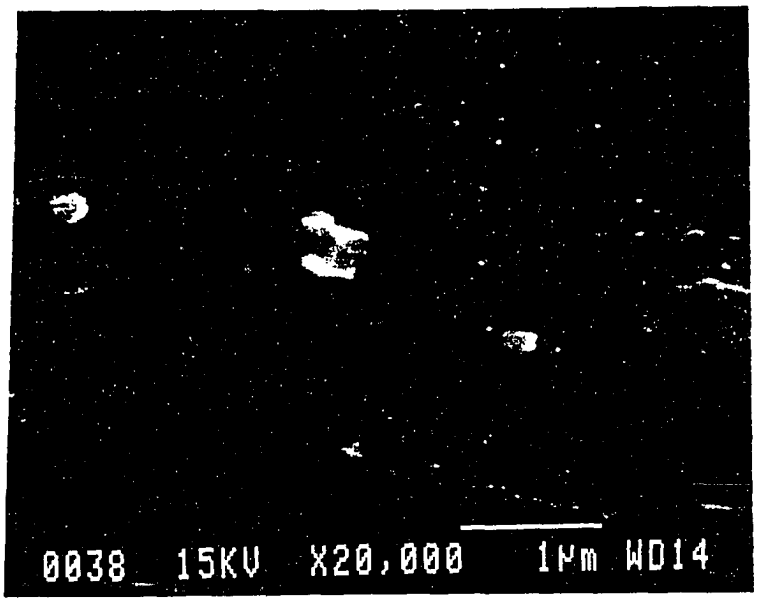

a

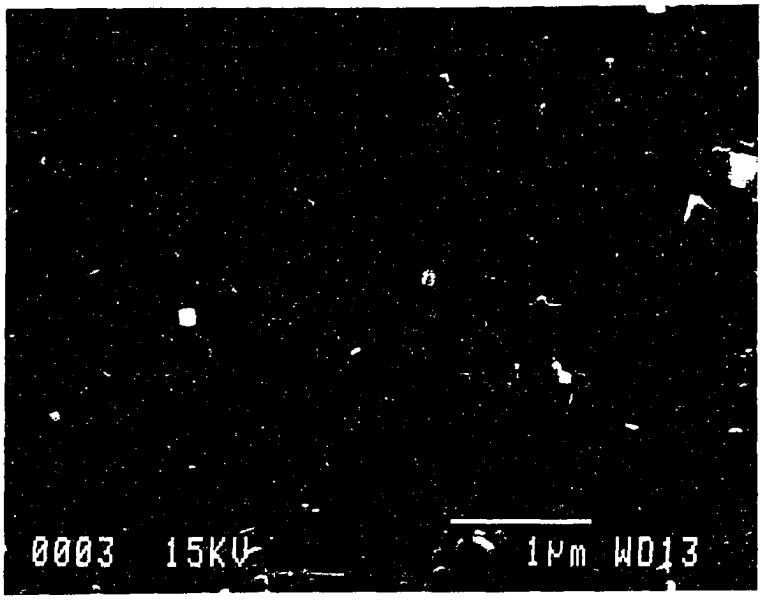

b

Figure 7: Oxidation features on Ti-6Al-4V surface after being exposed to air for (a) 10 minutes at 650°, (b) 10 minutes at 800°C, (c) 110 minutes at 800°, and (d) cross-sectional view of specimen oxidized for 110 minutes at 800°C

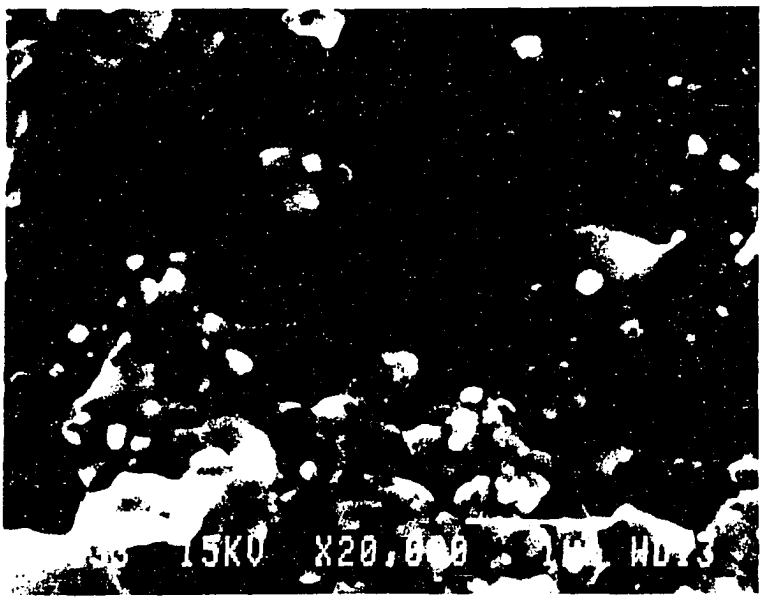

c

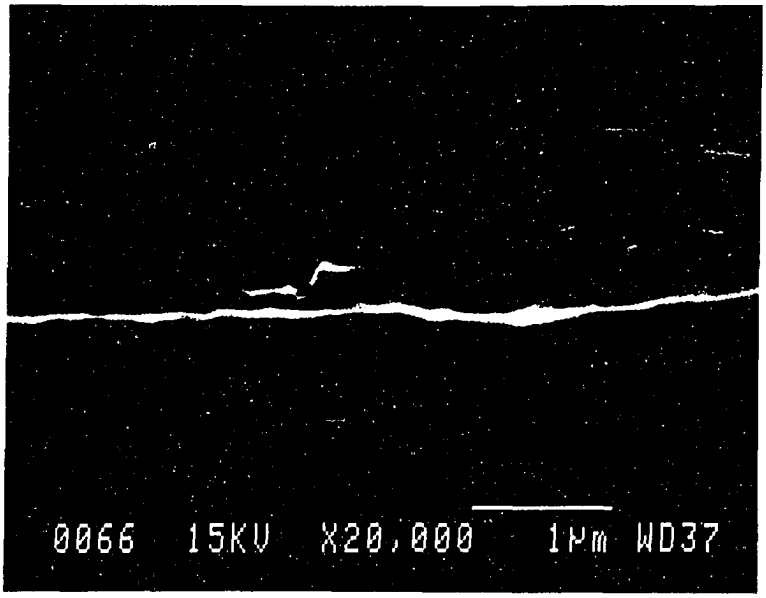

d

Figure 7 (Continued)

The gravimetric oxidation measurements were found to be consistent with the above observations. At 500°C the weight gain was less than $1.0 \times 10^{-4} mg/mm^2$ when the specimen was heated for as long as 110 minutes. The weight gains were $1.96 \times 10^{-4} mg/mm^2$ at 650°C and $1.96 \times 10^{-3} mg/mm^2$ at 800°C for 10 minutes exposure, and $8.48 \times 10^{-4} mg/mm^2$ and $9.79 \times 10^{-3} mg/mm^2$ for 70 minutes exposure at 650°C and 800°C respectively.

Though titanium can form TiO, Ti_2O_3, Ti_3O_5, and TiO_2 as the thermodynamically stable oxides, only TiO_2 was detected in the oxide scale by X-ray diffraction analysis at 800°C and below. This is supported by Figure 8 which shows the X-ray diffraction patterns where the upper line refers to the non-eroded area and the lower line to the eroded area.

Erosion Mechanisms

The eroded-corroded surfaces of the specimens were examined by scanning electron microscopy to develop an understanding of the mechanisms involved in both the room temperature and elevated temperature erosion. Figure 9 shows surface features at the centers of craters of the specimens tested at room temperature, 500°C and 800°C respectively. It should be noted that the crater surfaces for room temperature and, to some extent, for 500°C look more rugged overall whereas the surface for 800°C exhibits a lot of relatively large, flat and "smooth" band areas and thus indicates more ductile deformation. It seems that only the sharp corners of impacting particles could effectively penetrate into the substrate and remove material at low temperatures. At 800°C even the blunt features of the impacting particles were able to embed the surface, thereby establishing contact in large areas, removing consid-

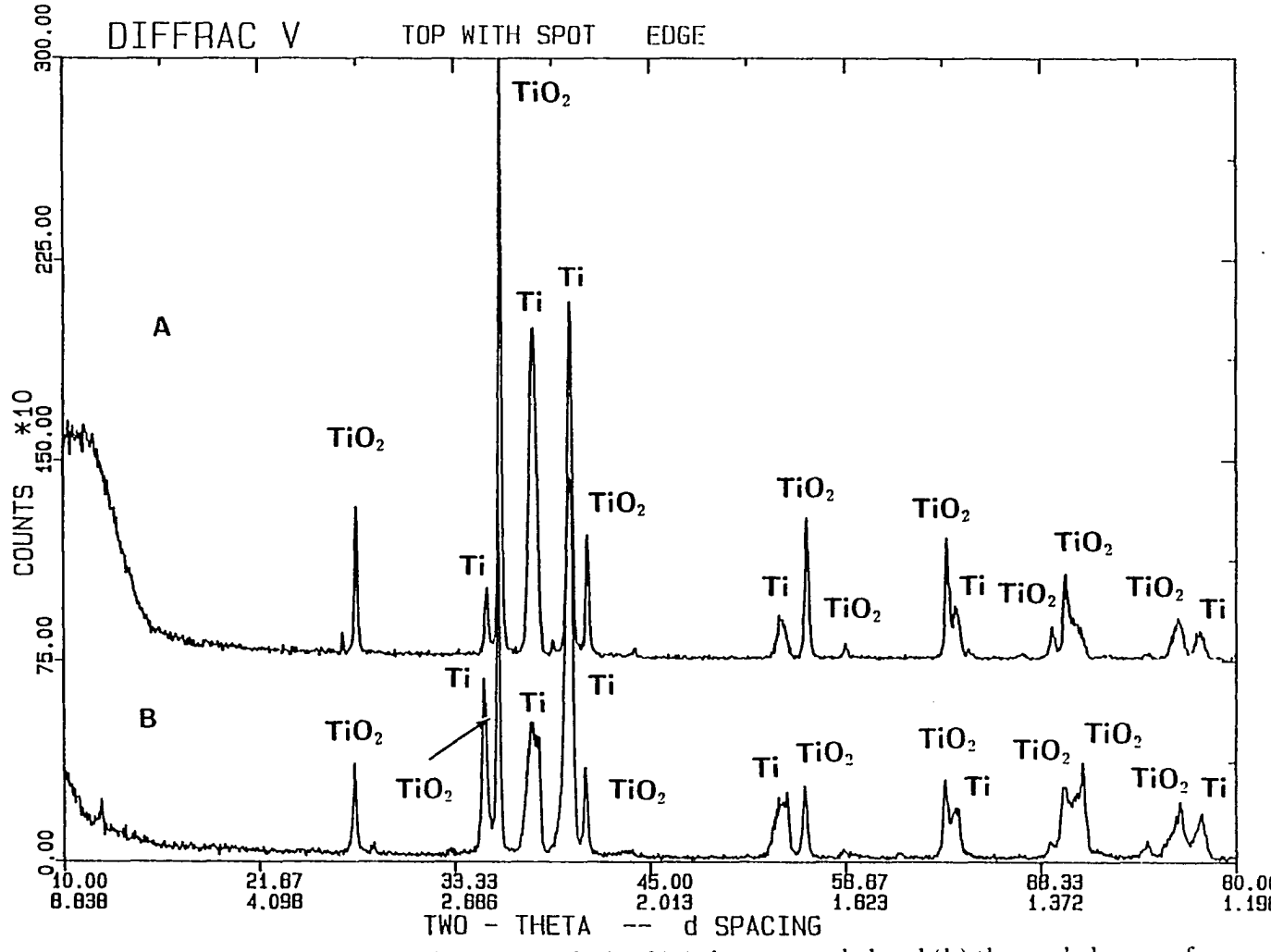

Figure 8: X-ray diffraction analysis of (a) the non-eroded and (b) the eroded areas of Ti-6Al-4V exposed to 800°C for 110 min. Impingement angle for erosion 30°, impact velocity 65 m/s.

erable material, and leaving large, deformed flat band features behind them.

The difference in surface morphology between the room temperature and high temperature erosion can also be observed from the cross-sectional views in Figure 10. At $800^{\circ}C$ the surface of the specimen underwent severe plastic deformation and deep pits were produced. Figure 10 (a) shows that an impacting particle cut deeply into the substrate at an angle of about 30° to the specimen surface and was stopped because of increasing resistance to deeper penetration. The right pit was the first to be produced by the impacting particle. It was after this that the pit on the left was created by the impact of another particle. As a result of this second impact, the material was piled up in front of the first pit and provided the surface contour as shown. The severely deformed ridge of the material between the two pits was probably removed during subsequent impacts. By comparison the depths of the pits produced in room temperature erosion were much shallower as shown in Figure 10 (b).

Figure 11 shows the damage features that resulted in the removal of material in erosion. Here Figure 11 (a) is the higher magnification photograph of the central part of Figure 9 (c). It shows that the impacting particle ploughed through the surface resulting in pile-up of material around the groove. This caused severe plastic deformation and generated microcracks on the contact surface. It is these microcracks that contributed to the separation of material from the substrate. Figure 11 (b) shows the details of the central part of Figure 9 (b) at higher magnification. Some chips produced by the cutting action of particles along with broken silicon carbide particles can be seen here. It seems that these chips could not detach from the

a

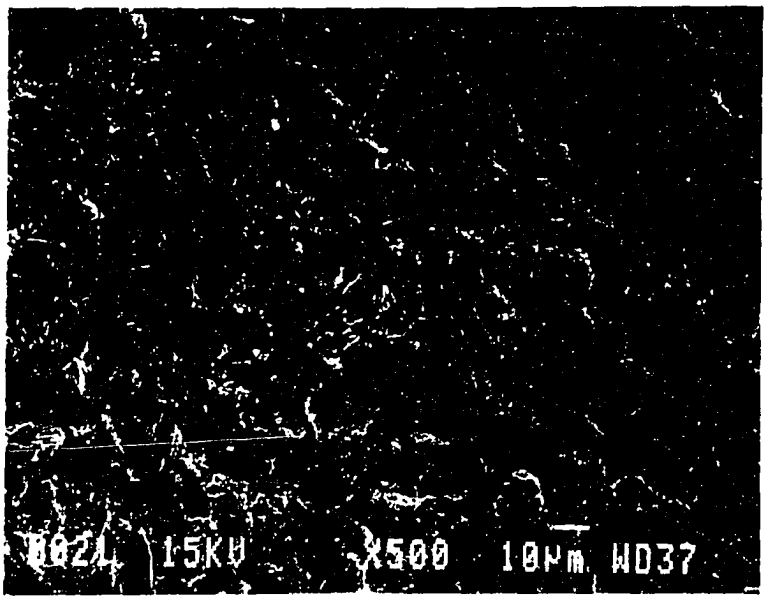

b

Figure 9: Surface morphology at the craters center of the specimen eroded at (a) 25°C, (b) 500°C, and (c) 800°C. Test conditions: 65 m/s velocity, 30° impingement angle.

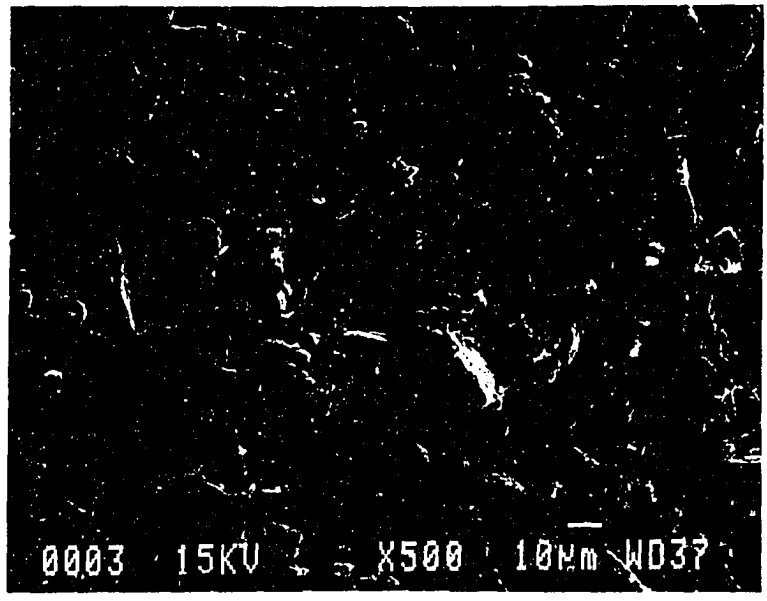

c

Figure 9 (Continued)

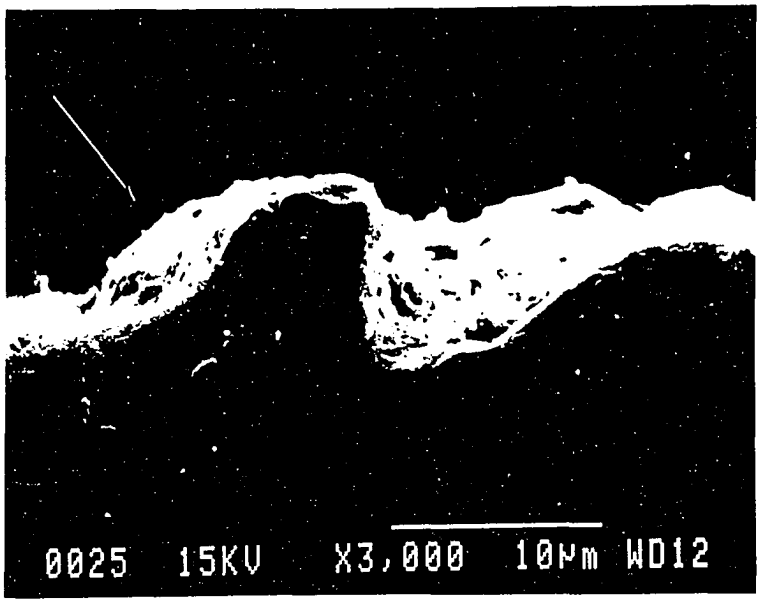

a

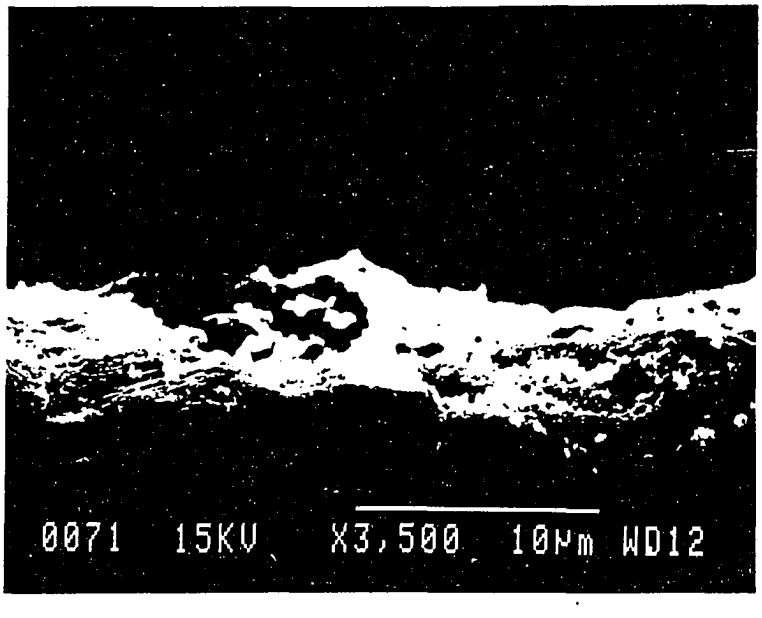

b

Figure 10: Cross-sectional view of the craters formed by erosion at the temperature of (a) 800°C; and (b) 25°C. Test conditons same as in Figure 9

substrate because of incomplete cutting or because of the blockage resulting from particle embedment.

Besides the cutting, ploughing and sliding actions discussed above, the material removal in erosion at high temperatures also occurred by blunt impacting. In this case, the impacting particles penetrated deeply into the target surface and material loss occurred from the debris generated by fracture under external impacts. The material exhibits here both the localized brittle features as indicated by the faceted debris and the ductile characteristics as indicated by severe plastic deformation. The features of erosion by blunt impacting are shown in Figure 12 where a "deep" pit was produced. The pit is surrounded by numerous debris. This kind of action is more prevalent in normal impingement, as seen in Figure 13. This process is helped also by decreased tensile strength.

The embedment of erodent particles is a common phenomenon which occurs both at room temperature and at elevated temperatures. Figure 14 (a) shows an erodent particle in a "large" erosion pit that was produced at room temperature. A large number of fragments separated from the target surface are also seen in this figure. Figure 14 (b) shows three SiC particles embedded into the surface during erosion at 500°C. The particle on the left embedded while impacting the surface from top at an acute angle, the one on the bottom embedded during normal impact, and that on the top-right side plowed a short distance while penetrating deeper into the substrate and stopped finally due to the exhaustion of kinetic energy.

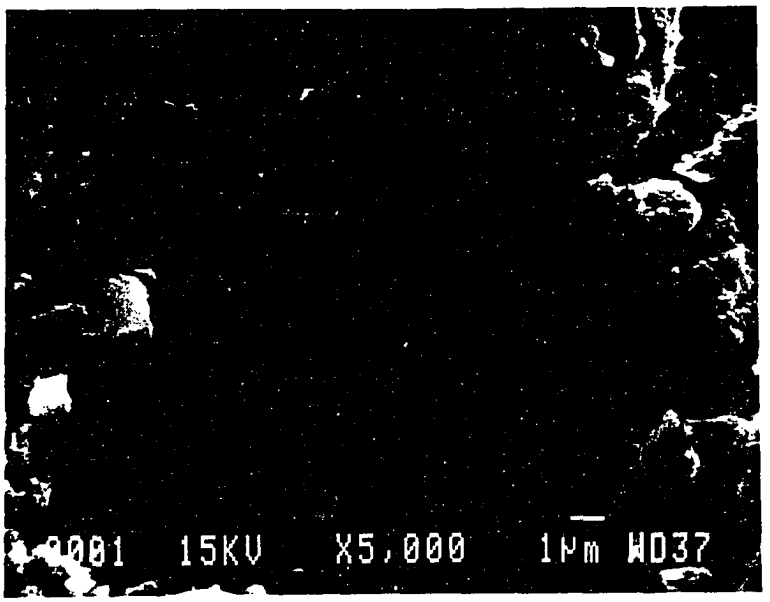

a

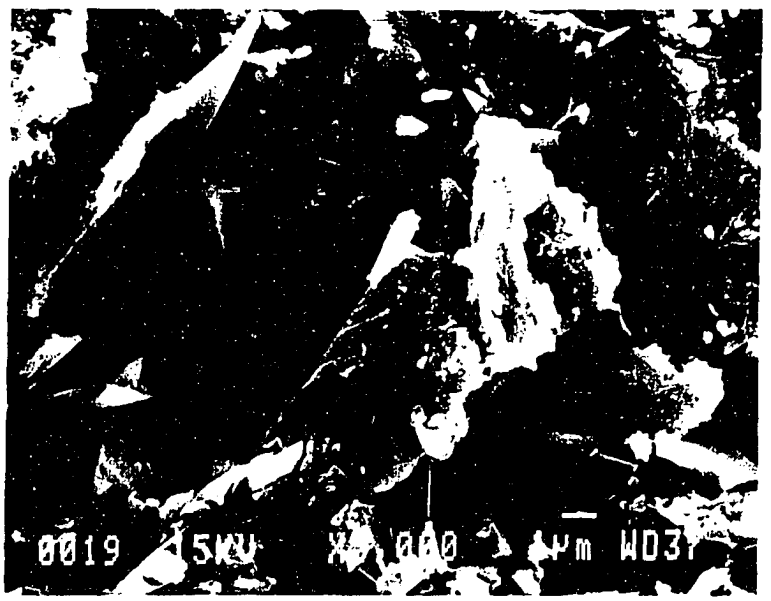

b

Figure 11: Plastic deformation features in erosion shown at higher magnification at the temperature given: (a) 800°C, and (b) 500°. Erosion conditions same as in Figure 9

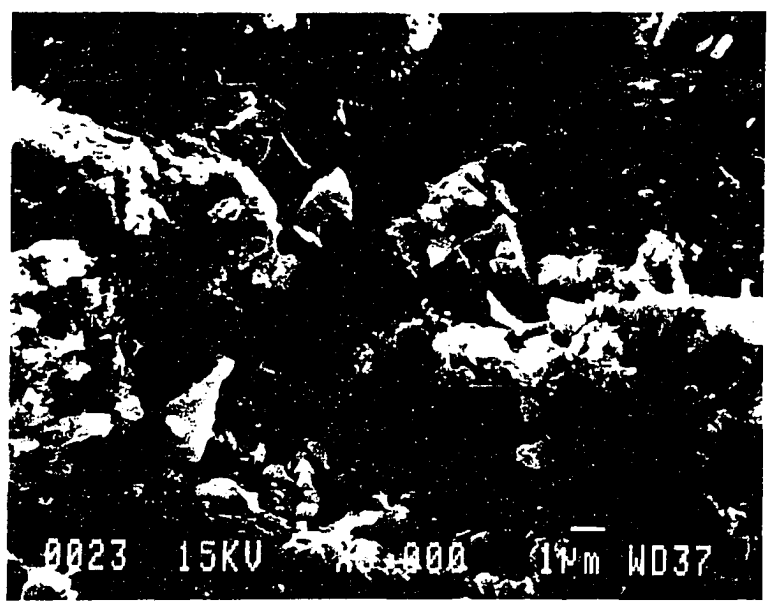

Figure 12: Features of blunt impacting in erosion. Erosion conditions: 500°C temperature, 65 m/s velocity and 30° impingement angle

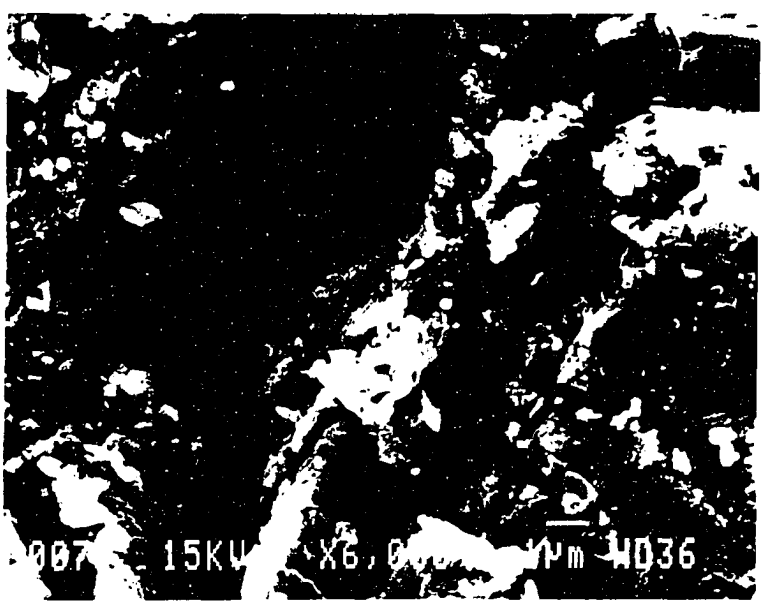

Figure 13: Erosion by blunt impacting angle in 90° impingement at 500°C

a

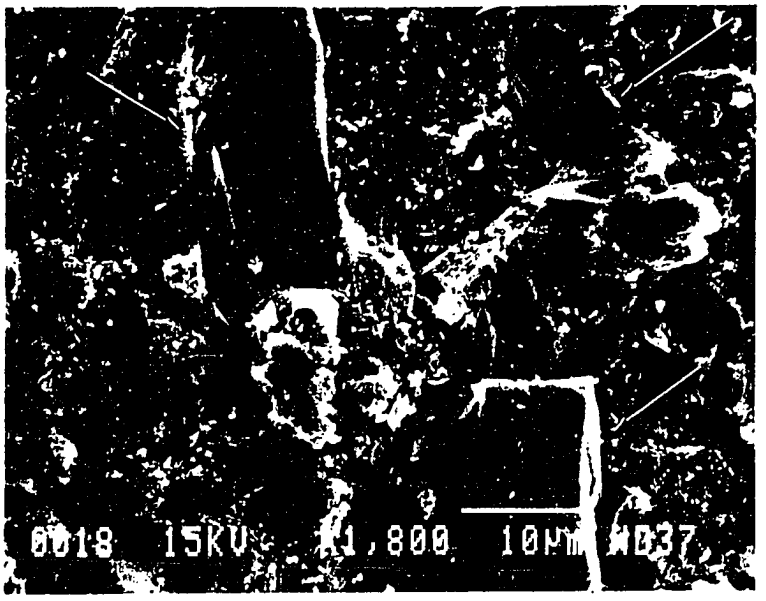

b

Figure 14: Embedment of erodent particles seen on the surface of Ti-6Al-4V eroded at (a) room temperature and (b) 500°C

Erosion-Corrosion Interaction

In order to provide protection to the surface from both the chemical and erosive damage, the oxide formed on the surface should have the following properties. It should adhere well to the substrate, have reasonable high-temperature elasticity and plasticity to resist fracture, be free of tensile stresses, and posses high melting point and low diffusion coefficients for metal ions and oxygen.

As described earlier, below 600°C the oxidation rate of Ti-6Al-4V was low and only a thin oxide layer was formed even after a prolonged exposure time (Figure 7). Such an oxide scale may provide some protection against further corrosion, but has negligible effect on erosion resistance because the scale is too thin and sparse. The oxidation resistance of titanium in air was very low above 650°C. The oxidation rate now followed a parabolic or linear relationship and a thick oxide scale which was prone to cracking and rupture due to the undesirable build up of stresses was formed. The oxide was formed here accompanied by an increase in volume at the metal-scale interface so that severe tensile stresses were induced. This made the oxide scale porous and susceptible to cracking.

The resistance of oxide film to the loading by erodent particles was studied by indentation tests. Figure 15 shows an indentation made by a square-base pyramid diamond indentor with 50 g load at the surface of a specimen oxidized for 110 minutes at 650 °C. Under external compressive deformation, the crystallites of oxide plastically deformed to provide a smooth contact surface, but the oxide scale cracked along the indentation boundaries. This indicates poor adherence between the oxide and its substrate even during static loading so that oxide scale would be easily separated during particle impacts. Similar observations were made from indentation

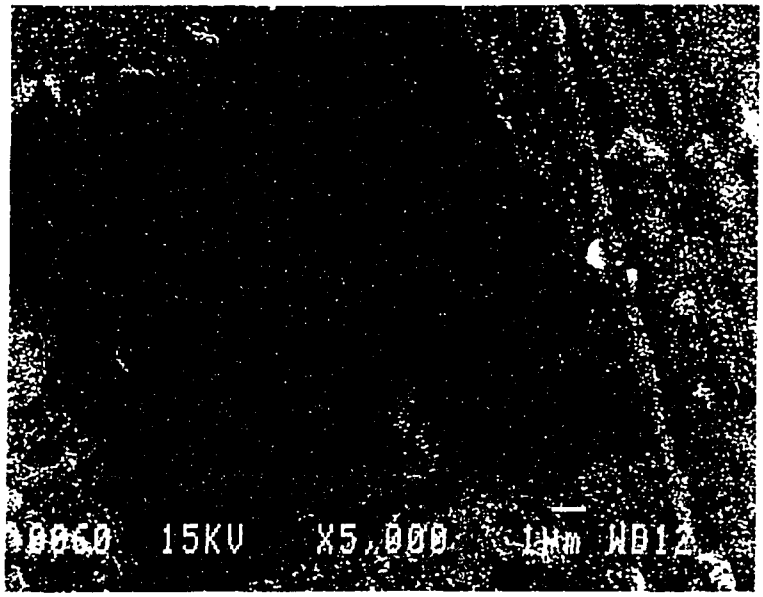

Figure 15: Plastic deformation and cracking of oxide scale in indentation test. Surface oxidized at 650°C for 110 min prior to indentation with a pyramid indentor under 60 g load

studies on the specimens exposed to 800°C as well. Severe spalling of oxide scale from the specimen surface exposed to 800°C was also noticed during cooling to room temperature. Based on these observations, it was concluded that the oxide formed at a temperature above 650 °C neither provided protection against corrosion nor erosion. Instead, it accelerated the removal of material during erosion because the porous oxide due to its poor adhesion to the substrate was easily removed by particle impacts. This exposed the fresh material to air which was rapidly oxidized because of its high oxidation rate. Therefore, corrosion accelerated erosion and erosion accelerated corrosion, because corrosion always occurred at the high initial rate. This process went round and round so that more and more material was wasted by the combined erosion-corrosion action. This is why erosion rate dramatically increased between 650-800°C when oxidation occurred at a rapid rate. This is what was basically responsible for the third range in Figures 1 and 2. The increase in erosion rate in the third range was higher in normal impacts than in 30° impacts because the oxide scale was more efficiently removed by spalling under normal impacts than by cutting under oblique impacts.

Figure 16 (a) shows how the oxide scale was displaced by an erodent particle which impacted in the direction of the arrow. It produced a pile up of the oxide scale as confirmed by the elemental mapping in Figure 16 (b). The undisturbed oxygen film can also be seen in this figure.

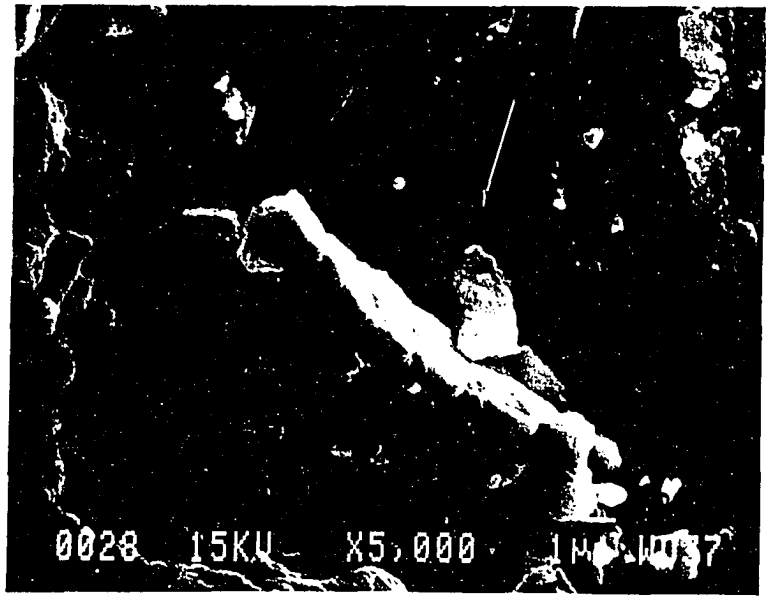

a

b

Figure 16: (a) Oxide scale displacement and pile-up, and (b) elemental mapping of the area in (a). Arrow shows the direction of particle impact (Temperature: 800°C)

CONCLUSIONS

From the erosion-corrosion studies on Ti-6Al-4V in high temperature air environment up to 800°C, the following conclusions were drawn:

1. There was no change in erosion rate with temperature up to 200°C. Erosion rate increased moderately with temperature up to 650°C and significantly from 650 to 800°C.

2. Erosion rates were the same for both of the heat treatment, conditions which were namely, annealing, and solution treating and aging.

3. The variation of erosion rate with temperature for normal impingement was similar to that for 30° impingement, but the increase in erosion rate between 650 and 800°C occurred more rapidly under normal impact condition. The latter was due to the spalling character of oxide scales.

4. It was possible to relate the changes in erosion rate with temperature with the changes in mechanical properties, oxidation rate, and oxide scale deformation behavior.

5. Erosion rate ($\dot{\epsilon}$) varied with impingement velocity (V) according to the relationship $\dot{\epsilon} \propto V^n$ where the exponent n was equal to 1.89 for 500°C as compared to 2.35 for room temperature.

6. The mechanisms of elevated temperature erosion were cutting, ploughing, the fragmentation of material by blunt impacting, and the spalling of oxide layers.

7. The oxidation of the alloy occurred at a high rate was rapid above 650°C. The oxide scale formed was poor in adherence and prone to fracture upon impact. The rapid increase in erosion rate between 650 to 800°C was partly because of these oxide scale characteristics.

REFERENCES

[1] Yerramareddy, S. and S. Bahadur. "Effect of Operational Variables, Microstructure and Mechanical Properties on the Erosion of Ti-6Al-4V." Wear 142 (1991): 253-263.

[2] Massoud, J. P., G. Coquerelle, and M. Collin. "Particle Erosion Behaviour of Laser Surface Treated Ti-6Al-4V." In Erosion by Liquid and Solid Impact, The Seventh International Conference Held in England 1-10 September 1987, edited by J. E. Field and J. P. dear, 53-1-53-7. England: Cavendish Laboratory, University of Cambridge, 1987.

[3] Emiliani, M. and R. Brown. " Erosion of Ti-6Al-4V by Spherical Silica Particles at 90° Impact Angle." In Erosion by Liquid and Solid Impact, The Sixth International Conference Held in England 5-8 September 1983, edited by J. E. Field and N. S. Corney, 40-1-40-5. England: Cavendish Laboratory, University of Cambridge, 1983.

[4] Smeltzer, C. E., M. E. Gulden, and W. A. Compton. "Mechanisms of Metal Removal by Impacting Dust Particles." Journal of Basic Engineering (September 1970): 639-654.

[5] Gat, N. and W. Tabakoff. "Some Effects of Temperature on the Erosion of Metals." Wear 50 (1978): 85-94.

[6] Tabakoff, W. "Erosion Study of High Temperature Metals Used in Turbomachinery." In High Temperature Corrosion in Energy Systems, ed. M. F. Rothman, 809-23. Indiana: The Metallurgical Society of AIME, 1985.

[7] Zhou, J. and S. Bahadur. "High-Temperature Erosion-Corrosion Behavior of Stainless Steels." In Corrosion & Particle Erosion at High Temperatures, ed. V. Srivivasan and K. Vedula, 315-33. Warrenda: TMS, 1989.

[8] Tilly, G. P. "Erosion Caused by Impact of Solid Particles." In Treatise on Materials Science and Technology 13, ed. D. Scott, 287-319. New York: Academic Press, 1979.

[9] Doyle, P. A. and A. V. Levy. "The Elevated Temperature Erosion of 1100 Aluminum by a Gas-Particle Steam." In Corrosion- Erosion Behavior of Material, ed. K. Natesan, 162-76. Warrendale: The Metallurgical Society of AIME, 1980.

[10] Zhou, J. and S. Bahadur. "Further Investigations on the Elevated Temperature Erosion-Corrosion of Stainless Steels," In Corrosion-Erosion-Wear of Materials at Elevated Temperatures, The Fourth Berkeley Conference Held in California 1990. California: 1990.

[11] Morrison, C. T., R. O. Scattergood, and J. L. Routbort. "Erosion of 304 Stainless Steel." Wear 111 (1986): 1-13.

[12] Levy, A. V., J. Yan, and J. Patterson. "Elevated Temperature Erosion of Steels." Wear 108 (1986): 43-60.

[13] Levy, A. V., E. Slamovich, and N. Jee. "Elevated Temperature Combined Erosion-Corrosion of Steels." Wear 110 (1986): 117-49.

[14] Wood, R. A. and R. J. Favor ed. Titanium Alloys Handbook. Ohio: Air Force Materials Laboratory and Wright-Patterson Air Force Base, 1972.

[15] Benjamin, D., ed. Metals Handbook Ninth Edition. Vol. 3, 351-418, Titanium and Titanium Alloys, by the ASM Committee on Titanium and Titanium Alloys and L. C. Covington. Ohio: American Society for Metals, 1980.

[16] Kofstad, P. High Temperature Corrosion. New York: Elsevier Applied Science, 1988.

GENERAL SUMMARY

The phenomenon of erosion gets fairly complicated at high temperatures because of the changes in target material properties, and microstructure, and the interaction between erosion and corrosion. These studies revealed that the material loss rate due to solid particle impacts increased with the increase in temperature for all materials but the increase was negligibly small in the initial stages of temperature rise. Beyond a certain temperature, which depended upon the material, the increase in erosion was more significant and became even greater with further increase in temperature. This behavior could be explained in terms of the changes in mechanical properties, mainly the strength and ductility of the materials, as well as the changes in microstructure. In the case of Ti-6Al-4V, the additional factor responsible for increased erosion was rapid corrosion at elevated temperatures. The strength of all materials decrease with the increase in temperature. This was partly responsible for increasing erosion at high temperatures. Microstructural changes also occurred and these changes were accelerated in the presence of stress. For instance, in stainless steels These changes induced the precipitation and formation of a brittle "network" along the grain boundaries which degraded the erosion resistance of the materials.

In this work, both ductile and brittle materials were studied. The stainless steels and Ti-6Al-4V were ductile materials while alumina ceramics a into the category of

brittle materials. The fracture processes in high temperature erosion did not follow this ideal classification. The typical ductile materials such as stainless steels showed localized brittleness because of the formation of a brittle network due to precipitation which occurred along the grain boundaries. Similarly, the typical brittle alumina ceramics exhibited plastic deformation in solid particle impacts which was increased in the presence of secondary phases. The mechanism of erosion also changed with the change in impingement angle.

The maximum in material loss rate occurred in the impingement angle range of $20^\circ \sim 30^\circ$ for 304 stainless steel and Ti-6Al-4V irrespective of the temperature. A slight shift in the peak from 30° at room temperature to 20° at elevated temperature was observed. For alumina ceramics impacted at 650°C, the peak in erosion rate occurred at 90° which is typical for brittle materials under room temperature erosion condition. This indicated that the brittle mechanism was still in effect at 650°C.

Erosion rate $\dot{\epsilon}$ was found to be less sensitive to impingement velocity V at high temperatures. The value of the exponent n at high temperatures in the relationship $\dot{\epsilon} \propto V^n$ was found to be lower than at room temperature for all the materials studied in this work. The increased ductility and decreased strength at high temperature could basically account for this change.

Erodent concentration was found to be a more important factor in affecting erosion at high temperature than at room temperature. This has been explained in terms of several phenomena such as the interaction between impingement particles and target material, lower critical erosivity at high temperatures, the time available for oxidation, the mechanisms responsible for material removal, and the intercollision between particles. Another parameter that affected erosion was the particle size. It

was observed that fine particles were less erosive than coarse particles under the same impingement conditions.

Because of the excellent heat resistance of the materials studied, oxidation did not become fairly profound up to 800°C except in the case of Ti-6Al-4V. It was only at 800°C that some significant interactions between erosion and corrosion could be observed in stainless steels. The observations from the dynamic impact and the scratch tests revealed that the oxide scale formed on surfaces of these alloys was strong and pliable and had excellent adherence to the substrate. While such oxide scales prevented the surface from further corrosion, they also provided protection to the substrate from erosion attack. On the other hand, oxidation was enhanced by erosion damage. In the case of Ti-6Al-4V, which had limited oxidation resistance above 650°C, the oxide scale formed did not adhere well to the substrate and was therefore, prone to fracture upon impact, This partially accounted for the rapid increase in erosion rate in the temperature range 600 to 800°C.

The eroded surface morphology also changed with test temperature. The morphological features showed that at high temperatures the surface material underwent severe plastic deformation. Upon solid particle impact, the grain boundaries in the substrate were severely deformed and slip bands could be seen. The surface morphology depended strongly upon the impingement angle in the case of alumina ceramics: it provided typical brittle fracture characteristics under normal impingement and showed plenty of plastic deformation features under oblique impingement.

The failure mechanisms in alumina ceramics were greatly affected by their composition and microstructure. The intergranular failure was dominant in single phase alumina, and fully developed cracks which led to the complete removal of fragments

were observed. In the case of alumina containing 4% silicate glassy phase, transgranular cracking was the main failure mechanism. The crack density in this case was and plenty of fragments loosely attached to the substrate could be seen. The multi-phase aluminas, containing either glassy phase, or zirconia or both, were more resistant to erosion than single phase alumina at all temperatures. But the presence of substantial amounts of glassy phase degraded mechanical properties and accelerated the erosion rate. Under the conditions used in the present work, the particles on impact did not create classical lateral cracks which are the basis for brittle indentation fracture model. Since at elevated temperatures the ductile mechanisms of erosion were involved, the erosion behavior of aluminas was not uniquely governed by the indentation fracture model as is generally thought to be the case in room temperature erosion. Thus the indentation fracture model needs to be modified for high temperature erosion situations.

ACKNOWLEDGMENTS

I am greatly indebted to Professor Shyam Bahadur for his continual guidance and encouragement throughout the course of this study. I would like to acknowledge the understanding and support he showed in my work. Without these, this work would not be what it is today.

In addition, I would like to express my appreciation to Dr. William Larsen and Dr. John Verhoeven for their helpful suggestions and discussions in the area of materials science and engineering. I am also grateful to Dr. Palaniappa Molian, Dr. Yu-Min Tsai, and Dr. William Spitzig for their valuable time and help in materials and mechanics. I thank all my friends for their encouragement and expectations.

I would like to dedicate this work to my parents for their dreams, their sacrifice, and their encouragement. I am greatly thankful to my wife Qin Wang for her constant encouragement, support, and patience.